

Dissertation for the degree of Doctor of Philosophy

Study of the Multi-strange Resonance  
 $\Xi(1530)^0$  Production with ALICE  
at the LHC Energies

The background of the page features a large, light blue watermark of the Pusan National University logo. The logo is circular, with the university's name in English, "PUSAN NATIONAL UNIVERSITY", around the perimeter. In the center is a stylized emblem consisting of a blue crown-like shape above a green square containing the Korean characters "부산" (Busan) and the year "1946" below it.

Jihye Song

Department of Physics  
The Graduate School  
Pusan National University

February 2018

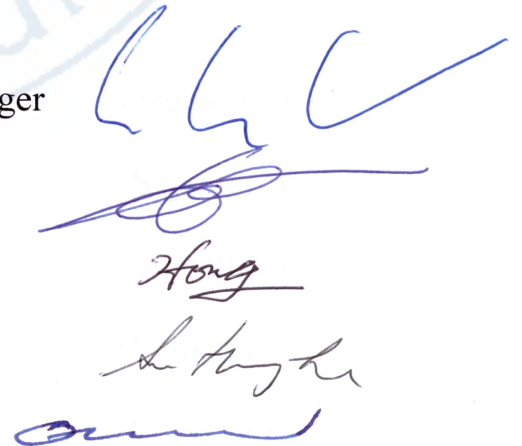
# Study of the Multi-strange Resonance $\Xi(1530)^0$ Production with ALICE at the LHC Energies by Jihye Song

A Dissertation submitted to the graduate school of  
Pusan National University in partial fulfillment of  
the requirements for the degree of Doctor of  
Philosophy in Physics  
under the direction of Prof. Dr. In-Kwon Yoo

The dissertation for the degree of Doctor of Philosophy  
by Jihye Song  
has been approved by the committee members.

December 15, 2017

Chair	Peter Braun-Muzinger
Member	Boris Hippolyte
Member	Byungsik Hong
Member	Su Houngh Lee
Member	In-Kwon Yoo



Handwritten signatures of the committee members in blue ink, corresponding to the names listed in the table.



# Table of Contents

<b>List of Tables</b> . . . . .	<b>v</b>
<b>List of Figures</b> . . . . .	<b>vi</b>
<b>Chapter 1 Introduction</b> . . . . .	<b>1</b>
1.1 Matter under extreme conditions . . . . .	1
1.2 Collision systems and physical observables in experiment . . . . .	4
1.3 Resonance and hyperon production . . . . .	6
1.3.1 Study of hadronic phase . . . . .	6
1.3.2 Hyperon production . . . . .	10
1.3.3 Mean transverse momentum . . . . .	12
<b>Chapter 2 A Large Ion Collider Experiment at the LHC</b> . . . . .	<b>14</b>
2.1 The ALICE detector . . . . .	15
2.1.1 Particle identification in the TPC . . . . .	19
2.1.2 Particle identification using weak decay topology . . . . .	22
2.1.3 Definition of ALICE coordinate system . . . . .	23
2.2 Determination of centrality definition . . . . .	24
<b>Chapter 3 Measurements of <math>\Xi(1530)^0</math> in p–Pb and Pb–Pb collisions</b> <b>27</b>	
3.1 $\Xi(1530)^0$ -reconstruction . . . . .	27
3.1.1 Data sample and event selection . . . . .	28
3.1.2 Track and topological selection criteria . . . . .	33
3.1.3 Particle identification . . . . .	35
3.1.4 Signal extraction . . . . .	40
3.2 Efficiency correction . . . . .	63
3.3 Corrected $p_T$ -spectra . . . . .	67
3.4 Systematic uncertainties . . . . .	69
<b>Chapter 4 Results and discussion</b> . . . . .	<b>74</b>
4.1 $\Xi(1530)^0$ transverse momentum spectra . . . . .	74
4.2 Particle yield ratios . . . . .	77
4.2.1 Integrated particle ratio to ground state particle . . . . .	77
4.2.2 Integrated particle ratio to $\pi$ . . . . .	83
4.3 Multiplicity and mass dependence of $\langle p_T \rangle$ . . . . .	86
4.4 Conclusions and outlook . . . . .	88

References . . . . .	94
----------------------	----



# List of Tables

1.1	Lifetime of the measured resonances with their quark content, decay modes exploited for the measurements presented here and branching ratios [16]. . . . .	10
2.1	Mean charged-particle multiplicity densities ( $\langle dN_{\text{ch}}/d\eta_{\text{lab}} \rangle$ ) measured at mid-rapidity ( $ \eta_{\text{lab}}  < 0.5$ ) [35], corresponding to the centrality classes defined using the V0A (V0M) detector [33, 34] in p–Pb (Pb–Pb) collisions at $\sqrt{s_{\text{NN}}} = 5.02$ (2.76) TeV. . . . .	25
3.1	Number of analyzed events per multiplicity/centrality interval . . .	32
3.2	Track selections common to all decay daughters and primary track selections applied to the charged pions from decays of $\Xi^{*0}$ . . . . .	34
3.3	Topological and track selection criteria. . . . .	35
3.4	Summary of the systematic uncertainties in minimum-bias events. Minimum and maximum values from all $p_{\text{T}}$ intervals and multiplicity classes in p–Pb, centrality classes in Pb–Pb are shown for each source. . . . .	73
4.1	Integrated yield, $dN/dy$ , and $\langle p_{\text{T}} \rangle$ in each multiplicity/centrality interval. Statistical (first one), systematic uncertainties due to selection criteria (second one) and uncertainties due to extrapolation (third one) from the various fit functions are quoted. . . . .	77

# List of Figures

1.1	QCD phase diagram of nuclear matter as functions of temperature and baryon density [4]. . . . .	2
1.2	A schematic view of the evolution of an ultra-relativistic heavy-ion collision. . . . .	3
1.3	Values of $\langle dN_{ch}/d\eta \rangle$ as a function of $\sqrt{s_{NN}}$ . Measurements for inelastic $pp(p\bar{p})$ collisions as a function of $\sqrt{s}$ are also shown along with those from Non-Single Diffractive (NSD) p-A and d-A collisions. The energy dependencies of the AA and $pp(p\bar{p})$ collision data are well described by the functions $s_{NN}^{0.155}$ (solid line) and $s_{NN}^{0.103}$ (dashed line), respectively. The shaded bands show the uncertainties on the extracted power-law dependencies. The central Pb-Pb measurements from CMS and ATLAS at 2.76 TeV have been shifted horizontally for clarity [12]. Note that, the color of point for NSD in p-A collision is changed to blue to emphasize. . . . .	5
1.4	Possible interactions of resonances during the hadronic phase. . . .	7
1.5	Ratios of $K^{*0}/K^-$ and $\phi/K^-$ with system size measured at mid-rapidity in pp and Pb-Pb collisions. Statistical uncertainties (bars) are shown as well as total systematic uncertainties (hollow boxes) and systematic uncertainties uncorrelated across multiplicity (shaded boxes). A few model predictions are also shown as lines at their appropriate abscissa [15]. . . . .	9

1.6	$\Xi/\pi$ (left) and $\Omega/\pi$ (right) ratios as a function of charged particle multiplicity densities in pp at 7 TeV, p-Pb at 5.02 TeV and Pb-Pb collisions with 2.76 TeV [19]. . . . .	11
1.7	Particle yield ratios to pion of strange and multi-strange baryons and protons normalized to the values measured in the inclusive pp sample in both pp and in p-Pb collisions [22]. . . . .	12
1.8	Mean transverse momentum of identified particles measured by ALICE in p-Pb collisions (left) and, in pp and Pb-Pb collisions (right) as a function of the charged particle density measured in the pseudorapidity range $ \eta  < 0.5$ . Statistical uncertainties are represented as bars, whereas boxes indicate systematic uncertainties [23, 24]. . . .	13
2.1	The CERN accelerator complex . . . . .	14
2.2	The ALICE experimental setup and detectors [28]. . . . .	16
2.3	Schematic view of the TPC . . . . .	18
2.4	The $p_T$ resolution for standalone TPC and ITS-TPC matched tracks with and without constraint to the vertex. [26]. . . . .	19
2.5	Transverse momentum resolution in the central rapidity region ( $ \eta  < 0.8$ ) for TPC tracks combined with hits in the ITS [29]. . . .	20
2.6	Specific energy loss ( $dE/dx$ ) in the TPC as a function of momentum in p-Pb collisions at $\sqrt{s_{NN}} = 5.02$ TeV (top) and Pb-Pb collisions at $\sqrt{s_{NN}} = 2.76$ TeV (bottom). The lines show the parameterizations of the expected mean energy loss. . . . .	21
2.7	Invariant mass distribution of $\pi^+\pi^-$ (left panel), $p\pi^-$ (middle) and $\Lambda\pi$ pairs (right panel) in Pb-Pb collisions at $\sqrt{s_{NN}} = 2.76$ TeV [30, 18].	23
2.8	Definition of the ALICE coordinate system axis, angles and detector sides . . . . .	23



2.9	Two heavy-ions before collision with impact parameter $b$ and then, the spectator nucleons continue unscattered, while in the participant zone particle production takes place [32]. . . . .	24
2.10	Distribution of the sum of amplitudes in the V0A (top) (Pb-going) for p-Pb collisions and V0M (bottom) for Pb-Pb collisions. Centrality classes are indicated by vertical lines. The insets show zoom-in distributions on the most peripheral events. [33, 34] . . . . .	26
3.1	Distribution of vertex- $z$ position from the accepted events in p-Pb collision (top) and in Pb-Pb collisions (bottom). The red dashed line indicates vertex cut on $ V_z  < 10$ cm . . . . .	30
3.2	Multiplicity distribution of accepted events in p-Pb collision in percentile. The each color presents the four intervals for the analysis. . . . .	31
3.3	Centrality distribution for the three different trigger bins. . . . .	32
3.4	Sketch of the decay modes for $\Xi^{*0}$ and depiction of the track and topological selection criteria. . . . .	35
3.5	TPC $dE/dx$ as function of momentum in p-Pb collisions for total (Left) and selected first emitted $\pi$ in $3\sigma$ (Right) . . . . .	36
3.6	TPC $dE/dx$ as function of momentum in p-Pb collisions for total (Left) and selected second emitted $\pi$ in $3\sigma$ (Right) . . . . .	36
3.7	TPC $dE/dx$ as function of momentum in p-Pb collisions for total (Left) and selected last emitted $\pi$ in $3\sigma$ (Right) . . . . .	37
3.8	TPC $dE/dx$ as function of momentum in p-Pb collisions for total (Left) and selected proton in $3\sigma$ (Right) . . . . .	37
3.9	TPC $dE/dx$ as function of momentum in Pb-Pb collisions for total (Left) and selected first emitted $\pi$ in $3\sigma$ (Right) . . . . .	38
3.10	TPC $dE/dx$ as function of momentum in Pb-Pb collisions for total (Left) and selected second emitted $\pi$ in $3\sigma$ (Right) . . . . .	38



3.11	TPC $dE/dx$ as function of momentum in Pb–Pb collisions for total (Left) and selected last emitted $\pi$ in $3\sigma$ (Right) . . . . .	39
3.12	TPC $dE/dx$ as function of momentum in Pb–Pb collisions for total (Left) and selected proton in $3\sigma$ (Right) . . . . .	39
3.13	$\Xi^\mp\pi^\pm$ invariant mass distribution (Same-event pairs) in $1.8 < p_T$ $< 2.2$ GeV/ $c$ for the multiplicity class of 20-40% in p–Pb collisions (left) and in $3.0 < p_T < 3.5$ GeV/ $c$ for the centrality class of 0-10% in Pb–Pb collisions (right). The signals are presented as black dots and the mixed-event backgrounds are shown as red dots for p–Pb collisions and blue dots for Pb–Pb collisions. . . . .	40
3.14	$\Xi^\mp\pi^\pm$ invariant mass distributions (full circle) and the mixed-event background distributions (open circle) for 10 $p_T$ bins from minimum- bias events (0-100%) in p–Pb collisions. The values written above each figure indicate bin boundary of $p_T$ bin. . . . .	42
3.15	$\Xi^\mp\pi^\pm$ invariant mass distributions (full circle) and the mixed-event background distributions (open circle) for 10 $p_T$ bins from central events (0-20%) in p–Pb collisions. The values written above each figure indicate bin boundary of $p_T$ bin. . . . .	43
3.16	$\Xi^\mp\pi^\pm$ invariant mass distributions (full circle) and the mixed-event background distributions (open circle) for 10 $p_T$ bins from 20-40% centrality interval in p–Pb collisions. The values written above each figure indicate bin boundary of $p_T$ bin. . . . .	44
3.17	$\Xi^\mp\pi^\pm$ invariant mass distributions (full circle) and the mixed-event background distributions (open circle) for 10 $p_T$ bins from 40-60% centrality interval in p–Pb collisions. The values written above each figure indicate bin boundary of $p_T$ bin. . . . .	45

3.18	$\Xi^\mp\pi^\pm$ invariant mass distributions (full circle) and the mixed-event background distributions (open circle) for 10 $p_T$ bins from peripheral events (60-100%) in p-Pb collisions. The values written above each figure indicate bin boundary of $p_T$ bin. . . . .	46
3.19	$\Xi^\mp\pi^\pm$ invariant mass distributions (full circle) and the mixed-event background distributions (open circle) for 7 $p_T$ bins from minimum-bias events in Pb-Pb collisions. The values written above each figure indicate bin boundary of $p_T$ bin. . . . .	47
3.20	$\Xi^\mp\pi^\pm$ invariant mass distributions (full circle) and the mixed-event background distributions (open circle) for 7 $p_T$ bins from central events (0-10%). The values written above each figure indicate bin boundary of $p_T$ bin. . . . .	48
3.21	$\Xi^\mp\pi^\pm$ invariant mass distributions (full circle) and the mixed-event background distributions (open circle) for 7 $p_T$ bins from semi-central events (10-40%) The values written above each figure indicate bin boundary of $p_T$ bin. . . . .	49
3.22	$\Xi^\mp\pi^\pm$ invariant mass distributions (full circle) and the mixed-event background distributions (open circle) for 7 $p_T$ bins from peripheral events (40-80%) The values written above each figure indicate bin boundary of $p_T$ bin. . . . .	50
3.23	Invariant mass distribution after subtraction of the mixed-event background in p-Pb collisions (left) and in Pb-Pb collisions (right). The solid curve represents the combined fit, while the dashed line describes the residual background. . . . .	51
3.24	Invariant mass distributions after subtraction of the mixed-event background in minimum-bias event in p-Pb collisions. The solid curve represents the combined fit, while the dashed line describes the residual background. . . . .	52

3.25	Invariant mass distributions after subtraction of the mixed-event background in central event (0-20%) in p-Pb collisions. The solid curve represents the combined fit, while the dashed line describes the residual background. . . . .	53
3.26	Invariant mass distributions after subtraction of the mixed-event background in 20-40% centrality interval in p-Pb collisions. The solid curve represents the combined fit, while the dashed line describes the residual background. . . . .	54
3.27	Invariant mass distributions after subtraction of the mixed-event background in 40-60% centrality interval in p-Pb collisions. The solid curve represents the combined fit, while the dashed line describes the residual background. . . . .	55
3.28	Invariant mass distributions after subtraction of the mixed-event background in peripheral event (60-100%) in p-Pb collisions. The solid curve represents the combined fit, while the dashed line describes the residual background. . . . .	56
3.29	Invariant mass distributions after subtraction of the mixed-event background from minimum-bias events in Pb-Pb collisions. The solid curve represents the combined fit, while the dashed line describes the residual background. . . . .	57
3.30	Invariant mass distributions after subtraction of the mixed-event background from central events (0-10%) in Pb-Pb collisions. The solid curve represents the combined fit, while the dashed line describes the residual background. . . . .	58
3.31	Invariant mass distributions after subtraction of the mixed-event background from semi-central event (10-40%) in Pb-Pb collisions. The solid curve represents the combined fit, while the dashed line describes the residual background. . . . .	59

3.32	Invariant mass distributions after subtraction of the mixed-event background from peripheral event (40-80%) in Pb-Pb collisions. The solid curve represents the combined fit, while the dashed line describes the residual background. . . . .	60
3.33	$\sigma$ fit parameters as a function of $p_T$ in MB in p-Pb collisions (left) and in Pb-Pb collisions (right). . . . .	61
3.34	$\Xi(1530)^0$ mass distribution as a function of $p_T$ in each multiplicity classes in p-Pb collisions (left) and the different centrality classes in Pb-Pb (right). The mass values are obtained from fit of the Voigtian function. . . . .	61
3.35	Raw spectra of $\Xi(1530)^0$ obtained by integrating the Voigtian fit function for different multiplicities in p-Pb collisions (top) and different centrality classes in Pb-Pb collisions (bottom). Only the statistical errors are reported. . . . .	62
3.36	Geometrical acceptance and the reconstruction efficiency ( $A \times \epsilon$ ) for $\Xi(1530)^0$ in $-0.5 < y_{CMS} < 0$ in p-Pb collisions. Only statistical uncertainties are shown. . . . .	63
3.37	Real corrected $\Xi(1530)^0$ spectrum is shown as black dots for the minimum-bias events with Lévy-Tsallis fit (black curve). The generated (un-weighted) spectrum are presented as blue dots and reconstructed (un-weighted) spectrum is shown as red squares. . . .	64
3.38	Efficiency as a function of $p_T$ in minimum bias events in p-Pb collisions. Statistical uncertainties are presented as bar. . . . .	65
3.39	Efficiency as a function of $p_T$ for different centrality classes in Pb-Pb collisions . . . . .	66
3.40	Corrected $p_T$ -spectra of $\Xi(1530)^0$ for NSD and different multiplicity classes in p-Pb collisions. . . . .	68



3.41	Corrected $p_T$ -spectra of $\Xi(1530)^0$ for different centrality classes in Pb-Pb collisions. . . . .	68
3.42	Summary of the contributions to the systematic uncertainty in minimum bias events in p-Pb collisions. The dashed black line is the sum in quadrature of all the contributions. . . . .	71
3.43	Systematic uncertainties for each multiplicity classes in p-Pb collisions. . . . .	72
3.44	Summary of the contributions to the systematic uncertainty in minimum bias events in Pb-Pb collisions. The dashed black line is the sum in quadrature of all the contributions. . . . .	72
3.45	Systematic uncertainties for each multiplicity classes. . . . .	73
4.1	Corrected $p_T$ -spectrum from NSD events and spectra from multiplicity dependent event classes in p-Pb collision system (top) and spectra in different centrality classes in Pb-Pb collision system (bottom). Statistical uncertainties are presented as bar and systematical uncertainties are plotted as boxes. . . . .	76
4.2	Ratio of $\Xi(1530)^0$ to $\Xi^-$ measured in pp [45], p-Pb [11, 19] and Pb-Pb collisions as a function of $\langle dN_{ch}/d\eta_{lab} \rangle$ measured at midrapidity. Statistical uncertainties (bars) are shown as well as total systematic uncertainties (hollow boxes) and systematic uncertainties uncorrelated across multiplicity (shaded boxes). A few model predictions are also shown as lines at their appropriate abscissa. . . . .	78
4.3	Ratio of $\Xi(1530)^0$ to $\Xi$ measured in Pb-Pb collisions as a function of $p_T$ at mid-rapidity. Statistical uncertainties (bars) are shown and total systematic uncertainties (boxes). . . . .	79

4.4	Ratio of $\rho/\pi$ for different system sizes in pp and Pb–Pb collisions. Statistical uncertainties (bars) are shown as well as total systematic uncertainties (hollow boxes) and systematic uncertainties uncorrelated across multiplicity (shaded boxes). . . . .	80
4.5	Ratio of $\Sigma(1385)^\pm$ for different system sizes in pp and p–Pb collisions (left) and ratio of $\Lambda(1520)/\Lambda$ in pp, p–Pb and Pb–Pb collisions (right). Statistical uncertainties (bars) are shown as well as total systematic uncertainties (hollow boxes) and systematic uncertainties uncorrelated across multiplicity (shaded boxes). . . . .	81
4.6	Double ratios of each resonances to ground-state hadrons obtained in central events divided by peripheral events in Pb–Pb collisions at $\sqrt{s_{NN}}=2.76$ TeV. Statistical uncertainties and systematic uncertainties are summed in quadrature. . . . .	82
4.7	Ratio of $\Xi(1530)^0$ to $\pi^\pm$ , measured in pp [47] and p–Pb [45] collisions, as a function of the average charged particle density ( $\langle dN_{ch}/d\eta_{lab} \rangle$ ) measured at mid-rapidity. Statistical uncertainties (bars) are shown as well as total systematic uncertainties (hollow boxes) and systematic uncertainties uncorrelated across multiplicity (shaded boxes). A few model predictions are also shown as lines at their appropriate abscissa. . . . .	84
4.8	Particle yield ratios to pions of strange and multi-strange hadrons normalized to the values measured in pp collisions, both in pp and in p–Pb collisions. The common systematic uncertainties cancel in the double-ratio. The empty boxes represent the remaining uncorrelated uncertainties. . . . .	85



4.9	Mean transverse momenta $\langle p_T \rangle$ of $\Lambda$ , $\Xi^-$ , $\Sigma^{*\pm}$ , $\Xi^{*0}$ and $\Omega^-$ in p-Pb collisions at $\sqrt{s_{NN}} = 5.02$ TeV as a function of mean charged-particle multiplicity density $\langle dN_{ch}/d\eta_{lab} \rangle$ , measured in the pseudorapidity range $ \eta_{lab}  < 0.5$ . The results for $\Lambda$ , $\Xi^-$ and $\Omega^-$ are taken from [11, 19, 23]. Results for $\Xi(1530)^0$ , the $\langle p_T \rangle$ obtained in pp collisions at $\sqrt{s} = 7$ TeV and Pb-Pb collisions at $\sqrt{s_{NN}} = 2.76$ TeV are also presented. Statistical and systematic uncertainties are represented as bars and boxes, respectively. . . . .	86
4.10	Mass dependence of the mean transverse momenta of identified particles for the 0-20% V0A multiplicity class and with $-0.5 < y_{CMS} < 0$ in p-Pb collisions at $\sqrt{s_{NN}} = 5.02$ TeV [11, 19], and in minimum-bias pp collisions at $\sqrt{s} = 7$ TeV [45] with $ y_{CMS}  < 0.5$ . Additionally, $D^0$ and $J/\psi$ results are plotted. The $D^0$ and $J/\psi$ were measured in different rapidity ranges: $ y_{CMS}  < 0.5$ [48] ( $ y_{CMS}  < 0.9$ [49]) for $D^0$ ( $J/\psi$ ) in pp and $-0.96 < y_{CMS} < 0.04$ [48] ( $-1.37 < y_{CMS} < 0.43$ [50]) for $D^0$ ( $J/\psi$ ) in p-Pb. Note also that the results for $D^0$ and $J/\psi$ in p-Pb collisions are for the 0-100% multiplicity class. . . . .	87
4.11	$p_T$ -integrated $K^*(892)^0/K$ and $\phi/K$ ratios in different collision systems. The yield ratios obtained different multiplicity event in pp collisions at $\sqrt{s} = 7$ TeV, in p-Pb collisions at $\sqrt{s_{NN}} = 5.02$ TeV and in Pb-Pb collisions at $\sqrt{s_{NN}} = 2.76$ TeV are shown in left figure with the results obtained from inelastic event in pp collisions. The same yield ratios but with different energies (pp at $\sqrt{s} = 13$ TeV, Pb-Pb at $\sqrt{s_{NN}} = 5.02$ TeV) are shown on right figure. . . . .	89

4.12	Ratio of $\Sigma(1385)^\pm$ to $\pi$ measured in pp [45, 47, 52, 53], dAu [52, 54] and pPb [11] collisions, as a function of the average charged particle density ( $\langle dN_{\text{ch}}/d\eta_{\text{lab}} \rangle$ ) measured at mid-rapidity. Statistical uncertainties (bars) are shown as well as total systematic uncertainties (hollow boxes) and systematic uncertainties uncorrelated across multiplicity (shaded boxes). A few model predictions are also shown as lines at their appropriate abscissa. . . . .	90
4.13	System size dependence of the mean transverse momentum of $K^*(892)^0$ compared to that of the proton (left panel) and $\langle p_T \rangle$ of $\phi$ compared to that of the proton (right panel). The system size is defined as the cubic root of the average charged particle multiplicity density measured in the ALICE central barrel ( $ \eta  < 0.5$ ) in pp at $\sqrt{s} = 7$ TeV (green), p-Pb at $\sqrt{s_{\text{NN}}} = 5.02$ TeV (blue) and Pb-Pb at $\sqrt{s_{\text{NN}}} = 2.76$ TeV (red). Statistical uncertainties are represented as bars, boxes indicate total systematic uncertainties. . . . .	91
4.14	Mass dependence of the mean transverse momenta of identified particles and predictions from EPOS v3 with UrQMD OFF and ON for central (0-10%) Pb-Pb collisions at $\sqrt{s_{\text{NN}}} = 2.76$ TeV. . . . .	93

# Study of the Multi-strange Resonance $\Xi(1530)^0$ Production with ALICE at the LHC Energies

Jihye Song

Department of Physics  
The Graduate School  
Pusan National University

## Abstract

The primary goal of the relativistic heavy-ion physics program at Large Hadron Collider (LHC) at CERN, Geneva, Switzerland is to study the nuclear matter under extreme conditions. The measurement of resonances in ultra-relativistic heavy-ion collisions allows one to study the properties of the hadronic medium. Resonances with short lifetimes compared to the duration of the time span between chemical and kinetic freeze-out are good candidates to prove the interplay of particle re-scattering and regeneration in the hadronic phase, which result in a modification of their measured yields.

The ALICE detector and its subsystem used for the analysis presented in this thesis are explained. Particle identification method and a coordinate system of ALICE are provided.

Measurements of multi-strange resonance  $\Xi(1530)^0$  were performed with the ALICE detector in pp, p-Pb and Pb-Pb collisions at the LHC energies.

The  $p_T$ -spectra of  $\Xi(1530)^0$  are obtained and compared with model predictions. The yield ratios of  $\Xi(1530)^0$  to stable hadrons are shown and discussed. Mean transverse momentum of  $\Xi(1530)^0$  has been investigated and compared with that of identified hadrons. The comparison of results obtained for other resonances is also presented in this thesis.

# Chapter 1

## Introduction

The main objective of relativistic heavy-ion physics is to study the nuclear matter under extreme conditions such as high temperature and energy density. The phase in high temperature or large baryon density allows one to produce a system of quarks and gluons. In this chapter, the matter created by ultra-relativistic heavy-ion collisions is introduced, and physical observables and collisions systems used in this thesis, are shortly explained.

### 1.1 Matter under extreme conditions

Inside of the hadrons, the quarks are confined by the strong interactions which can be explained by the Quantum Chromo Dynamics (QCD) theory [1]. The Lattice QCD (LQCD) calculations suggest the existence of different phases depending on the temperature and baryon density [2]. When high temperature and/or high baryon-density is obtained, the confinement of the quarks and gluons can be broken so that they lose their hadronic binding and become quasi-free particles. This state is called as Quark-Gluon Plasma (QGP) [3]. Figure 1.1 is a QCD phase diagram in temperature versus net baryon density.

Ultra-relativistic heavy-ion collisions allow forming the QGP because they produce a large number of binary nucleon-nucleon collisions taking place in a very small spatial region. Consequentially, temperature, pressure and energy density reach to be enable us to study the new state of matter under extreme conditions.

Figure 1.2 presents a scenario of the space-time evolution of ultra-relativistic



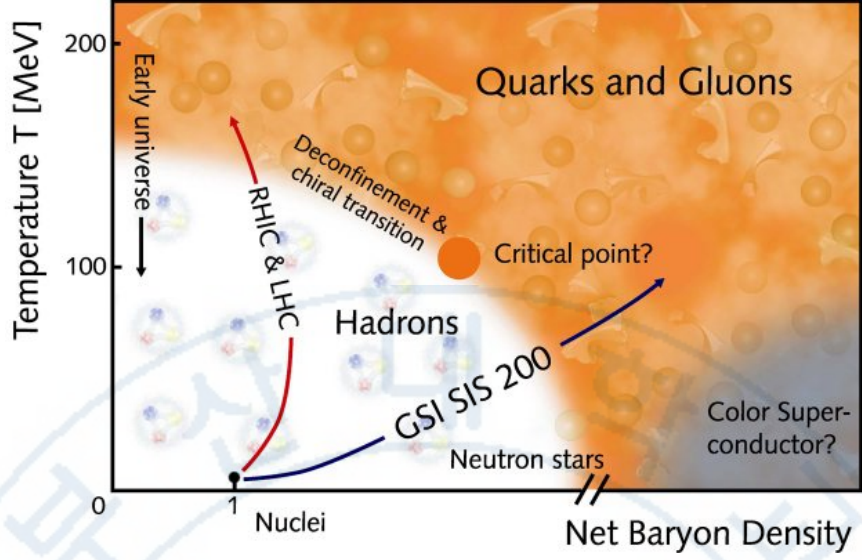


Figure 1.1: QCD phase diagram of nuclear matter as functions of temperature and baryon density [4].

heavy-ion collisions.

After being accelerated by Large Hadron Collider [5], ions are traveling with a velocity very close to the speed of light. Due to the Lorentz contraction, they appear as thin disks just before the collisions, as shown in the left bottom of Figure 1.2. Just at the moment of collision, a large amount of energy is deposited in a small volume of space and in a short duration of time [6].

During the period that takes a fraction of  $1 \text{ fm}/c$  (pre-equilibrium stage), quarks and gluons are produced. At the proper time  $\tau_0$ , the system composed by quarks and gluons is expected to be equilibrated. The system expands and gradually cools down by elastic and inelastic collisions (expansion stage,  $1 \lesssim \tau \lesssim 10 \text{ fm}/c$ ). The temperature of the QGP decreases while expanding due to its internal pressure, until it reaches the critical temperature  $T_c$ . Once such temperature is reached, the QGP begins to convert into hadron gas. From the LQCD calculation, it is expected that transition from the QGP to the hadronic matter at zero baryon chemical potential is of crossover type [7, 8, 9] and  $T_c$  is very close to the chemical freeze-out temperature,  $T_{ch}$ , where the abundance of hadrons is fixed.

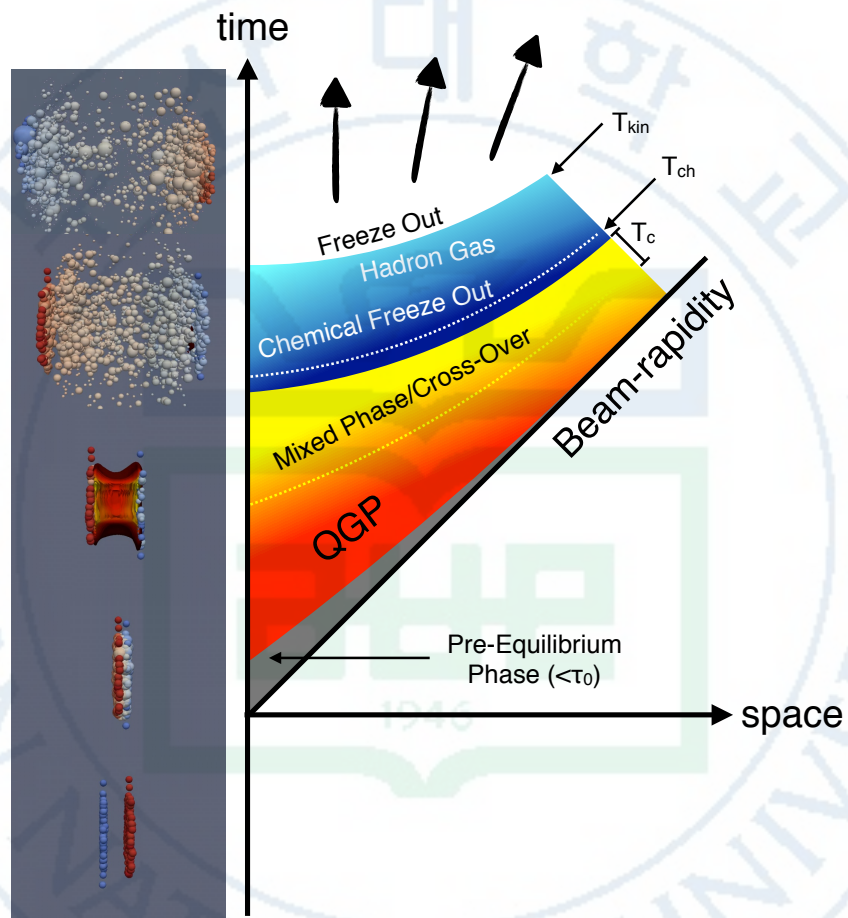


Figure 1.2: A schematic view of the evolution of an ultra-relativistic heavy-ion collision.



As a consequence, the ratios between production rates of different particle species can provide information on the system at this stage. (Pseudo-)Elastic interactions can still be present and continue to modify the kinetic properties of produced hadrons. When the distances between hadrons are larger than the range of the interaction, (pseudo-)elastic collisions also stop and the kinetic freeze-out is reached ( $T_{kin}$ ). Then, the kinematical distribution of the hadrons is fixed. Hence, the information on the kinetic freeze-out temperature can be obtained from the hadrons momentum spectra. When  $\tau \gtrsim 15 \text{ fm}/c$  [10], the hadrons freely stream out to the detectors. Experimental measurements of various particles which have experienced the different stages of the ultra-relativistic heavy-ion collision evolution allow us to study the properties of hot matter such as particle production mechanisms, strangeness enhancement and various information associated to the hadronic phase.

## 1.2 Collision systems and physical observables in experiment

In order to study properties of matter under extreme conditions, the ALICE has accumulated the data from high-energy Pb–Pb, p–Pb and pp collisions. From the Pb–Pb data, the properties of the QGP are investigated, whereas the results obtained with p–Pb collisions provide information on cold matter and help to disentangle cold matter effect from the hot matter produced in Pb–Pb collisions. Results derived from minimum bias pp collisions are commonly used as a reference for p–Pb and Pb–Pb collisions.

Recent measurements have, however, revealed striking similarities across different systems. There are some hints for collectivity in the small systems and a smooth evolution is observed for particle production from pp, p–Pb, peripheral Pb–Pb collisions to central Pb–Pb collisions [11]. In order to compare the results

from different collision systems, global observables should be introduced such as i.e., “charged-particle multiplicity density” [12].

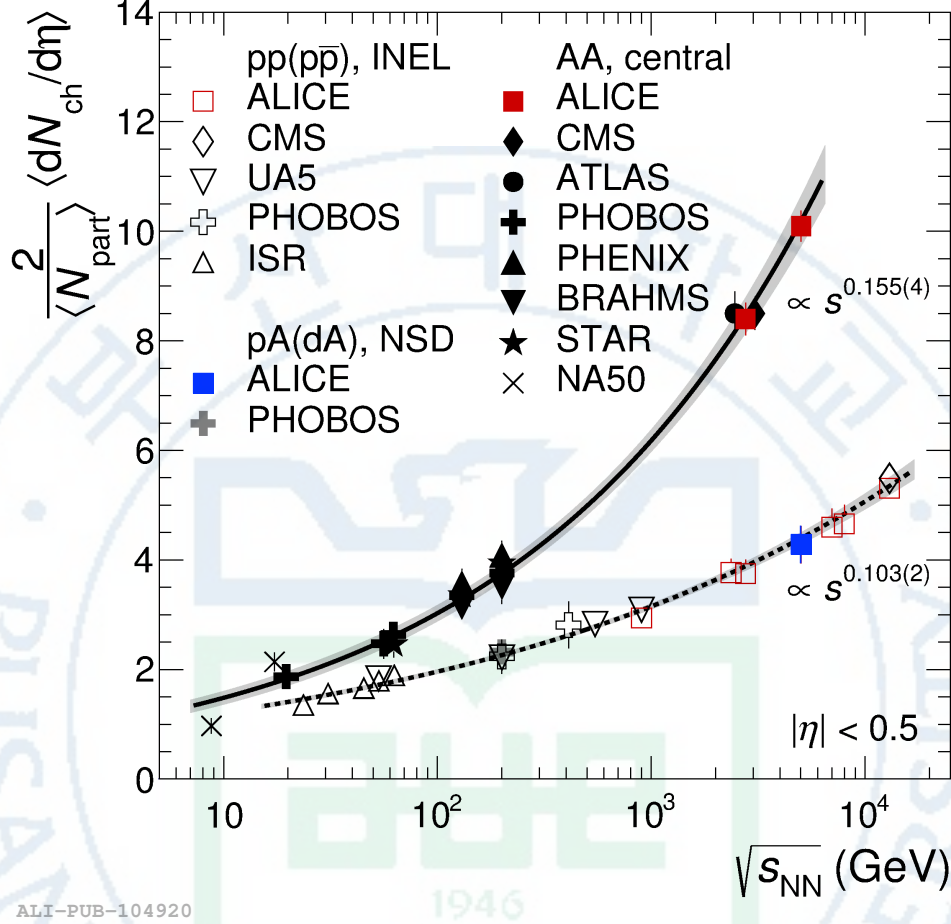


Figure 1.3: Values of  $\langle dN_{ch}/d\eta \rangle$  as a function of  $\sqrt{s_{NN}}$ . Measurements for inelastic  $pp(p\bar{p})$  collisions as a function of  $\sqrt{s}$  are also shown along with those from Non-Single Diffractive (NSD) p-A and d-A collisions. The energy dependencies of the AA and  $pp(p\bar{p})$  collision data are well described by the functions  $s_{NN}^{0.155}$  (solid line) and  $s_{NN}^{0.103}$  (dashed line), respectively. The shaded bands show the uncertainties on the extracted power-law dependencies. The central Pb-Pb measurements from CMS and ATLAS at 2.76 TeV have been shifted horizontally for clarity [12]. Note that, the color of point for NSD in p-A collision is changed to blue to emphasize.

The “charged-particle multiplicity density”,  $dN_{ch}/d\eta$ , is defined by the number of charged particles produced at mid-rapidity ( $|\eta| < 0.5$ ) and can be related to the collision system size and the energy [12]. Systems produced in different collisions such as pp, p-Pb and Pb-Pb at different energies can be classified by

using  $dN_{ch}/d\eta$  which is a basic quantity which enables one to also investigate the colliding energy dependence.

Averaged values of  $dN_{ch}/d\eta$  normalized to half of  $\langle N_{part} \rangle$  (averaged number of participating nucleons, calculated with a Glauber model [12]) from inelastic pp, Non-Single Diffractive (NSD) p(d)-A (“A” represent heavy-ion, such as Au and Pb) and central AA collisions are shown in Figure 1.3. For  $\Xi(1530)^0$  resonance production which will be discussed in this thesis, the data samples from p-Pb collisions at  $\sqrt{s_{NN}} = 5.02$  TeV and Pb-Pb collisions at  $\sqrt{s_{NN}} = 2.76$  TeV were analyzed. Corresponding  $\frac{2}{\langle N_{part} \rangle} \langle dN_{ch}/d\eta \rangle$  values are shown as blue square for Non-Single Diffractive (NSD) events in p-Pb collisions and red square for central Pb-Pb collisions.

As results,  $p_T$ -integrated particle yield ratios and  $\langle p_T \rangle$  will be discussed and presented as a function of  $\langle dN_{ch}/d\eta \rangle$  to see the colliding system size dependence. The  $\langle dN_{ch}/d\eta \rangle$  values used for this analysis will be provided in section 2.2 with additional information about its definition.

## 1.3 Resonance and hyperon production

### 1.3.1 Study of hadronic phase

Resonances are hadrons which have the same quark contents with its ground state particle but different excited quantum states, and therefore larger masses [13]. The resonances usually have a short lifetime in the order of a few fm/c which is comparable to the lifetime of the fireball created by heavy-ion collisions [13]. The short lifetime is a property of resonances and makes resonances one of the good tools to investigate hadronic medium between chemical and kinetic freeze-out [14].

In heavy-ion collisions, the hadronic resonances which are produced during the expansion could interact with the medium. The resonances are measured only via the reconstruction of their decay products in detectors.

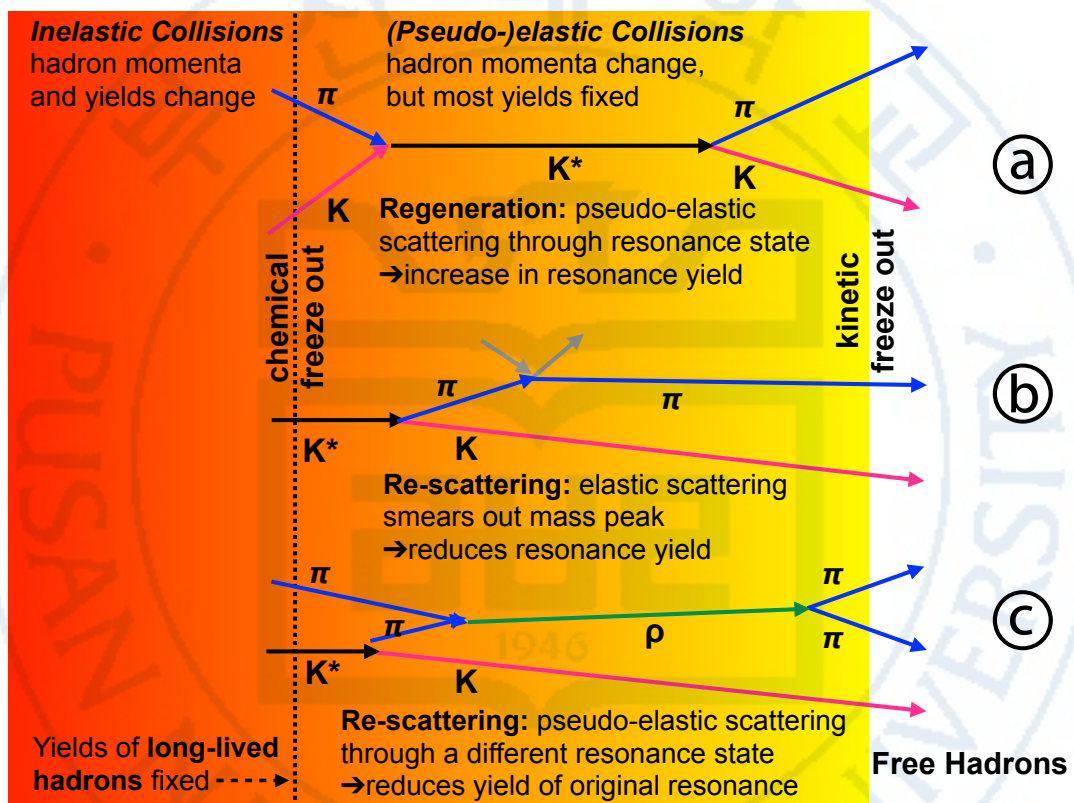


Figure 1.4: Possible interactions of resonances during the hadronic phase.

Figure 1.4 shows the scheme of possible interactions during the hadronic phase. In the time duration between the chemical and the kinetic freeze-out, hadron momenta still can be changed while most of the particle yields are fixed. Resonances can possibly decay during this stage due to their short lifetime and process such as (pseudo-)elastic collisions can also occur.

A sketch of the possible scenarios leading to different yields starting from the initial production until kinetic freeze-out is shown in Figure 1.4. The decay channel shown here corresponds to the  $K^*(892)^0$  resonance which decay is  $K^*(892)^0 \rightarrow \pi^- + K^+$ . Because of the pseudo-elastic collisions, the  $K^*(892)^0$  can be partially regenerated during the hadronic phase from  $\pi$  and  $K$  which were produced at chemical freeze-out (Ⓐ in Figure 1.4). On the other hand, if decay products of the  $K^*(892)^0$  undergo elastic scattering (Ⓑ in Figure 1.4) or pseudo-elastic scattering (Ⓒ in Figure 1.4), the initial  $K^*(892)^0$  can not be reconstructed using the invariant mass technique of the  $(\pi, K)$  daughters. As a result, the observed yield after kinetic freeze-out can be more larger or smaller than the yield originally produced. If the regeneration effect would be dominant than the re-scattering effect, the yield should increase. Conversely, the yield observed after kinetic freeze-out can decrease if re-scattering effect is predominant. The final resonance yield depends on the lifetimes of resonances and the duration of the hadronic phase which can be connected to the temperature of the chemical/kinetic freeze-out.

In order to investigate how the hadronic phase affects the yields of resonance particles, resonances having different lifetimes were studied for different collision systems. In particular, it will be shown that the integrated yield-ratios between resonances with various lifetimes and their ground state particle provide valuable insights on the role of the regeneration and re-scattering processes.

Figure 1.5 presents integrated yield-ratio of  $K^{*0}/K$  and  $\phi/K$  as a function of  $\langle dN_{ch}/d\eta_{lab} \rangle^{1/3}$  [15]. As shown in Figure 1.5, the ratio of  $K^{*0}/K$  is suppressed in central Pb–Pb collisions with respect to the peripheral Pb–Pb collisions and



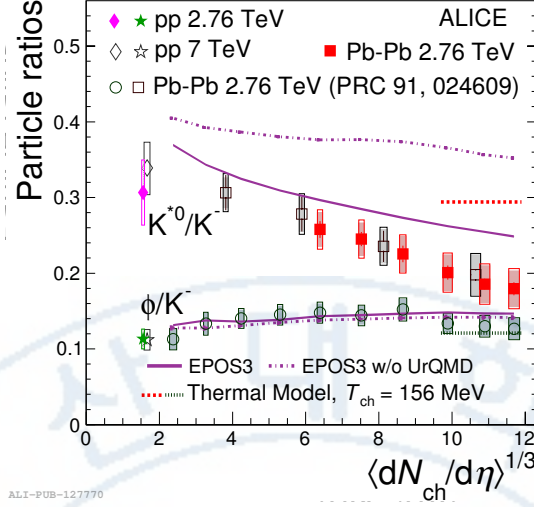


Figure 1.5: Ratios of  $K^{*0}/K^-$  and  $\phi/K^-$  with system size measured at mid-rapidity in pp and Pb–Pb collisions. Statistical uncertainties (bars) are shown as well as total systematic uncertainties (hollow boxes) and systematic uncertainties uncorrelated across multiplicity (shaded boxes). A few model predictions are also shown as lines at their appropriate abscissa [15].

with a value lower than thermal model predictions, whereas  $\phi/K$  ratio does not show such a suppression and remains consistent with thermal model [15]. The decreasing trend of the ratio which was observed on  $K^{*0}/K$  was suggested as an indication of the abundance of re-scattering processes in the hadronic medium.

Table 1.1 presents a list of particles with their lifetime, valence quark contents, branching ratios (BR) and decay modes used in analyses. Among them, **the  $\Xi(1530)^0$  resonance is one of the good candidates to study hadronic phase since it has a lifetime between  $K^*(892)^0$  and  $\phi(1020)^0$** . From the measurement of  $\Xi^-$  and its excited state  $\Xi(1530)^0$ , the integrated particle-ratio of  $\Xi(1530)^0$  to  $\Xi^-$  can be extracted similarly to the  $K^*(892)^0$  and  $\phi(1020)^0$ . If re-scattering is dominant for  $\Xi(1530)^0$ , the trend of  $\Xi(1530)^0/\Xi^-$  could have similar behavior as  $K^*(892)^0$ . On the other hand, if regeneration is the predominant process, the ratio would be approximately constant with system size. The results of  $\Xi(1530)^0/\Xi^-$  will be compared with other particle yield ratios ( $\rho/\pi$ ,  $K^*/K$ ,  $\Lambda^*/\Lambda$ ,  $\phi/K$ ) and discussed with model predictions.



	$c\tau$ (fm)	quark content	Decay modes	BR [%]
$\rho(770)^0$	1.3	$(u\bar{u}+d\bar{d})/\sqrt{2}$	$\pi^+ + \pi^-$	100
$K^*(892)^0$	4.2	$d\bar{s}$	$K^+ + \pi^-$	66.6
$\Sigma^*(1385)^+$	5.5	$uus$	$\Lambda\pi^+ \rightarrow (p\pi^-)\pi^+$	87.0
$\Lambda^*(1520)$	12.6	$uds$	$p + K^-$	22.5
$\Xi^*(1530)^0$	21.7	$uss$	$\Xi^- \pi^+ \rightarrow (\Lambda\pi^-)\pi^+ \rightarrow ((p\pi^-)\pi^-)\pi^+$	66.7
$\phi(1020)^0$	44	$s\bar{s}$	$K^+ + K^-$	48.9

Table 1.1: Lifetime of the measured resonances with their quark content, decay modes exploited for the measurements presented here and branching ratios [16].

### 1.3.2 Hyperon production

The particles to be discussed in this thesis are regarding one of the special family that contains at least one strange valence quark, but not heavier quarks (like charm or bottom) and they are called as hyperon. As examples,  $\Lambda(uds)$ ,  $\Xi^-(dss)$ ,  $\Omega(sss)$  and the corresponding antiparticles and also their excited state of particles (e.g.,  $\Lambda(1520)$ ,  $\Sigma(1385)^\pm$  and  $\Xi(1530)^0$ ) are hyperons. They have been studied extensively over past decades in connection with the study of QGP by evaluating at the strangeness production [17]. It was found that in high energy nucleus-nucleus (A–A) collisions at the Super Proton Synchrotron (SPS), the Relativistic Heavy Ion Collider (RHIC) and the Large Hadron Collider (LHC) the abundances of hyperons are compatible with those from thermal statistical model calculations [18]. In smaller collision systems such as pp and p–A collisions, relative abundance of hyperons is lower with respect to A–A collisions [19]. This effect is known as canonical suppression. The more strange valence quarks within the hadron, the larger the effect (i.e., higher strangeness) [20].

ALICE has measured hyperons in different collision systems, pp, p–Pb and Pb–Pb to investigate the production mechanism as a function of system size. The integrated yields of hyperon are normalized by the yields of non-strange hadron,  $\pi$ , at the same  $\langle dN_{ch}/d\eta \rangle$  as shown in Figure 1.6. The ratios of  $\Xi/\pi$  and  $\Omega/\pi$  in Pb–Pb collisions reach values that are consistent with thermal model predictions [21], while these ratios smoothly increase from pp to p–Pb collisions with  $\langle dN_{ch}/d\eta \rangle$

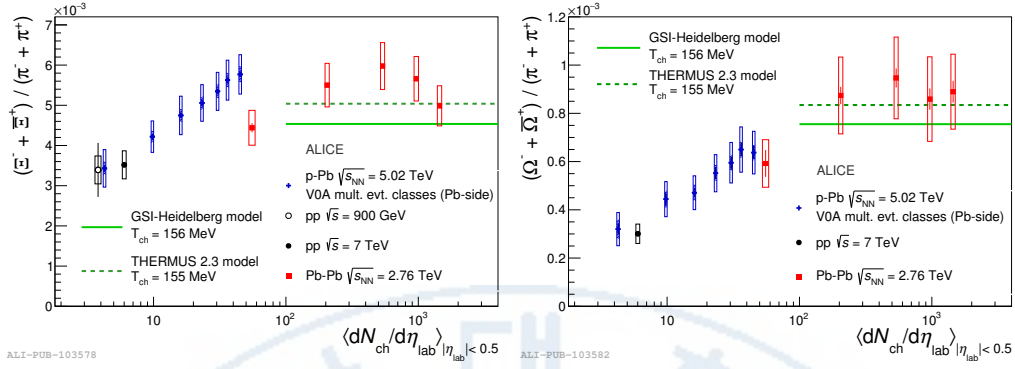


Figure 1.6:  $\Xi/\pi$  (left) and  $\Omega/\pi$  (right) ratios as a function of charged particle multiplicity densities in pp at 7 TeV, p-Pb at 5.02 TeV and Pb-Pb collisions with 2.76 TeV [19].

because of canonical suppression in small collision systems [19].

It is important to distinguish if the increase observed from small systems is related to the **strangeness valence quark content** or to the **mass of the hadron**. In order to understand the increasing trend in the small systems, particle ratios having different strange quark are compared as shown in Figure 1.7. It summarizes of the dynamical evolution of multiplicity-dependent particle production relative to the pp collisions. Figure 1.7 presents the yield ratios to pions divided by the values measured in INEL>0 (event selection that contains inelastic events with at least one charged particle in  $|\eta| < 1$ ) pp collisions, both for pp and p-Pb results. The observed multiplicity-dependent enhancement with respect to the INEL>0 sample follows a hierarchy connected to the hadron strangeness content.

This hierarchy could also originate from the mass ordering of hadrons. Because the particles on numerator have an increasing mass ( $M_p < M_\Lambda < M_\Xi < M_\Omega$ ), the increasing yields might be directly connected to the mass. In order to confirm that the effect is due to the strangeness content and not to the hadron mass, particles having same strangeness content but different masses have to be compared. **The  $\Xi(1530)^0$  is one of the crucial candidates to check this hypothesis because the  $\Xi(1530)^0$  has double strangeness same to  $\Xi$  but**

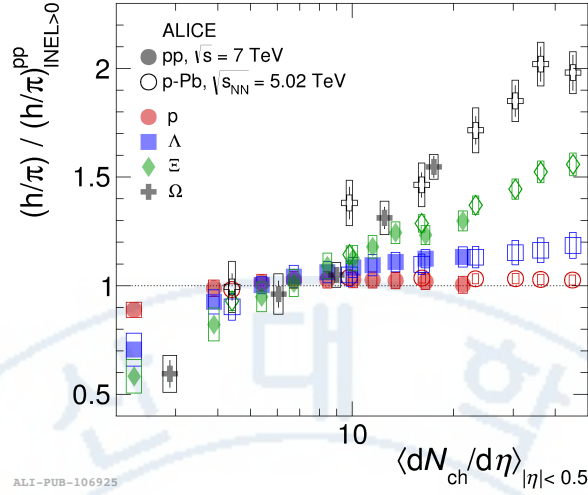


Figure 1.7: Particle yield ratios to pion of strange and multi-strange baryons and protons normalized to the values measured in the inclusive pp sample in both pp and in p-Pb collisions [22].

it decays strongly and have a larger mass with  $\Delta M \sim 210 \text{ MeV}/c^2$ .

### 1.3.3 Mean transverse momentum

From the measurement of  $p_T$ -spectra of identified particles, one can obtain relevant information not only from the integrated yield but also via mean transverse momentum of each particle. In a hydrodynamical evolving system, the spectral shapes are driven by the expansion velocity, thus by the hadron mass, so they are expected to follow a mass ordering. Vice-versa, the observation of mass ordering of particle spectra may be suggestive of the presence of collective (hydrodynamic) behavior of the expanding system.

The mean transverse momentum of identified hadrons in p-Pb collisions at 5.02 TeV as a function of  $\langle dN_{ch}/d\eta_{lab} \rangle$  is shown in the left panel and the measurements in pp at 7 TeV and the results from Pb-Pb collisions at 2.76 TeV are presented the right panel in Figure 1.8. The results in p-Pb collisions show that the mean transverse momentum increases with  $\langle dN_{ch}/d\eta_{lab} \rangle$  and the particle having larger mass have higher  $\langle p_T \rangle$ . The results in central Pb-Pb collisions also give

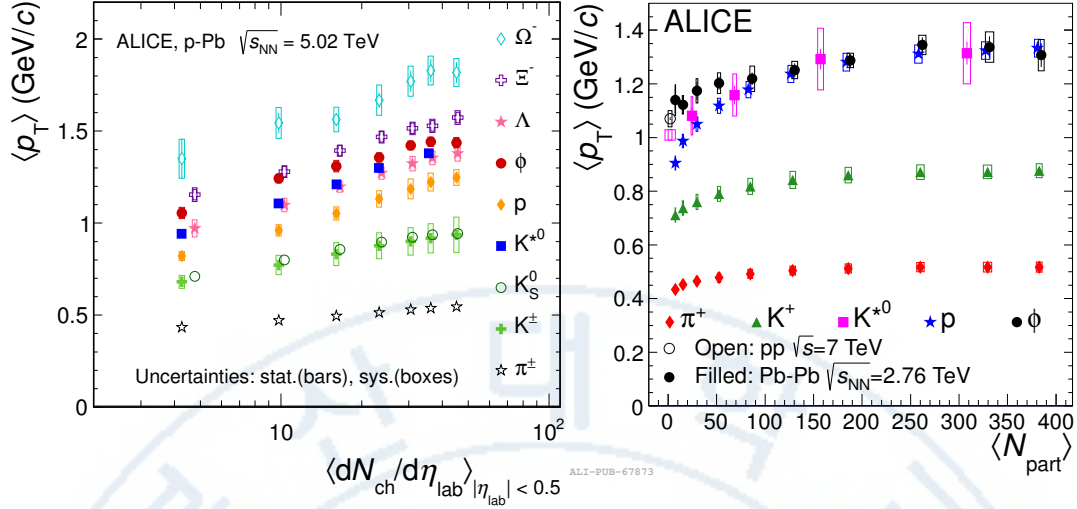


Figure 1.8: Mean transverse momentum of identified particles measured by ALICE in p-Pb collisions (left) and, in pp and Pb-Pb collisions (right) as a function of the charged particle density measured in the pseudo-rapidity range  $|\eta| < 0.5$ . Statistical uncertainties are represented as bars, whereas boxes indicate systematic uncertainties [23, 24].

the same mass ordering of mean transverse momentum.

The  $\langle p_T \rangle$  also can be used as a tool to probe interplay of re-scattering and regeneration in hadronic phase. As discussed in Section 1.3.1, the shape of spectra can be changed due to (pseudo-)elastic scattering during the hadronic phase. Correspondingly, the  $\langle p_T \rangle$  is affected by the existence of re-scattering and regeneration. EPOS v3 predicts an increase in  $\langle p_T \rangle$  of about 200-300 MeV/c due to interactions in the hadronic phase for most of the resonances and proton [25]. A modest increase in  $\langle p_T \rangle$  is however predicted for  $\phi$  and  $\Xi(1530)^0$  because of lower interaction rate in the hadronic medium of the daughter particles due to comparatively long lifetimes. In addition, a larger regeneration of the  $\Xi(1530)^0$  from the  $\Xi\pi$  channel is expected which compensates the signal loss in the low momenta region [25]. **The results of  $\langle p_T \rangle$  for the  $\Xi(1530)^0$  will be discussed in Section 4.3 and compared with the other particles and model predictions. The  $\langle p_T \rangle$  of  $\Xi(1530)^0$  complements previous measurements for strange and non-strange hadrons.**



## Chapter 2

# A Large Ion Collider Experiment at the LHC

A Large Ion Collider Experiment (ALICE) is one of the major experiments at Large Hadron Collider (LHC) which is a two ring superconducting hadron accelerator at CERN close to Geneva [26]. Figure 2.1 shows several experiments at CERN, the accelerator complex as well as the location of the ALICE.

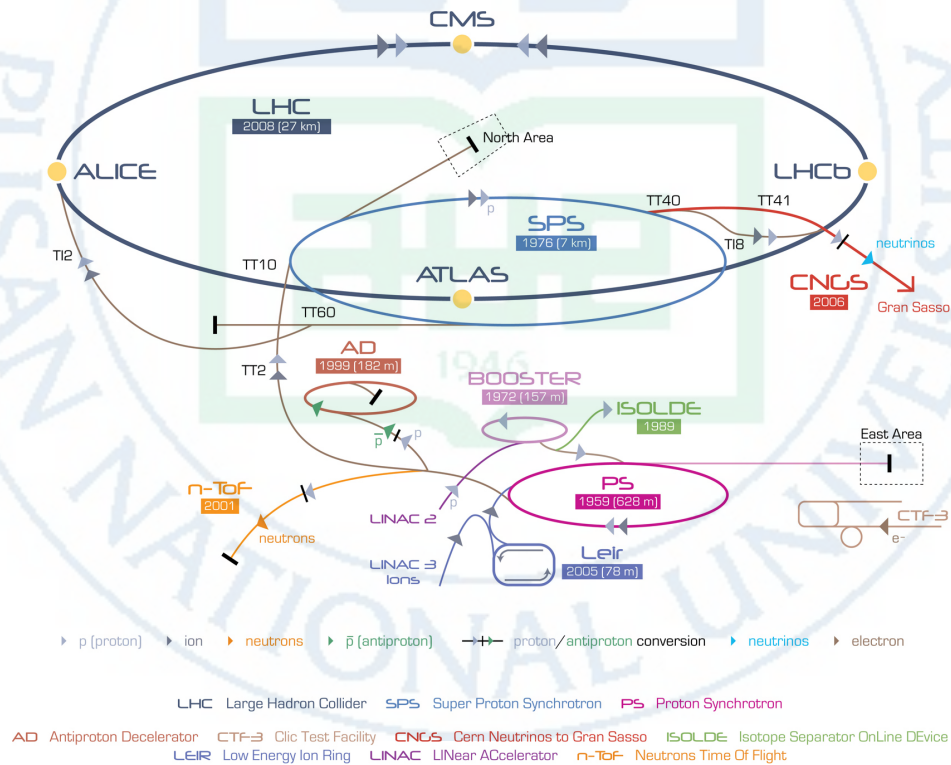


Figure 2.1: The CERN accelerator complex

The ALICE had accumulated data during the whole first phase of the LHC operation, from the end of 2009 to the beginning of the technical shutdown in 2013



(Run1). During that period of time, the LHC provided pp collisions at 0.9, 2.76, 7 and 8 TeV, p–Pb collisions at 5.02 TeV and Pb–Pb collisions at 2.76 TeV. Then, ALICE has carried out data taking of each collision systems with twice larger beam energies from 2015 in Run2 period. ALICE is designed to record nucleus-nucleus collisions and to investigate strongly interacting matter at very high energy density [27, 28].

The purpose is to understand the nature of the phase transition from hadronic matter to the QGP which was proposed by lattice QCD calculations. By design, ALICE is able to cope with the large multiplicities associated with Pb–Pb collision and at the same time has to cover as many QGP-related observables as possible. In comparison with the other experiments, ALICE can provide an excellent Particle IDentification (PID) performance at low transverse momenta and tracking with a very low material budget at mid-rapidity [26, 29]. PID is obtained by a combination of different techniques corresponding to various detectors which are optimized in different momentum regions [26].

## 2.1 The ALICE detector

The ALICE is a complex of 18 detector subsystems (Figure 2.2) that can be categorized into three groups [26, 28].

**Group 1. Central detectors** are installed in a solenoid magnet which provides 0.5 T magnetic field and covered pseudo-rapidity interval of  $-0.9 < \eta < 0.9$ . The central detectors are mainly used for the vertex reconstruction, tracking, particle identification and momentum measurement. From interaction region to outer region of the detector, there are several detectors listed below:

- Inner Tracking System (ITS)
- Time Projection Chamber (TPC)
- Transition Radiation Detector (TRD)

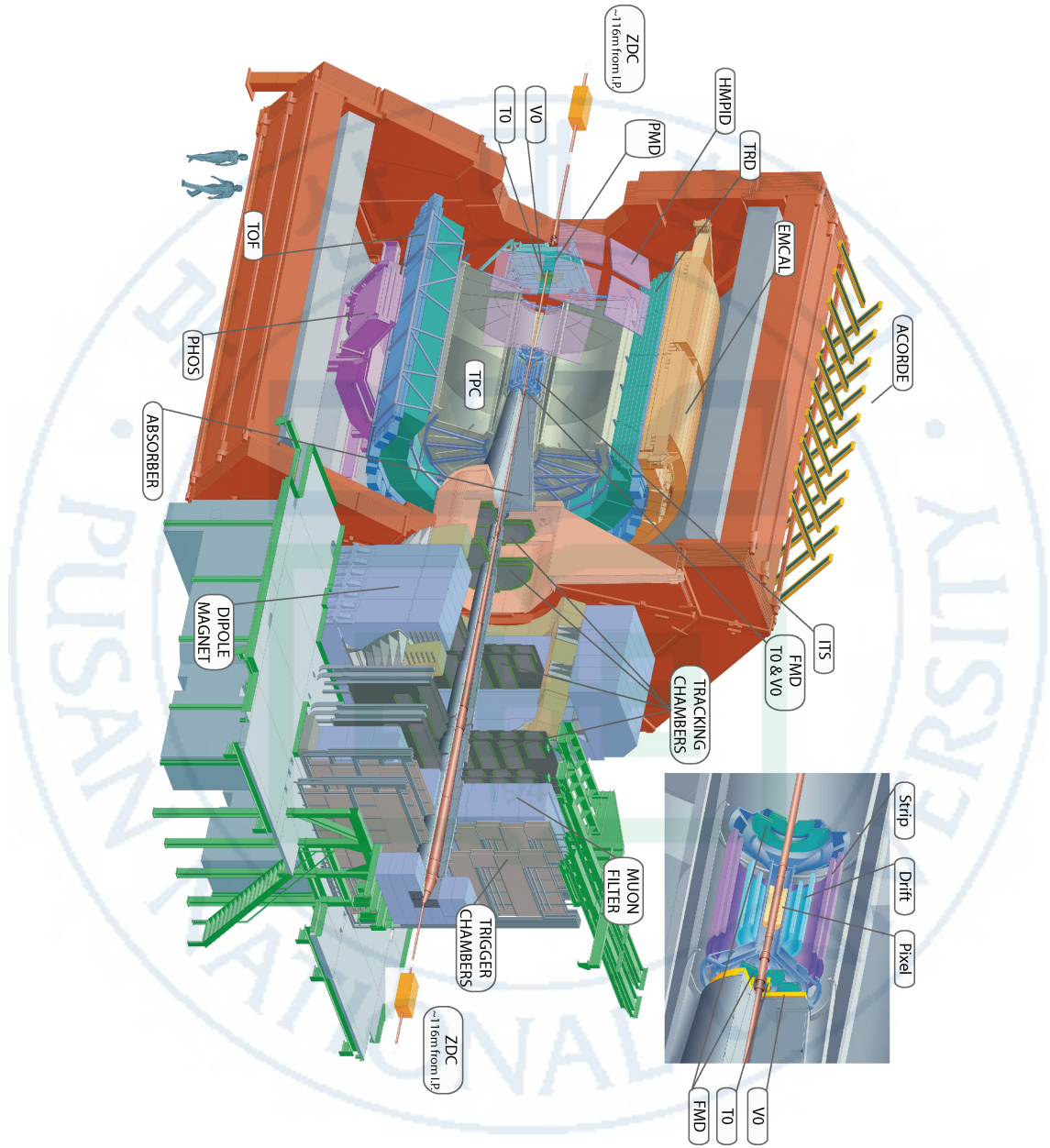


Figure 2.2: The ALICE experimental setup and detectors [28].

- Time Of Flight (TOF)

Following three detectors have limited azimuthal acceptance in the mid-rapidity region:

- High Momentum Particle Identification Detector (HMPID)
- PHOton Spectrometer (PHOS)
- ElectroMagnetic CALorimeter (EMCAL)

**Group 2. Muon spectrometer** is located in the forward pseudo-rapidity region ( $-4.0 < \eta < -2.5$ ) and is made up of a dipole magnet and tracking/trigger chambers. It has been optimized and configured to measure muons and to reconstruct heavy quark resonances such as  $J/\Psi$  through their  $\mu^+\mu^-$  decay channels.

**Group 3. Forward detectors** are placed in the high pseudo-rapidity area (small angles with respect to the beam pipe). They are used to measure and to trigger global event characteristics.

- Time Zero (T0) measures the time of events with a precision of the order of tens of picoseconds, as needed by TOF.
- VZERO (V0) is used to trigger minimum bias events and rejects the backgrounds coming from the beam-gas interaction.
- Forward Multiplicity Detector (FMD) gives multiplicity information and it covers large fraction of the solid angle ( $-3.4 < \eta < -1.7$  and  $1.7 < \eta < 5$ ).
- Photon Multiplicity Detector (PMD) measures the spatial distribution of photons on an event-by-event basis in  $2.3 < \eta < 3.7$  region.
- Zero Degree Calorimeter (ZDC) is used to measure and trigger on the impact parameter. The ZDC consists of two calorimeters, one for neutrons

(ZDC:ZN) and another one for protons (ZDC:ZP), and also includes an electromagnetic calorimeter (ZEM).

The TPC is the main tracking detector used for the analysis in this thesis, and further information is provided below.

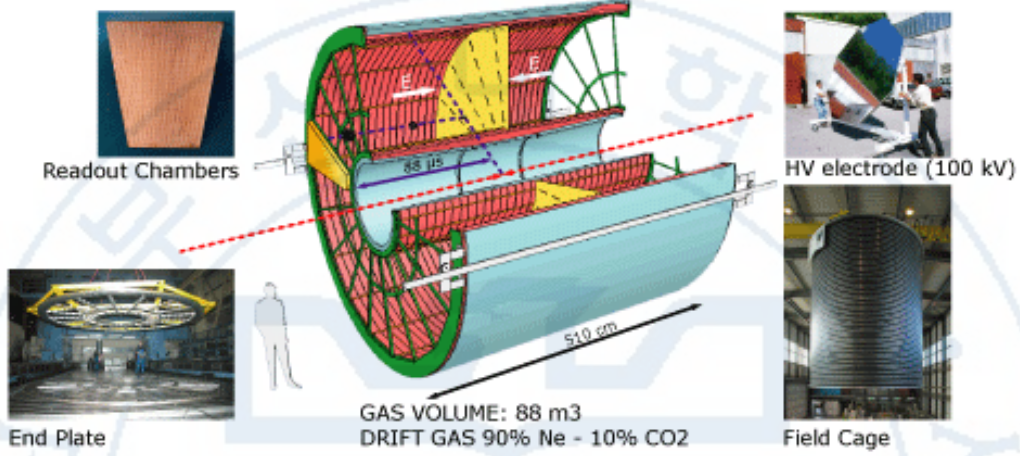


Figure 2.3: Schematic view of the TPC

The TPC [29] shown in Figure 2.3 is the main tracking detector of the central barrel optimized to measure the charged-particle's momentum with excellent track separation. It also has a good capability of the particle identification and vertex determination. The TPC was designed to have excellent tracking performance in the high multiplicity environment of Pb–Pb collisions. For such a reason, it was constructed as a drift chamber of cylindrical shape and a length of 5 m. The inner radius ( $r_{in}$ ) of  $\sim 85$  cm is decided by the maximum acceptable track density, and the outer radius ( $r_{out}$ ) of  $\sim 250$  cm by the minimum track length for which  $dE/dx$  is  $< 10\%$ . The volume of TPC is  $90 \text{ m}^3$  filled by Ne (90%)/CO<sub>2</sub> (10%) [28, 29]. The readout chambers are installed at the two endplates of the cylinder. Their design is based on the Multi-Wire Proportional Chamber (MWPC) technique with pad readout.

A low material budget and a rather low magnetic field (0.5 T) are the require-



ments to optimize the ALICE detector for tracking and particle identification down to very low momenta ( $p \geq 100 \text{ MeV}/c$ ) [29]. The transverse momentum resolution in p-Pb collisions for TPC standalone and ITS-TPC combined tracks is shown in Figure 2.4 [26].

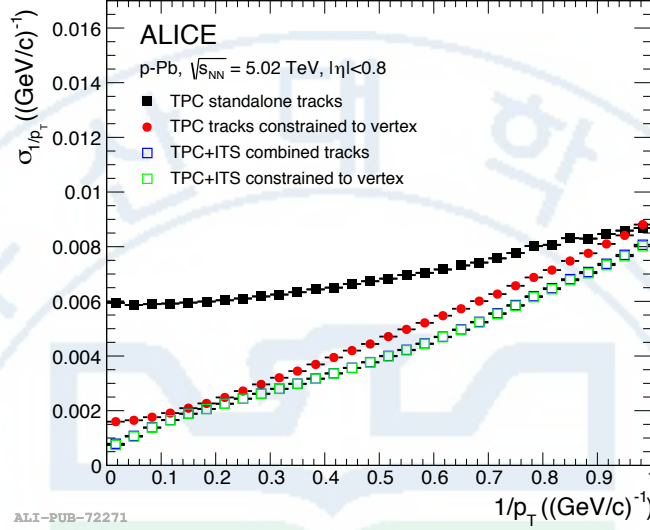


Figure 2.4: The  $p_T$  resolution for standalone TPC and ITS-TPC matched tracks with and without constraint to the vertex. [26].

Figure 2.5 shows transverse momentum resolution in the central rapidity region ( $|\eta| < 0.8$ ) in Pb-Pb collisions for TPC tracks combined with hits in the ITS. As shown in the Figure 2.5, a transverse momentum resolution of  $\sigma(p_T)/p_T = 20\%$  at  $p_T = 100 \text{ GeV}/c$  was achieved in Pb-Pb collisions at  $\sqrt{s_{NN}} = 2.76 \text{ TeV}$ .

### 2.1.1 Particle identification in the TPC

The TPC provides Particle IDentification (PID) for charged tracks. The gas in the detector is ionized by charged particle traveling through the chamber. In order to identify a particle, the physics observable which is required is energy loss per unit length within the matter crossed by the charged particle. This specific energy loss denoted by  $dE/dx$ , is described by Beth-Bloch parameterization (see eq. 2.1) that highlights the key of the identification technique. The  $dE/dx$  depends



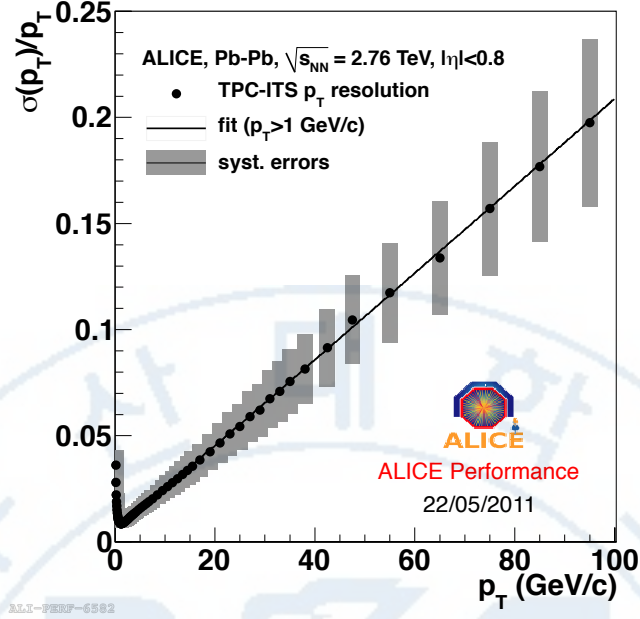


Figure 2.5: Transverse momentum resolution in the central rapidity region ( $|\eta| < 0.8$ ) for TPC tracks combined with hits in the ITS [29].

on the charge and the velocity ( $\beta$ ) of the particle, which, in turn, depends only on the momentum and the mass of the ionizing particle. Since momentum is already known from the track curvature and the charge is unitary for most measured tracks, measuring the  $dE/dx$  allows us to determine mass indirectly and thus determine the particle species. The following Bethe-Bloch parameterization gives the mean specific energy loss:

$$-\left\langle \frac{dE}{dx} \right\rangle = k_1 \cdot z^2 \frac{Z}{A} \cdot \frac{1}{\beta^2} \left[ \frac{1}{2} \ln(k_2 \cdot m_e c^2 \cdot \beta^2 \gamma^2) - \beta^2 + k_3 \right] \quad (2.1)$$

where  $\beta\gamma = p/Mc$  and

Z: atomic number of the ionized gas (in this case Ne/CO<sub>2</sub>/N<sub>2</sub>)

A: mass number of the ionized gas (g/mol)

$m_e$ : electron mass

z: electric charge of the ionizing particle in unit of electron charge  $e$

M: ionizing particle mass

$p$ : ionizing particle momentum

$\beta$ : ionizing particle velocity normalized to the light velocity  $c$

$\gamma = 1/\sqrt{1 - \beta^2}$ , Lorentz factor

$k_1, k_2, k_3$ : constants depending on the ionized medium

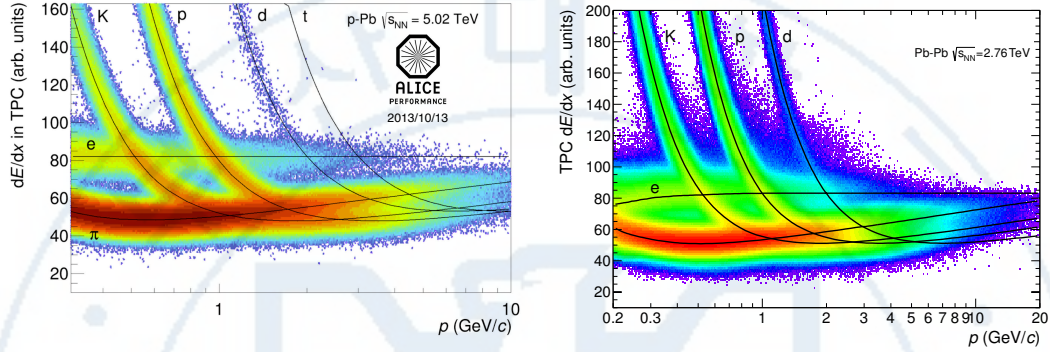


Figure 2.6: Specific energy loss ( $dE/dx$ ) in the TPC as a function of momentum in p-Pb collisions at  $\sqrt{s_{NN}} = 5.02$  TeV (top) and Pb-Pb collisions at  $\sqrt{s_{NN}} = 2.76$  TeV (bottom). The lines show the parameterizations of the expected mean energy loss.

The specific energy loss in the TPC as a function of momentum is shown in Figure 2.6. Left panel on Figure 2.6 shows  $dE/dx$  distribution as a function of momentum in p-Pb collisions at  $\sqrt{s_{NN}} = 5.02$  TeV and right panel presents distribution in Pb-Pb collisions at  $\sqrt{s_{NN}} = 2.76$  TeV. The different bands show expected values for  $e^\pm$ ,  $\pi^\pm$ ,  $K^\pm$ ,  $p^\pm$  and deuteron. These correspond to the statistical distribution of the measured energy loss.

The expected value which corresponds to the prediction by the Bethe-Bloch parameterization is shown as black lines on Figure 2.6. For a track within the TPC, the relevant quantity to be considered for PID is the difference between the specific energy loss measured by the detector and the corresponding value predicted by the Bethe-Bloch parametrization. The difference could be expressed in a number of  $\sigma$  as shown in Equation 2.2. In this way, it is possible to estimate the goodness of a mass hypothesis more quantitatively. It also provides the possibility to choose

strictness to be adopted for the identification by applying a different value of  $n_\sigma$ .

$$n_\sigma = \frac{(dE/dx)_{measured} - (dE/dx)_{Bethe-Bloch}}{\sigma_{TPC}} \quad (2.2)$$

### 2.1.2 Particle identification using weak decay topology

In addition to the direct identification of stable hadrons (e.g.,  $\pi$ , K, p) by using mass-dependent signals such as  $dE/dx$ , TOF, and Cherenkov radiation, ALICE also identifies hadrons through their weak decay topologies. This technique is used for strange hadrons, such as  $K_s^0$ ,  $\Lambda$ , and multi-strange baryons,  $\Xi$  and  $\Omega$  to remove combinatorial backgrounds which is particularly huge in Pb–Pb collisions.

Because they have long decay length (e.g.,  $c\tau$  of  $\Lambda \sim 7.89$  cm), tracks with a distance of closest approach to the interaction vertex exceeding a certain minimum value (0.5 mm in pp, p–Pb and 1 mm in Pb–Pb) are selected. For each unlike-sign pair of such tracks called V0 candidate, the Point of Closest Approach (PCA) between the two tracks is calculated, and it is requested to be less than 1.5 cm in pp, p–Pb and 1.0 cm in Pb–Pb collisions. The cosine of the angle between the total momentum vector of the pair,  $\vec{p}_{pair}$ , and the straight line connecting the primary (interaction) and secondary vertices must exceed 0.9 in pp, p–Pb and 0.998 in Pb–Pb collisions [28]. For V0 candidates with a momentum below 1.5 GeV/c, the latter cut is relaxed. It facilitates the subsequent search for cascade decays. The left and middle panel in Figure 2.7 shows  $K_s^0$  and  $\Lambda$  peak obtained in central Pb–Pb collisions.

After reconstructing V0 candidates, the search for the cascade ( $\Xi^-$ ) decays is performed. The V0 candidates with an invariant mass in the vicinity of the  $\Lambda$  are matched with a secondary track by applying a selection cut on their mutual distance and requesting that the latter is outside of a cylindrical volume around the interaction vertex ( $r > 0.2$  cm). As results, the signal of  $\Xi^-$  and its antiparticle is shown in the right panel in Figure 2.7 [30, 18].

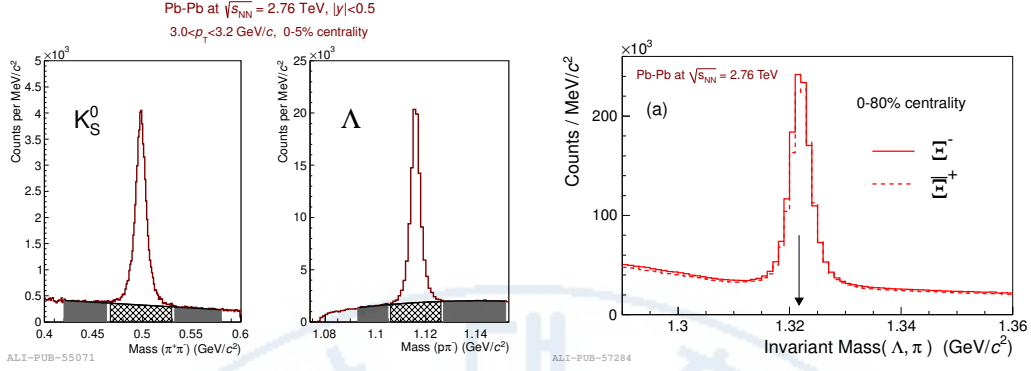


Figure 2.7: Invariant mass distribution of  $\pi^+\pi^-$  (left panel),  $p\pi^-$  (middle) and  $\Lambda\pi$  pairs (right panel) in Pb-Pb collisions at  $\sqrt{s_{NN}} = 2.76$  TeV [30, 18].

### 2.1.3 Definition of ALICE coordinate system

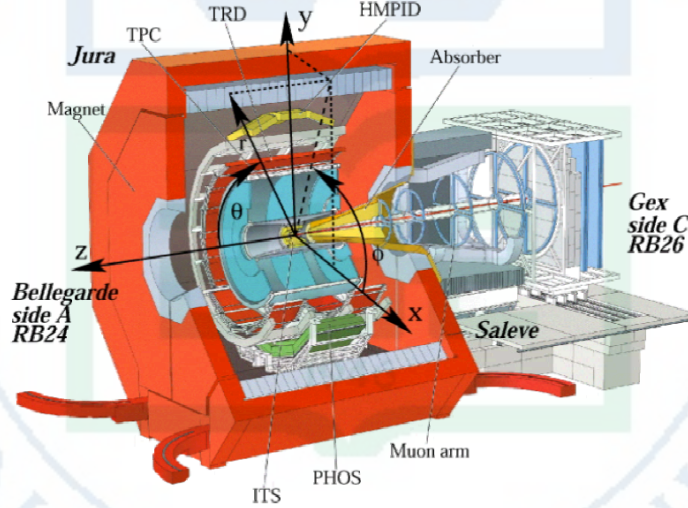


Figure 2.8: Definition of the ALICE coordinate system axis, angles and detector sides

The ALICE global coordinate system [31] is a right-handed orthogonal Cartesian system with the origin  $X, Y, Z = 0$  at the center of the detector. Figure 2.8 shows the definition of the ALICE coordinate system axis, angles and detector sides. The three Cartesian axes are defined as follows: the X-axis pointing towards the center of the LHC, the Y-axis pointing upward and the Z-axis parallel to beamline pointing in the direction opposite to the muon spectrometer. The



azimuthal angle increases counter-clockwise from the positive X-axis ( $\Phi = 0$ ) to the positive Y-axis ( $\Phi = \pi/2$ ) when the observer stands at positive Z and looking at negative Z. The polar angle increases from the positive Z-axis ( $\theta = 0$ ) to the X-Y plane ( $\theta = \pi/2$ ) and the negative Z-axis ( $\theta = \pi$ ).

## 2.2 Determination of centrality definition

One of the important parameters which have to be determined in heavy-ion collisions is the centrality. The centrality is defined according to the value of the impact parameter  $b$  which is the length of a 2D vector, connecting the center of the two nuclei and provides a geometrical scale of the overlapping region. Figure 2.9 shows the feature of the impact parameter. As the impact parameter increases, the collision will be defined from central to peripheral. The centrality of a collision is not directly measurable and must be deduced from a combination of experimentally measured quantities and Monte Carlo simulations.

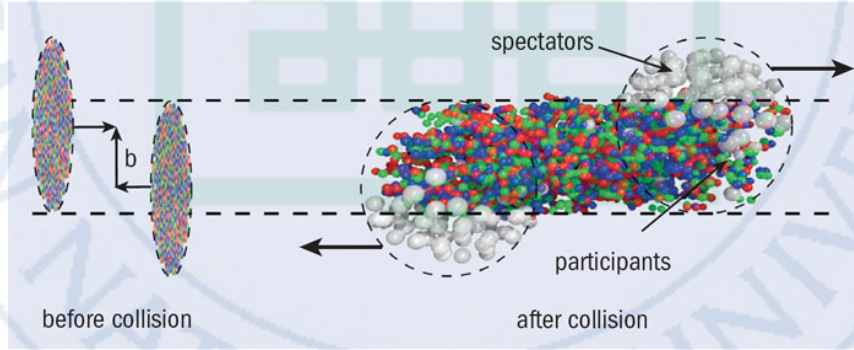


Figure 2.9: Two heavy-ions before collision with impact parameter  $b$  and then, the spectator nucleons continue unscattered, while in the participant zone particle production takes place [32].

The centrality estimation used in this thesis is based on the measurement of signals from the VZERO scintillators. In order to categorize the events in p-Pb collisions, the information accumulated in V0A( $2.8 < \eta < 5.1$ ) is used while V0M which is the sum of the amplitude in the VZERO A and C( $-3.7 < \eta < -1.7$ ) is used



to classify centrality in Pb–Pb collisions [33, 34]. The distributions of the V0A and V0M amplitudes are shown in Figure 2.10, and the vertical lines separate the centrality classes. A Glauber model is used to relate the V0A(V0M) amplitude distribution to the geometry of the collisions.

Estimator	Centrality(%)	$\langle dN_{\text{ch}}/d\eta_{\text{lab}} \rangle$
V0A (p–Pb)	0-20	$35.6 \pm 0.8$
	20-40	$23.2 \pm 0.5$
	40-60	$16.1 \pm 0.4$
	60-100	$7.1 \pm 0.2$
V0M (Pb–Pb)	0-10	$1448 \pm 55$
	10-40	$680 \pm 25$
	40-80	$130 \pm 5$

Table 2.1: Mean charged-particle multiplicity densities ( $\langle dN_{\text{ch}}/d\eta_{\text{lab}} \rangle$ ) measured at mid-rapidity ( $|\eta_{\text{lab}}| < 0.5$ ) [35], corresponding to the centrality classes defined using the V0A (V0M) detector [33, 34] in p–Pb (Pb–Pb) collisions at  $\sqrt{s_{\text{NN}}} = 5.02$  (2.76) TeV.

The centrality classes in p–Pb and Pb–Pb used in this analysis is written in Table 2.1 with corresponding mean charged-particle multiplicity densities ( $\langle dN_{\text{ch}}/d\eta_{\text{lab}} \rangle$ ) measured at mid-rapidity ( $|\eta_{\text{lab}}| < 0.5$ ) [33, 34, 35].

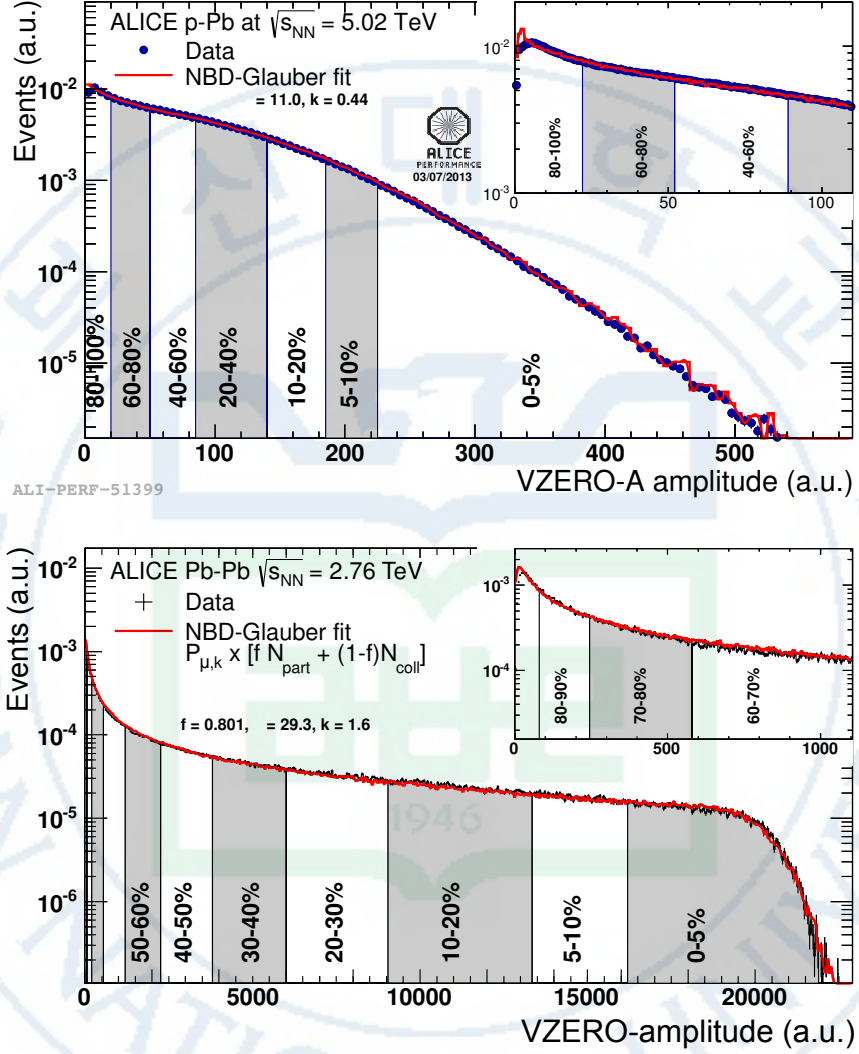


Figure 2.10: Distribution of the sum of amplitudes in the V0A (top) (Pb-going) for p-Pb collisions and V0M (bottom) for Pb-Pb collisions. Centrality classes are indicated by vertical lines. The insets show zoom-in distributions on the most peripheral events. [33, 34]

## Chapter 3

# Measurements of $\Xi(1530)^0$ in p–Pb and Pb–Pb collisions

In order to study the particle production mechanisms in the hadronic phase between the chemical and kinetic freeze-out, the  $\Xi(1530)^0$  resonance at mid-rapidity ( $-0.5 < y_{\text{CMS}} < 0$ ) was measured in p–Pb collisions at  $\sqrt{s_{\text{NN}}} = 5.02$  TeV and in Pb–Pb collisions with  $|y| < 0.5$  at  $\sqrt{s_{\text{NN}}} = 2.76$  TeV with the ALICE by the reconstruction of its hadronic decay into  $\Xi\pi$ . In this chapter, detailed steps for the  $\Xi(1530)^0$  reconstruction are provided in section 3.1, and then the efficiency correction obtained from Monte Carlo (MC) is explained in section 3.2. In section 3.3, the corrected  $p_{\text{T}}$ -spectra are presented, and systematic studies are discussed in the last section.

### 3.1 $\Xi(1530)^0$ -reconstruction

The  $\Xi(1530)^0$  productions in p–Pb and Pb–Pb collisions at mid-rapidity were measured in different multiplicity and centrality classes, from peripheral to central collisions as well as for minimum bias triggered events. The analysis is based on the invariant mass of the daughter pairs which might be the decay of a  $\Xi(1530)^0$  baryon into charged hadrons. Invariant mass is defined as below (Note that, we use units such that  $c = 1$ ):

$$M^2(\Xi^{*0}) = (E_{\Xi} + E_{\pi})^2 - (\vec{p}_{\Xi} + \vec{p}_{\pi})^2 \quad (3.1)$$

As a starting point of analysis, data sample used in this analysis is shortly in-

roduced, and event selection is explained. In order to select tracks that have good quality and satisfy topological criteria for  $\Xi(1530)^0$  reconstruction via its daughter particles, track and topological selections are applied and will be explained. By using weak decay topology technique which was described in Section 2.1.2, the daughter particles are identified as oppositely charged  $\Xi$  and  $\pi$  among the tracks reconstructed in the central barrel. In addition, PID technique is used to reduce background contamination. As a result of aforementioned steps, invariant mass distributions of  $\Xi\pi$  in p-Pb and Pb-Pb collisions are obtained. Then, the raw yield is extracted by integrating the fit on the background-subtracted invariant mass distributions in several transverse momentum intervals.

### 3.1.1 Data sample and event selection

A description of the ALICE experimental setup and its performance during the LHC Run 1 (2010–2013) can be found in [26, 28]. The data sample in the analysis from Pb-Pb collisions at  $\sqrt{s_{\text{NN}}} = 2.76$  TeV was obtained during 2011, and the sample of p-Pb collisions at  $\sqrt{s_{\text{NN}}} = 5.02$  TeV was recorded in 2013.

Due to the asymmetric energies of the proton (4 TeV) and lead ion (1.57 A TeV) beams of p-Pb collision system, the center-of-mass system in the nucleon-nucleon frame is shifted in rapidity by  $\Delta y_{\text{NN}} = 0.465$  towards the direction of the proton beam with respect to the laboratory frame of the ALICE detector [23]. In case of p-Pb collisions, the direction of the proton beam was towards the ALICE muon spectrometer, the denominated “C” side, located at negative rapidities; conversely, the Pb beam circulated towards positive rapidities, labeled as “A” side. Note that, Pb-p collision system has opposite direction of p and Pb beams.

The analysis in this paper was carried out at mid-rapidity, in the rapidity window in laboratory system  $-0.465 < y_{\text{LAB}} < 0.035$ . Corresponding rapidity interval is  $-0.5 < y_{\text{CMS}} < 0$  following ALICE convention which defines that proton

going direction is defined as positive rapidity, while in p-Pb collisions system case, proton beam was configured to have negative direction. Therefore one needs a sign conversion.

The minimum bias trigger during the p-Pb run was configured to collect events by requiring a logical OR of signals in V0A and V0C [26]. During analysis, a coincidence of signals in both V0A and V0C was required to remove the events from single-diffractive and electromagnetic interactions. This lead to the collection of about 109.3 million events. Among them, 93.9 million events pass the following selection criteria and have been used for the analysis.

The data sample in Pb-Pb collisions was selected by online centrality trigger which requires a signal above a specific threshold in the forward V0 detectors [34] to record preferentially central collisions. The data consists of 24.8 million events in most central collisions (0-10%), 21.8 million events in semi-central collisions (10-50%) and 3.5 million events with the minimum-bias trigger (0-90%). Among them, 43.0 million events have been analyzed as passed the criteria below.

- Events with z-position of primary vertex ( $V_z$ ) within  $\pm 10$  cm of the center of TPC/ITS
- Rejection of pile-up event
- Requiring primary tracks to have at least one hit in SPD
- p-Pb: multiplicity ranges in percentile (V0A): 0-20%, 20-40%, 40-60%, 60-100% and MB(0-100%)
- Pb-Pb: centrallity classes (V0A and V0C): 0-10%, 10-40%, 40-80% and MB (0-80%)

The distribution of  $V_z$  for the accepted events in p-Pb collisions is reported in the upper panel of Figure 3.1 and same figure but obtained from Pb-Pb collisions is shown in the bottom panel on Figure. 3.1. Events with  $|V_z| < 10$  cm have been



used to make sure that the tracks have been obtained from uniform acceptance in the central pseudo-rapidity region,  $|\eta| < 0.8$ , where the analysis is performed. This cut reduces the total number of events. It results in the selection of,  $\sim 89.2\%$  events in p-Pb collisions and  $\sim 86.8\%$  events in Pb-Pb collisions.

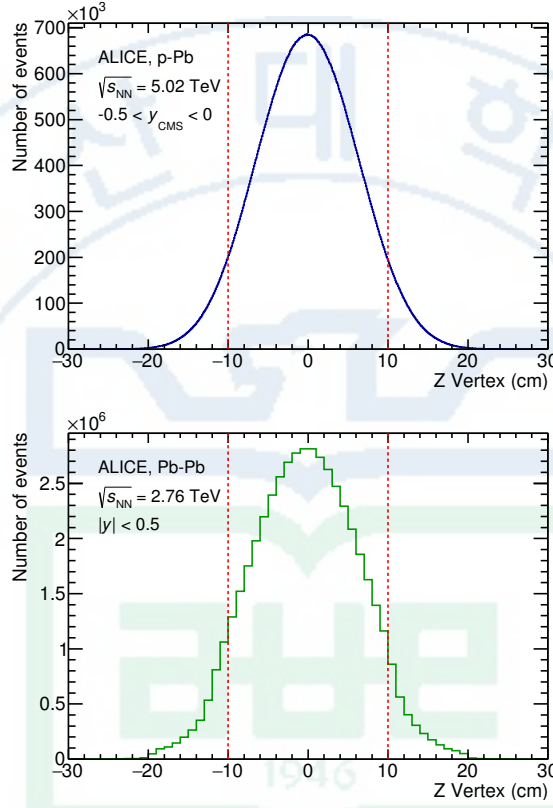


Figure 3.1: Distribution of vertex-z position from the accepted events in p-Pb collision (top) and in Pb-Pb collisions (bottom). The red dashed line indicates vertex cut on  $|V_z| < 10$  cm

figure 3.2 shows the multiplicity distribution of the accepted events in p-Pb collision divided into bins of percentile. Each color on the histogram indicates a multiplicity interval used in this analysis. The corresponding number of events of each multiplicity range is provided in Table 3.1.

The centrality distribution from each trigger (kCentral, kSemiCentral, kMB) in Pb-Pb collisions is shown in Figure 3.3. The centrality has step structure because three different trigger classes were requested with different threshold for

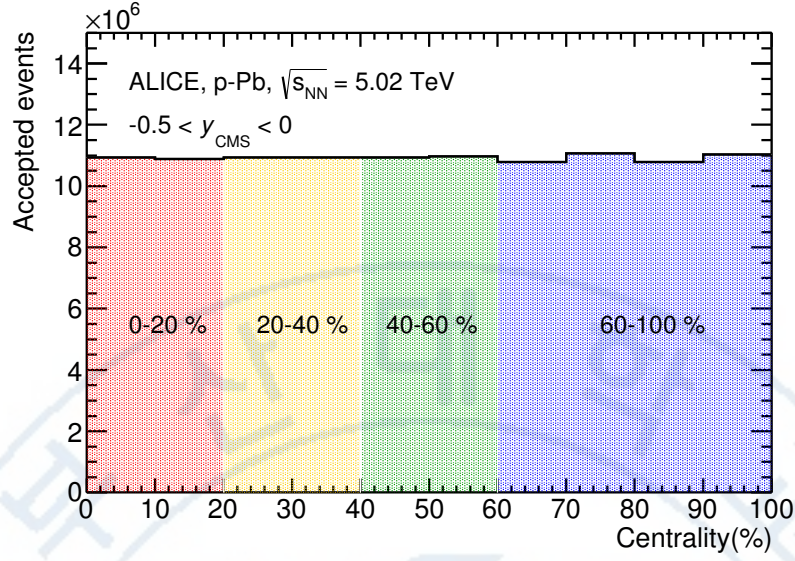


Figure 3.2: Multiplicity distribution of accepted events in p-Pb collision in percentile. The each color presents the four intervals for the analysis.

signal on VZERO detector in order to obtain specific data sample in Pb-Pb collisions. Because the number of events with centrality is not a flat, this may lead to additional bias, in particular when one needs to combine the results from different triggers. For example, events from the 0-20% centrality bin should be biased to have results which could be obtained from central events due to the high statistics recorded for the 0-10% centrality interval. In order to compensate this effect, we have applied a flattening procedure to have the same number of events in each centrality bin. A brief explanation of the method is provided below :

1. Invariant mass distribution is obtained in 1% centrality bins
2. Scale factor for each 1% centrality bin is computed with:

$$\text{Scale factor} = N_{\text{event in 20-40\%}} / 20 / N_{\text{event in current 1\% bin}}$$

, where 20 is number of centrality bin in 20-40%

3. Each invariant mass distribution from 1% centrality bin is scaled using the computed factor

4. Histograms are added for the different centrality bins of interest: 0-10%, 10-40%, 40-80%, 0-80%

The resulting number of events in each centrality classes is summarized in Table 3.1.

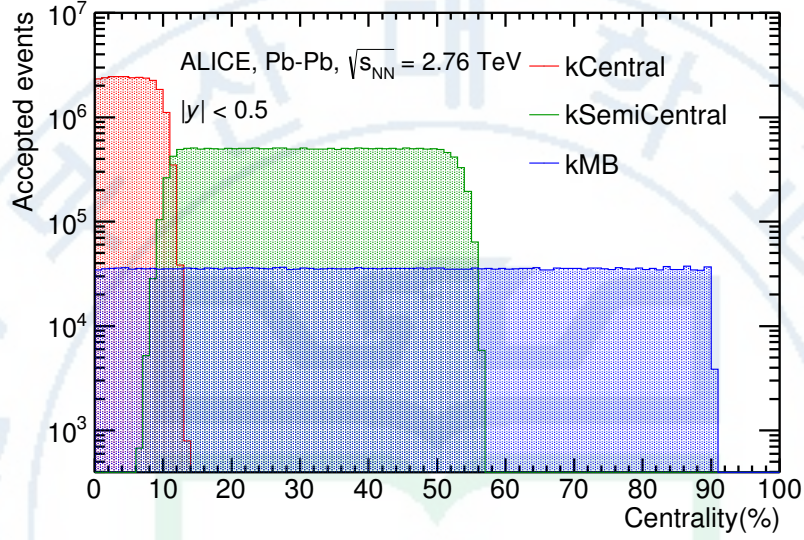


Figure 3.3: Centrality distribution for the three different trigger bins.

Collision	Centrality	Number of events
p-Pb	0-20%	$21.82 \times 10^6$
	20-40%	$21.86 \times 10^6$
	40-60%	$21.91 \times 10^6$
	60-100%	$43.68 \times 10^6$
Pb-Pb	0-10%	$5.58 \times 10^6$
	10-40%	$16.73 \times 10^6$
	40-80%	$22.31 \times 10^6$

Table 3.1: Number of analyzed events per multiplicity/centrality interval

### 3.1.2 Track and topological selection criteria

The track and topological selections are summarized in Table 3.2. All charged tracks were selected with  $p_T > 0.15$  GeV/ $c$ . For the selection of pseudo-rapidity,  $|\eta_{\text{lab}}| < 0.8$  cut is implemented since the ALICE detector is optimized for measuring charged particles in the central pseudo-rapidity region [26]. The Particle IDentification (PID) criteria for all decay daughters are based on the requirement that the specific energy loss ( $dE/dx$ ) is measured in the TPC within three standard deviations ( $\sigma_{\text{TPC}}$ ) from the expected value ( $dE/dx_{\text{exp}}$ ), computed using a Bethe-Bloch parametrization [26]. The primary tracks were chosen with the Distance of Closest Approach (DCA) to Primary Vertex (PV) of less than 2 cm along the longitudinal direction ( $\text{DCA}_z$ ) and lower than  $7\sigma_r$  in the transverse plane ( $\text{DCA}_r$ ), where  $\sigma_r$  is the resolution of  $\text{DCA}_r$ .

The quality of the charged track reconstruction in the TPC is related to the number of clusters a track is composed of. In order to reduce contamination from fake tracks, but not be too sensitive to run-by-run changes in the TPC condition, a reasonably loose cut was selected. As such, the cut was requiring at least 70 clusters deposited in the TPC, out of the possible 160 pad rows. In addition, during reconstruction procedure, a value of  $\chi^2$  is calculated for each TPC cluster that reflects the quality of the track. Therefore,  $\chi^2 < 4$  selection was applied to select primary tracks. To ensure good quality of primary tracks, candidate tracks were required to have at least one hit in one of the two innermost layers of the Inner Tracking System (ITS).

Because pions and protons from the weak decay of  $\Lambda$  ( $c\tau = 7.89$  cm [16]) and pions from the weak decay of  $\Xi^-$  ( $c\tau = 4.91$  cm [16]) are produced away from the PV, specific topological, and track selection criteria are applied as summarized in Table 3.3. The DCA of proton and  $\pi$  track from the  $\Lambda$  decay to the primary vertex is requested to be larger than 0.06 cm for p-Pb data sample and 0.11 cm for Pb-Pb data sample. The  $\text{DCA}_r$  of  $\pi$  from  $\Xi$  to the primary vertex is applied



Common track selections	$ \eta_{\text{lab}} $	$< 0.8$
	$p_{\text{T}}$	$> 0.15 \text{ GeV}/c$
	PID $ (dE/dx) - (dE/dx)_{\text{exp}} $	$< 3 \sigma_{\text{TPC}}$
Primary track selections	$\text{DCA}_z$ to PV	$< 2 \text{ cm}$
	$\text{DCA}_r$ to PV	$< 7\sigma_r - 10\sigma_r (p_{\text{T}})$
	number of SPD points	$\geq 1$
	number of TPC points	$> 70$
	$\chi^2$ per cluster	$< 4$

Table 3.2: Track selections common to all decay daughters and primary track selections applied to the charged pions from decays of  $\Xi^{*0}$ .

to be larger than 0.015 cm in p-Pb, 0.035 cm in Pb-Pb respectively. The DCA between the daughter tracks (e.g.,  $\pi p$  from  $\Lambda$  and  $\pi\Lambda$  from  $\Xi$ ) is also used to select V0 candidates. For p-Pb collisions, the DCA between decay daughters of  $\Lambda$  ( $\Xi$ ) is required to be less than 1.4 cm (1.9 cm). The same cut with value of 0.95 cm (0.275 cm) is applied for Pb-Pb collisions.

The pointing angle is defined as the angle between the reconstructed position and momentum vectors of a V0s (e.g.,  $\Lambda$ ,  $\Xi$ ) as shown in Figure 3.4. If the value of Cosine Pointing Angle (CPA) equals unity, the V0 points directly back to the primary vertex, while a lower value would indicate that the V0 is possibly a secondary particle or even combinatorial background. The  $\text{CPA}(\theta_{\Lambda})$  is required to be larger than 0.875 for p-Pb and 0.998 for Pb-Pb collisions. For  $\text{CPA}(\theta_{\Xi})$ , the cut is applied to be larger than 0.981 for p-Pb and 0.9992 for Pb-Pb collisions. The radius of the fiducial volume ( $r(\Lambda)$ ,  $r(\Xi)$ ) is also applied.

As daughter particle of  $\Xi(1530)^0$ , the  $\Xi$  is obtained from the invariant mass distribution of  $M_{\Lambda\pi}$  selecting the  $\Xi$  candidate when it is inside an interval of  $\pm 7 \text{ MeV}/c^2$  from the mass of  $\Xi$  given by PDG.



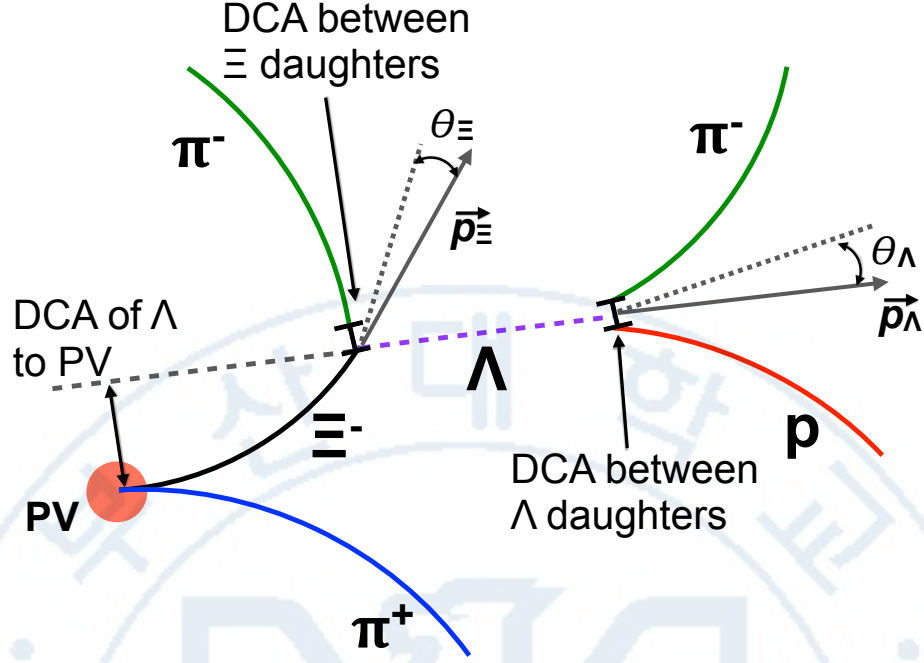


Figure 3.4: Sketch of the decay modes for  $\Xi^{*0}$  and depiction of the track and topological selection criteria.

Topological cuts	p-Pb	Pb-Pb
$DCA_r$ of $\Lambda$ decay products to PV	$> 0.06$ cm	$> 0.11$ cm
DCA between $\Lambda$ decay products	$< 1.4$ cm	$< 0.95$ cm
DCA of $\Lambda$ to PV	$> 0.015$ cm	$> 0.06$
$\cos\theta_\Lambda$	$> 0.875$	$> 0.998$
$r(\Lambda)$	$0.2 < r(\Lambda) < 100$ cm	$0.2 < r(\Lambda) < 100$ cm
$ M_{p\pi} - m_\Lambda $	$< 7$ MeV/ $c^2$	$< 7$ MeV/ $c^2$
$DCA_r$ of pion (from $\Xi^-$ ) to PV	$> 0.015$ cm	$> 0.035$ cm
DCA between $\Xi^-$ decay products	$< 1.9$ cm	$< 0.275$
$\cos\theta_\Xi$	$> 0.981$	$> 0.9992$
$r(\Xi^-)$	$0.2 < r(\Xi^-) < 100$ cm	$0.2 < r(\Xi^-) < 100$ cm
$ M_{\Lambda\pi} - m_\Xi $	$< 7$ MeV/ $c^2$	$< 7$ MeV/ $c^2$

Table 3.3: Topological and track selection criteria.

### 3.1.3 Particle identification

PID selection criteria are applied for

1.  $\pi^\mp$  (last emitted  $\pi$ ) and proton from  $\Lambda$
2.  $\pi^\mp$  (second emitted  $\pi$ ) from  $\Xi^\mp$

to

from the information of  $dE/dx$  as

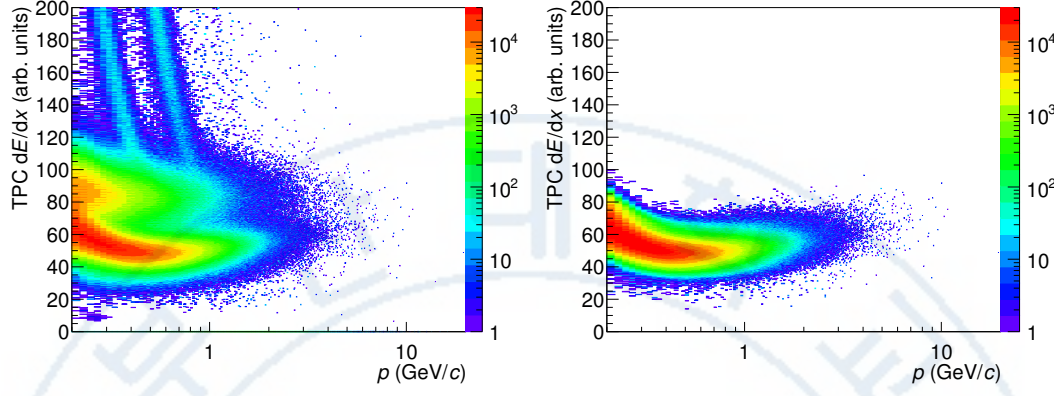


Figure 3.7: TPC  $dE/dx$  as function of momentum in p-Pb collisions for total (Left) and selected last emitted  $\pi$  in  $3\sigma$ (Right)

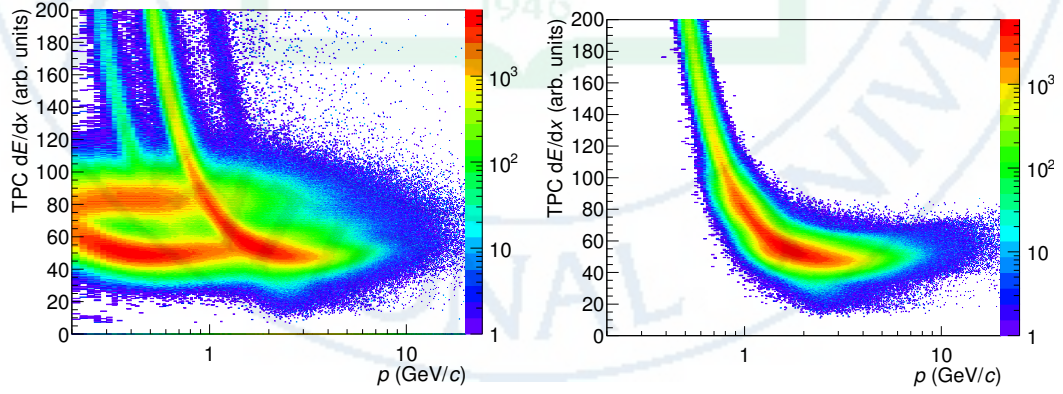


Figure 3.8: TPC  $dE/dx$  as function of momentum in p-Pb collisions for total (Left) and selected proton in  $3\sigma$ (Right)

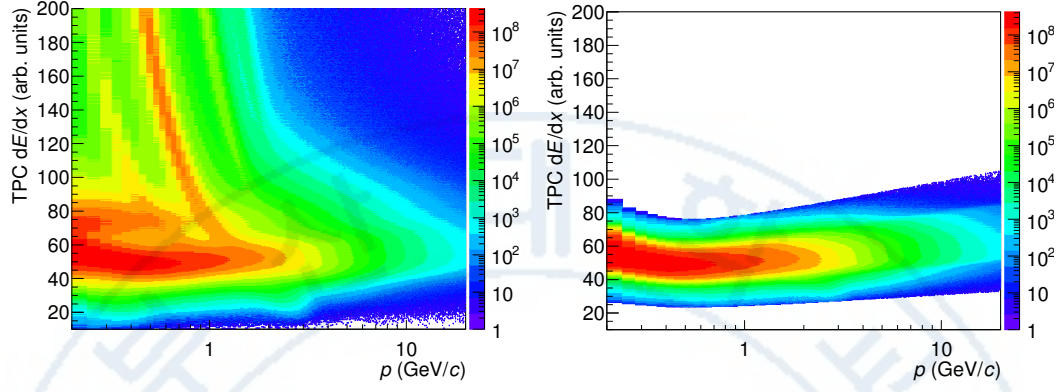


Figure 3.9: TPC  $dE/dx$  as function of momentum in Pb–Pb collisions for total (Left) and selected first emitted  $\pi$  in  $3\sigma$  (Right)

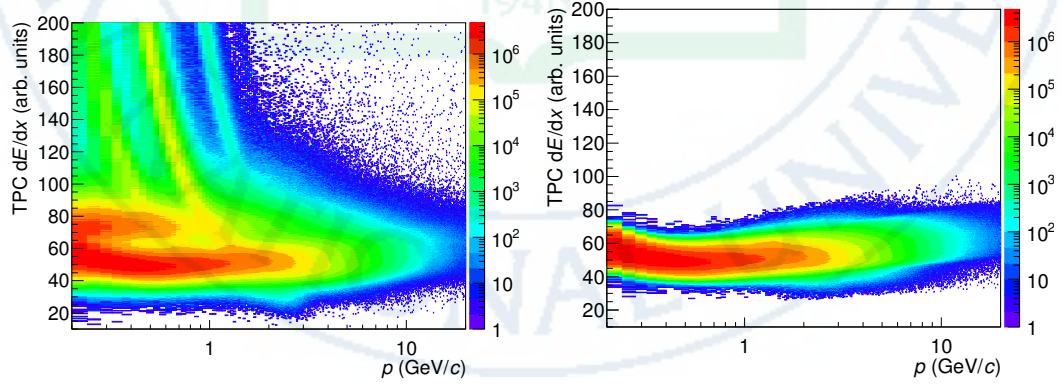


Figure 3.10: TPC  $dE/dx$  as function of momentum in Pb–Pb collisions for total (Left) and selected second emitted  $\pi$  in  $3\sigma$  (Right)



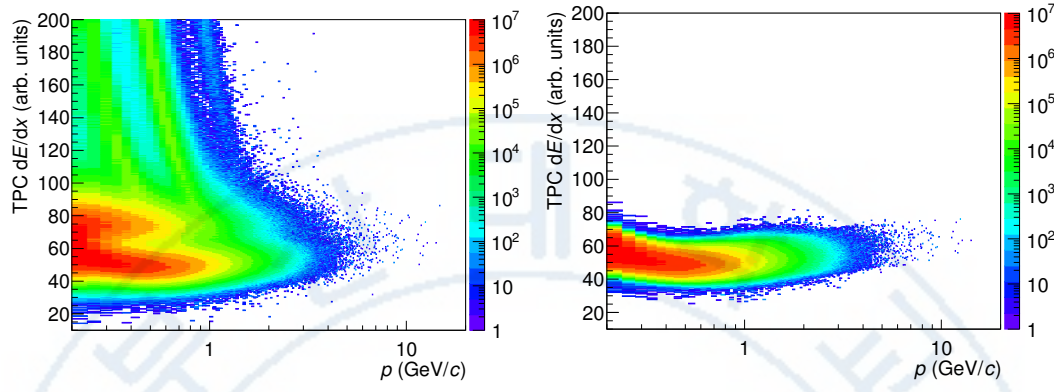


Figure 3.11: TPC  $dE/dx$  as function of momentum in Pb–Pb collisions for total (Left) and selected last emitted  $\pi$  in  $3\sigma$  (Right)

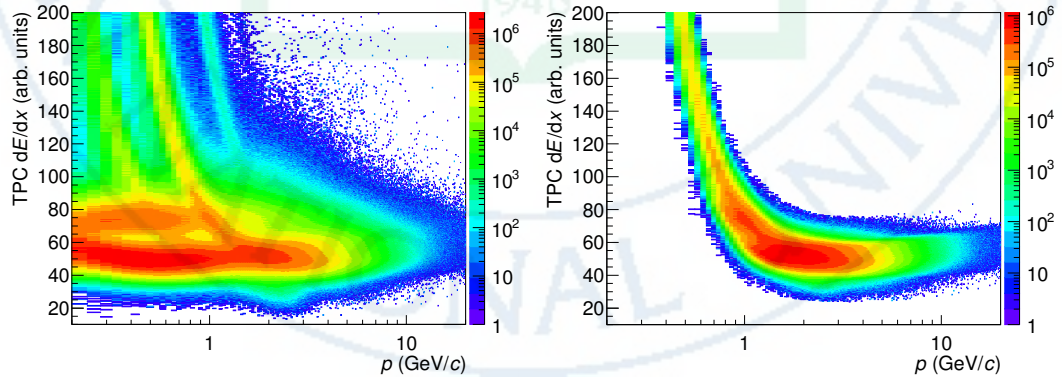


Figure 3.12: TPC  $dE/dx$  as function of momentum in Pb–Pb collisions for total (Left) and selected proton in  $3\sigma$  (Right)

### 3.1.4 Signal extraction

The  $\Xi(1530)^0$  signal was reconstructed by invariant-mass analysis from the candidates of the decay products in each  $p_T$  intervals and different multiplicity/centrality classes. The  $\Xi^-\pi^+(\Xi^+\pi^-)$  invariant mass distribution from semi-central events (20-40%) in p-Pb collisions and the distribution from central events (0-10%) in Pb-Pb collisions are shown in Figure 3.13.

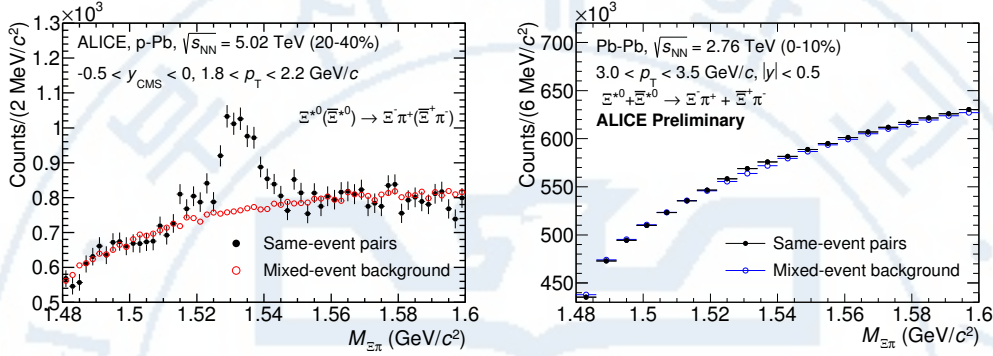


Figure 3.13:  $\Xi^\mp\pi^\pm$  invariant mass distribution (Same-event pairs) in  $1.8 < p_T < 2.2$  GeV/c for the multiplicity class of 20-40% in p-Pb collisions (left) and in  $3.0 < p_T < 3.5$  GeV/c for the centrality class of 0-10% in Pb-Pb collisions (right). The signals are presented as black dots and the mixed-event backgrounds are shown as red dots for p-Pb collisions and blue dots for Pb-Pb collisions.

Since the decay products of resonances come from the location that is indistinguishable from the PV, a significant combinatorial background is present. In order to extract  $\Xi(1530)^0$  signal, it is necessary to reduce the combinatorial background as much as possible. To get background distributions, event mixing technique has been applied by combining uncorrelated decay products from 20 different events in p-Pb collisions (5 different events in Pb-Pb collisions). The events for the mixing have been chosen by applying the similar selection to minimize distortions due to different acceptances and to ensure a similar event structure. Tracks from events with similar vertex positions  $z$  ( $|\Delta z| < 1$  cm) and track multiplicities  $n$  ( $|\Delta n| < 10$ ) were taken.

The distribution of mixed-event background was normalized to counts in re-

gions,  $1.49 < M_{\Xi\pi} < 1.51 \text{ GeV}/c^2$  and  $1.56 < M_{\Xi\pi} < 1.58 \text{ GeV}/c^2$ , around the  $\Xi(1530)^0$  mass peak. The uncertainty on the selection of the range for normalization was estimated by varying the normalization regions and is included into the systematic uncertainty as part of signal extraction (Section 3.4).

The  $\Xi(1530)^0$  particle with p-Pb data sample has been analyzed in 10  $p_T$  bins starting from 0.8 to 8  $\text{GeV}/c$  ( $p_T$  bin: 0.8–1.4–1.8–2.2–2.6–3.0–3.4–3.8–4.8–5.8–8.0  $\text{GeV}/c$ ). The invariant mass distributions and distributions of mixed-event background in each  $p_T$  bins for different multiplicity classes are shown with Figures 3.14 to 3.18.

The analysis of  $\Xi(1530)^0$  in Pb-Pb collisions have been performed in 7  $p_T$  bins starting from 1.2 to 6  $\text{GeV}/c$  ( $p_T$  bin: 1.2–2.0–2.5–3.0–3.5–4.0–5.0–6.0  $\text{GeV}/c$ ). The invariant mass distributions as well as the distributions of mixed-event background in each  $p_T$  bins for different centrality intervals are shown with Figures 3.19 to 3.22.

As shown in Figure 3.14 to 3.18, the  $\Xi(1530)^0$  signal in p-Pb collisions is clearly seen in all  $p_T$  bins from 0.8 to 8  $\text{GeV}/c$ . It, therefore, can be extracted even without further background subtraction. On the other hand, the signal from Pb-Pb collision is very hard to extract as shown in Figure 3.19. Even though the invariant mass distribution is obtained from minimum-bias events which have larger statistics, there are only hints of signals, and it can not be extracted without background subtraction. The shape of the peak is hard to separate from the background. Moving to the semi-central events, 10-40% centrality, a peak is seen from  $\sim 2.5$ –3.0 or 3.0–3.5  $p_T$  bins as shown in Figure 3.21. Only for the signal from peripheral collisions in Pb-Pb, which resembles the event classes of central p-Pb collision, is distinguishable by the different shape of signal and background.

Background subtraction is necessary for the signal extraction and the distribution after the background subtraction is shown in Figure 3.23 as an example. The subtracted invariant mass distributions in all  $p_T$  bins in different multiplicity/centrality classes are shown in Figure 3.24 to 3.28 for p-Pb collisions and in

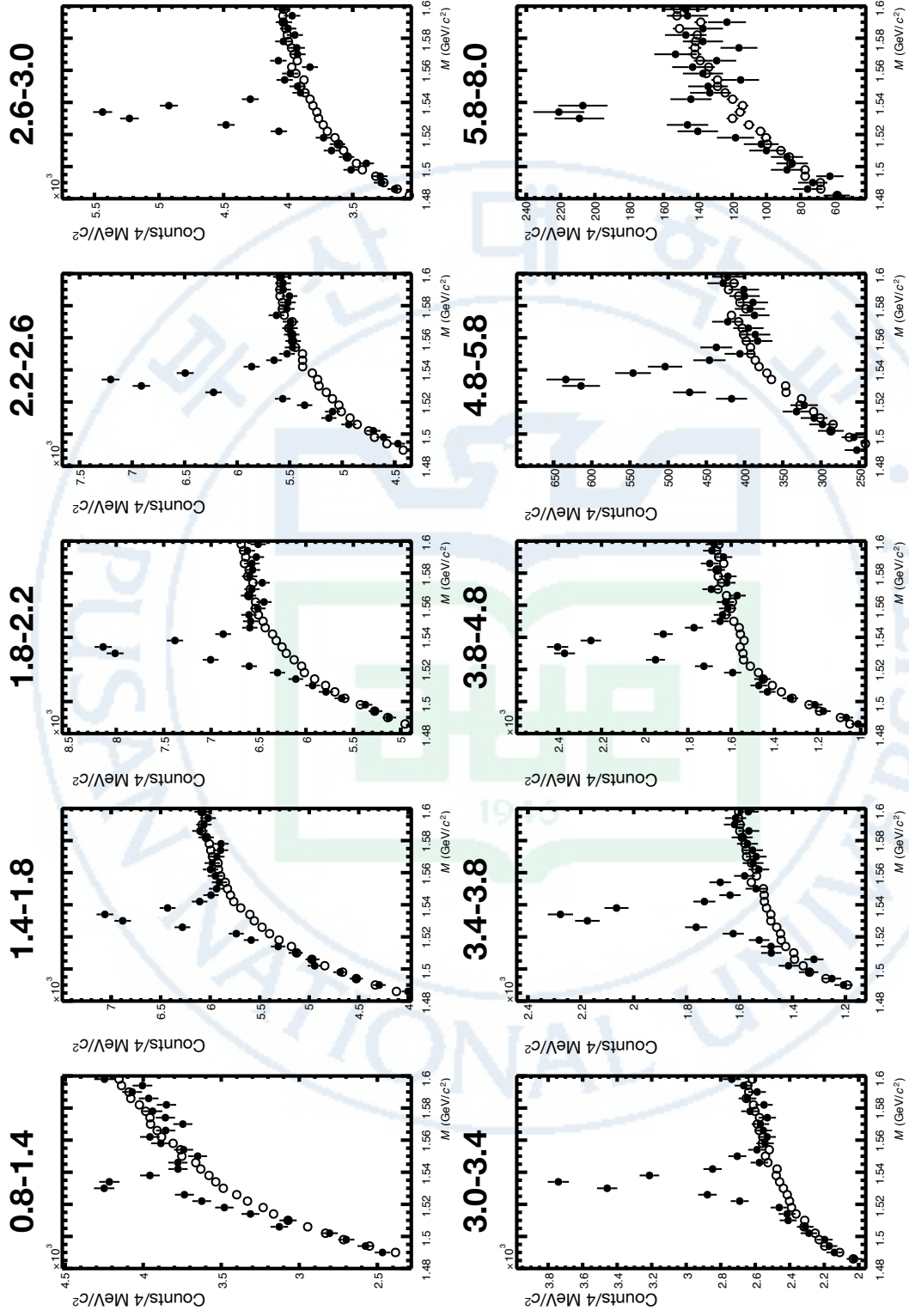


Figure 3.14:  $\Xi^\mp \pi^\pm$  invariant mass distributions (full circle) and the mixed-event background distributions (open circle) for 10  $p_T$  bins from minimum-bias events (0-100%) in p-Pb collisions. The values written above each figure indicate bin boundary of  $p_T$  bin.



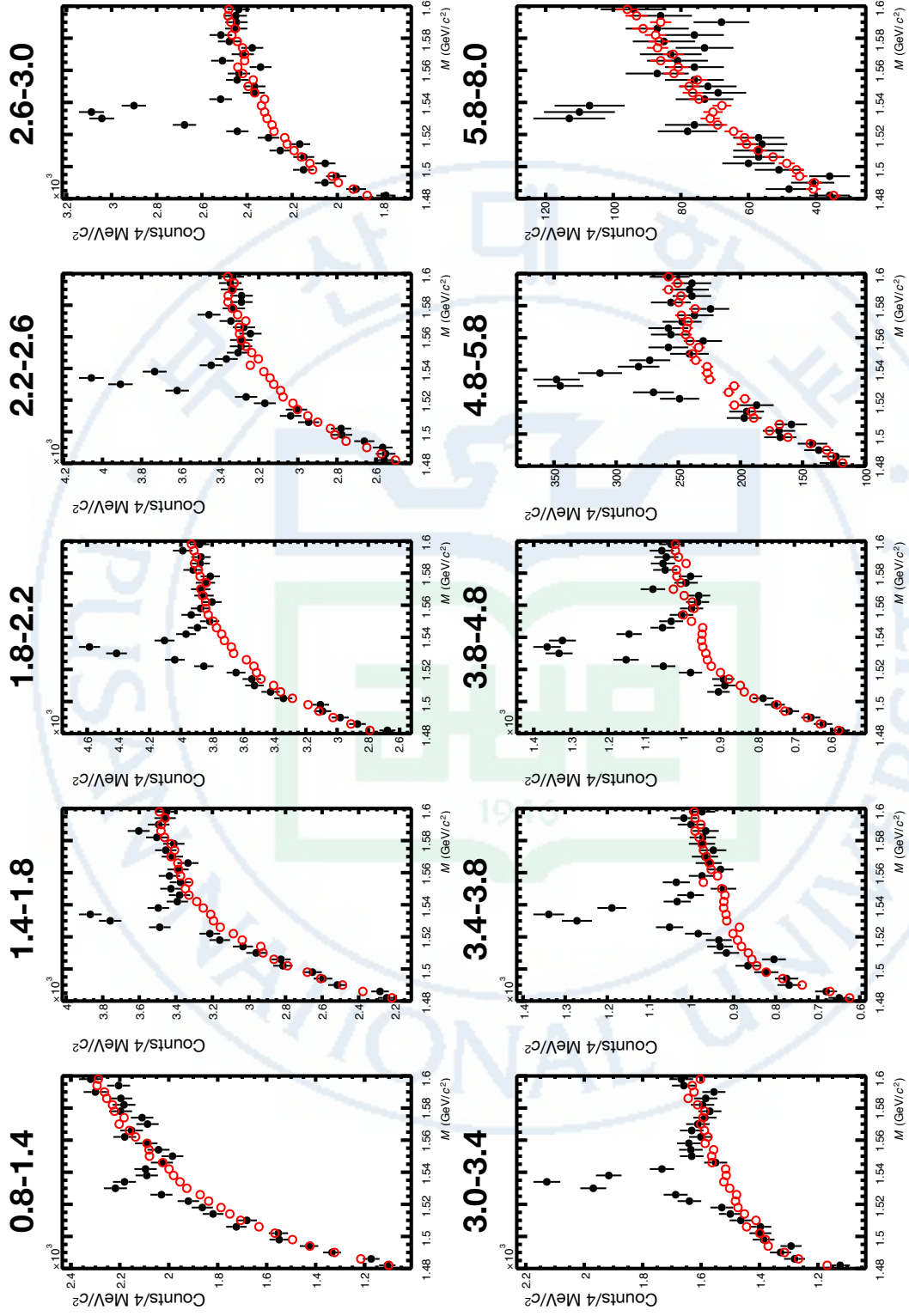


Figure 3.15:  $\Xi^\mp \pi^\pm$  invariant mass distributions (full circle) and the mixed-event background distributions (open circle) for 10  $p_T$  bins from central events (0-20%) in p-Pb collisions. The values written above each figure indicate bin boundary of  $p_T$  bin.

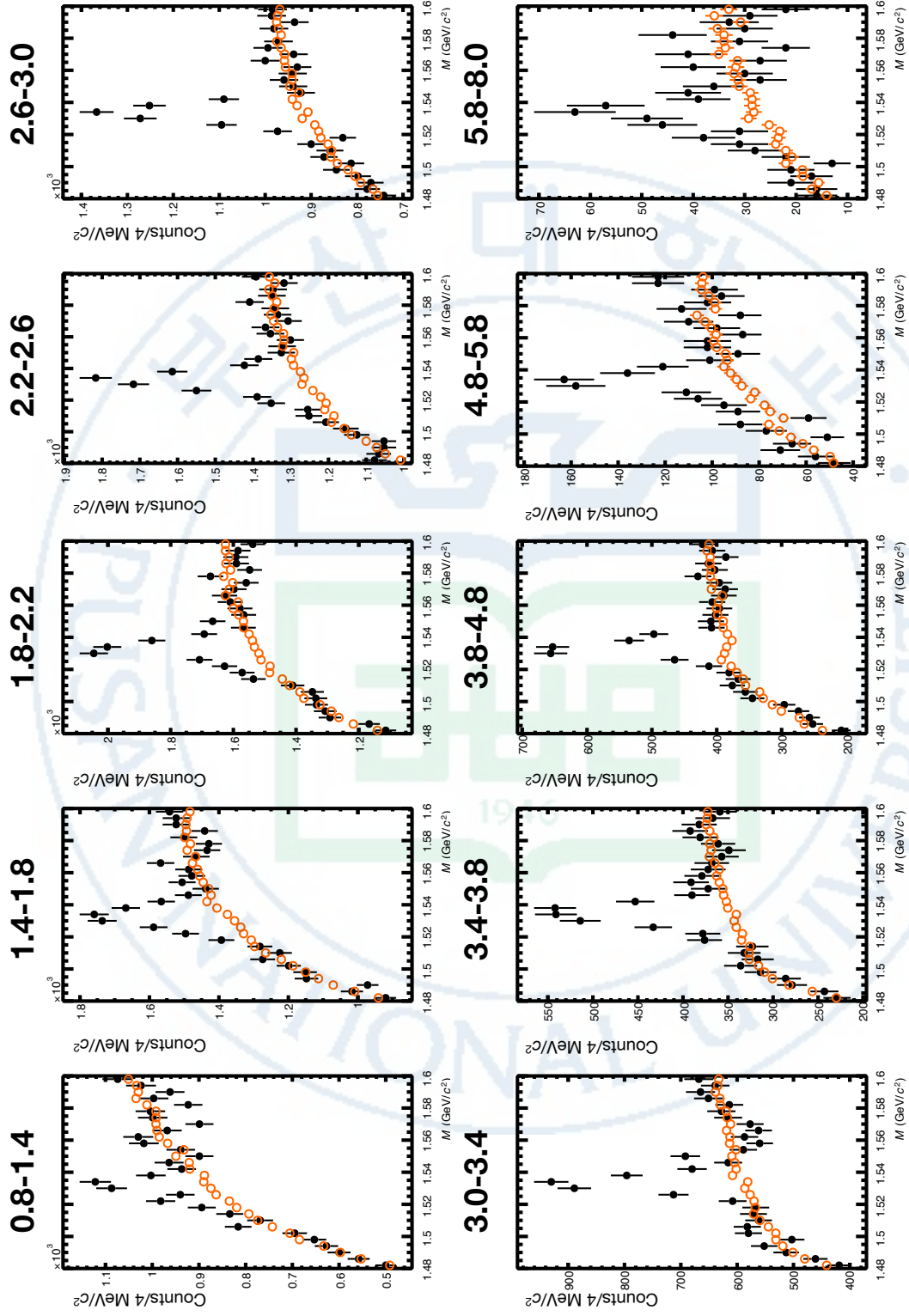


Figure 3.16:  $\Xi^\mp \pi^\pm$  invariant mass distributions (full circle) and the mixed-event background distributions (open circle) for 10  $p_T$  bins from 20-40% centrality interval in p-Pb collisions. The values written above each figure indicate bin boundary of  $p_T$  bin.

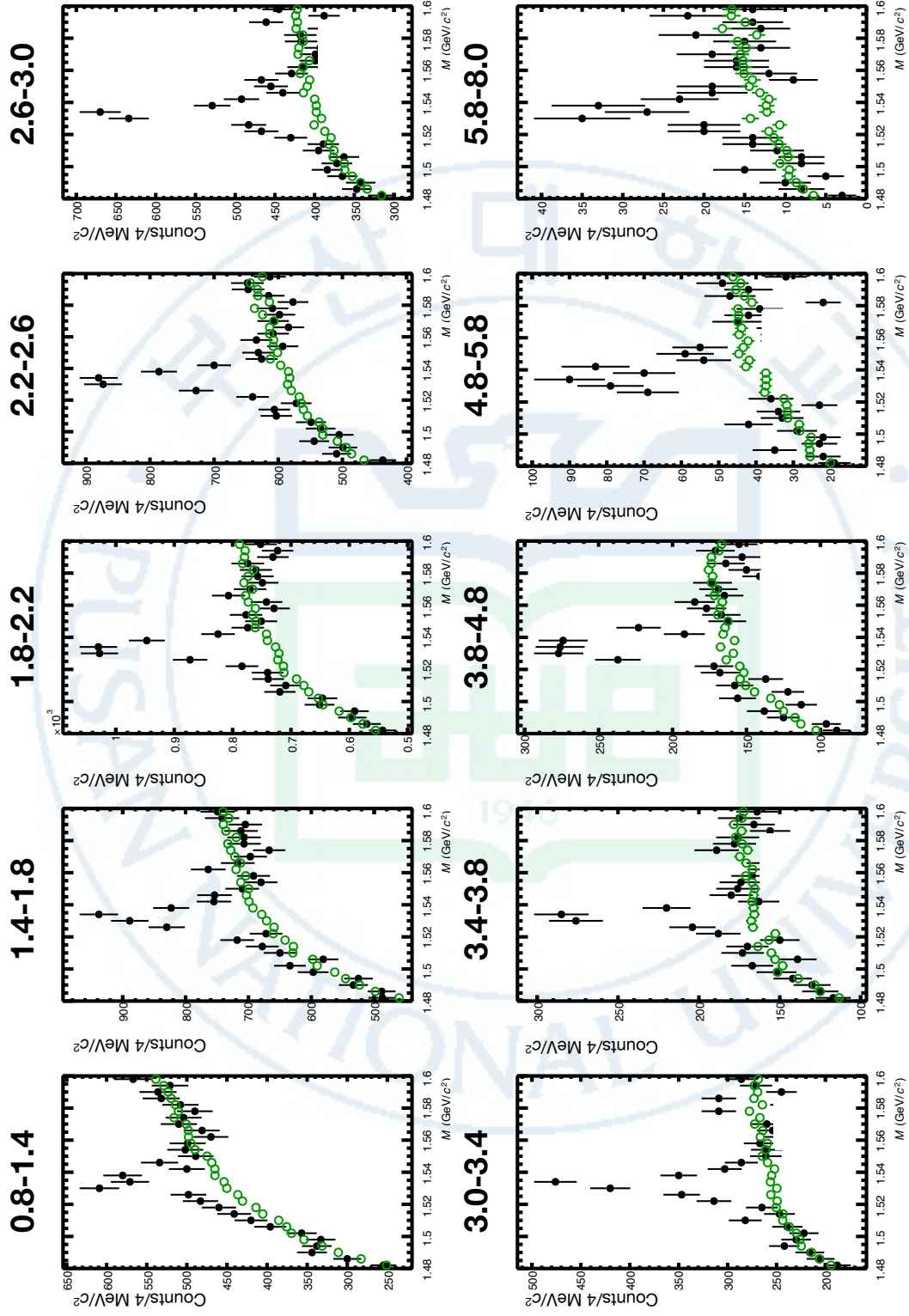


Figure 3.17:  $\Xi^\mp \pi^\pm$  invariant mass distributions (full circle) and the mixed-event background distributions (open circle) for 10  $p_T$  bins from 40-60% centrality interval in p-Pb collisions. The values written above each figure indicate bin boundary of  $p_T$  bin.

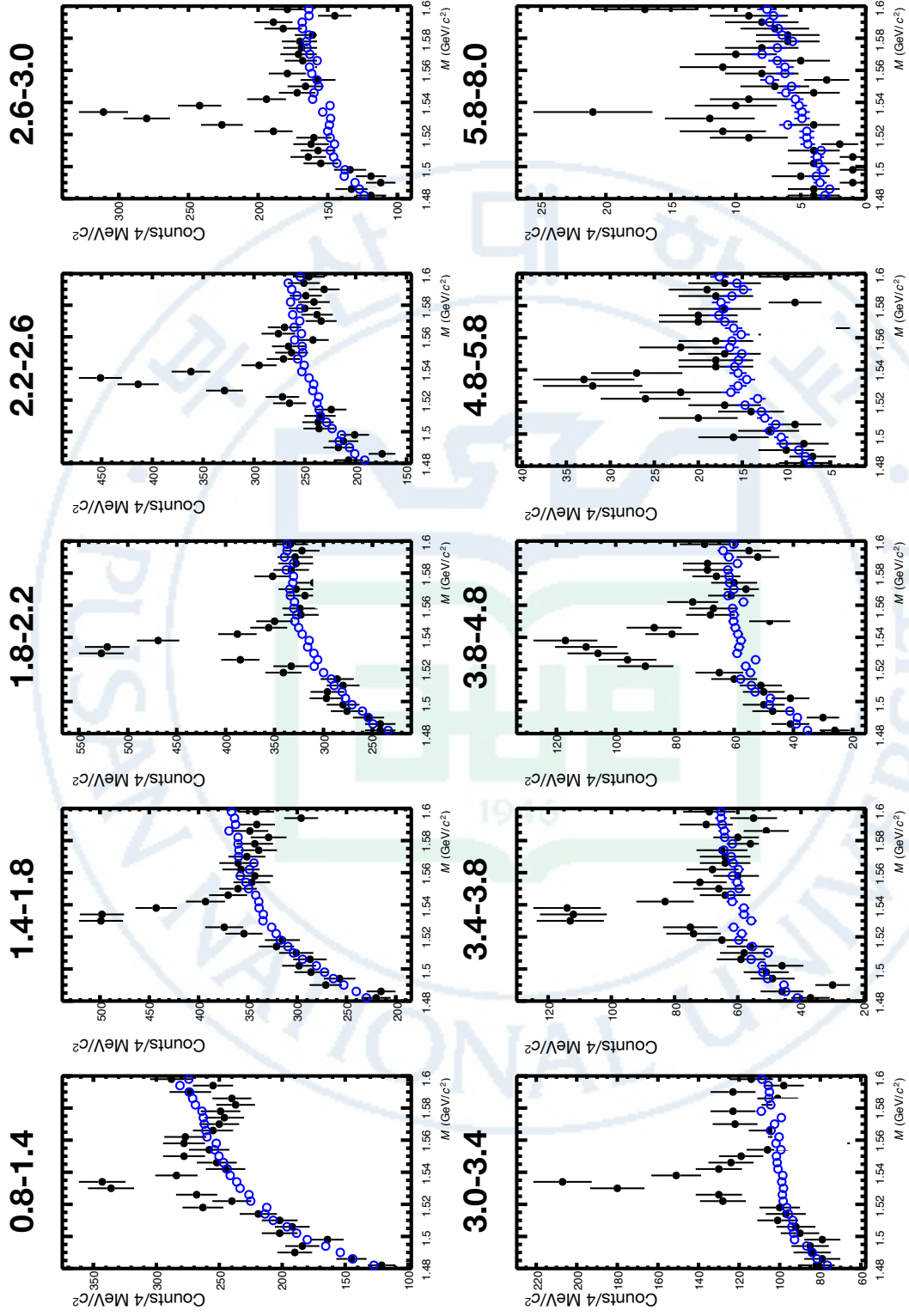


Figure 3.18:  $\Xi^\mp \pi^\pm$  invariant mass distributions (full circle) and the mixed-event background distributions (open circle) for 10  $p_T$  bins from peripheral events (60-100%) in p-Pb collisions. The values written above each figure indicate bin boundary of  $p_T$  bin.



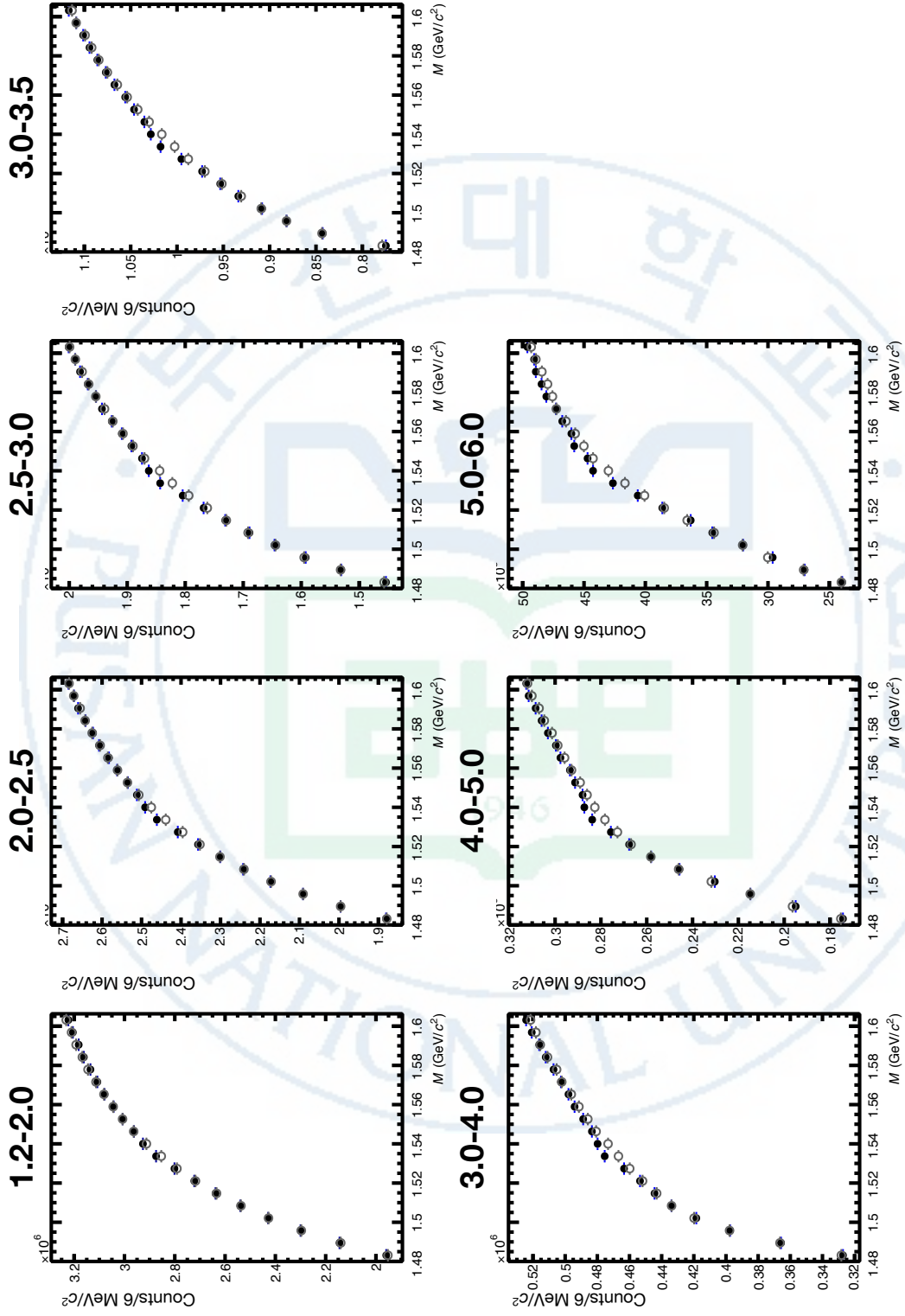


Figure 3.19:  $\Xi^\pm \pi^\pm$  invariant mass distributions (full circle) and the mixed-event background distributions (open circle) for 7  $p_T$  bins from minimum-bias events in Pb-Pb collisions. The values written above each figure indicate bin boundary of  $p_T$  bin.

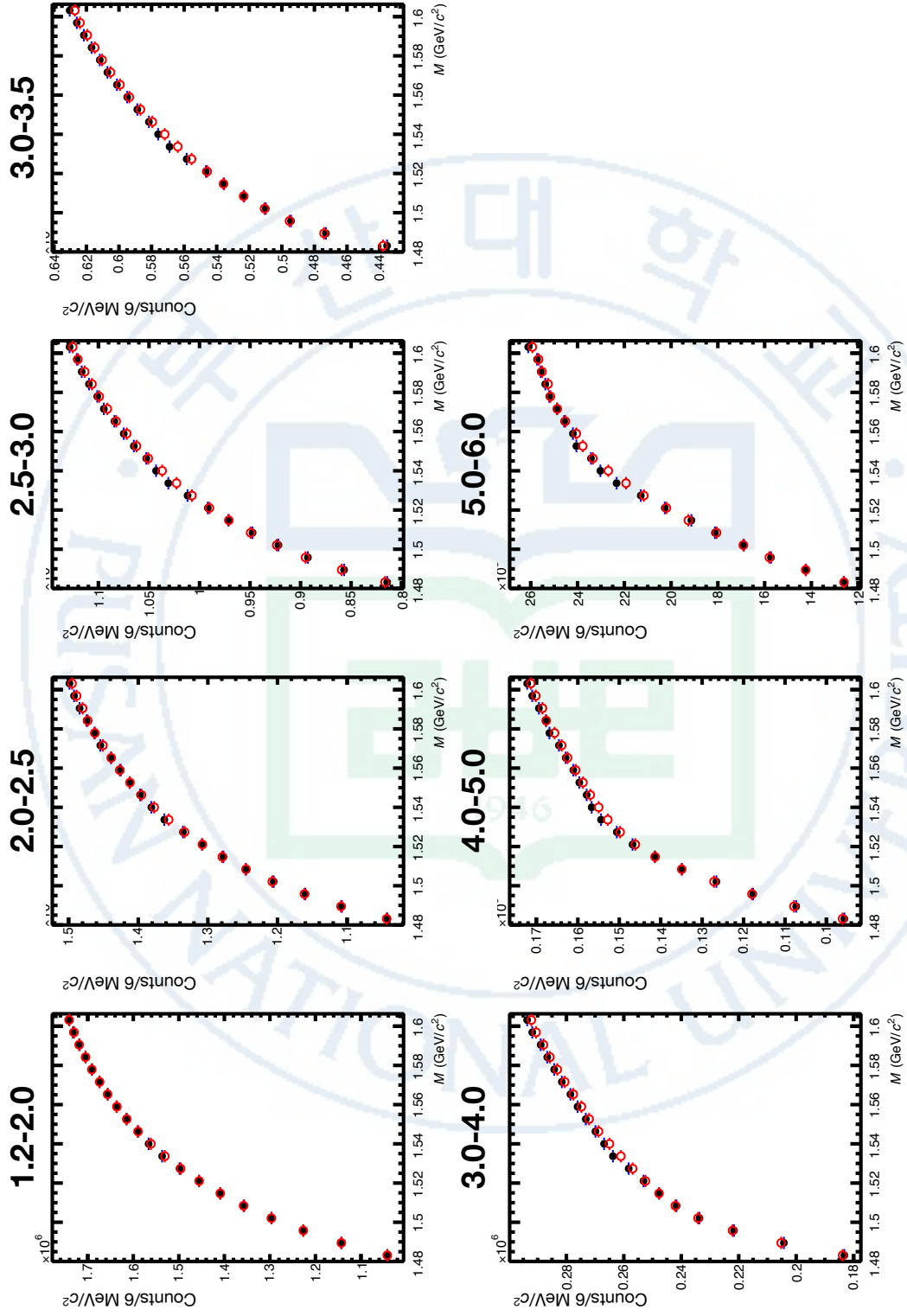


Figure 3.20:  $\Xi^\pm \pi^\pm$  invariant mass distributions (full circle) and the mixed-event background distributions (open circle) for 7  $p_T$  bins from central events (0-10%). The values written above each figure indicate bin boundary of  $p_T$  bin.

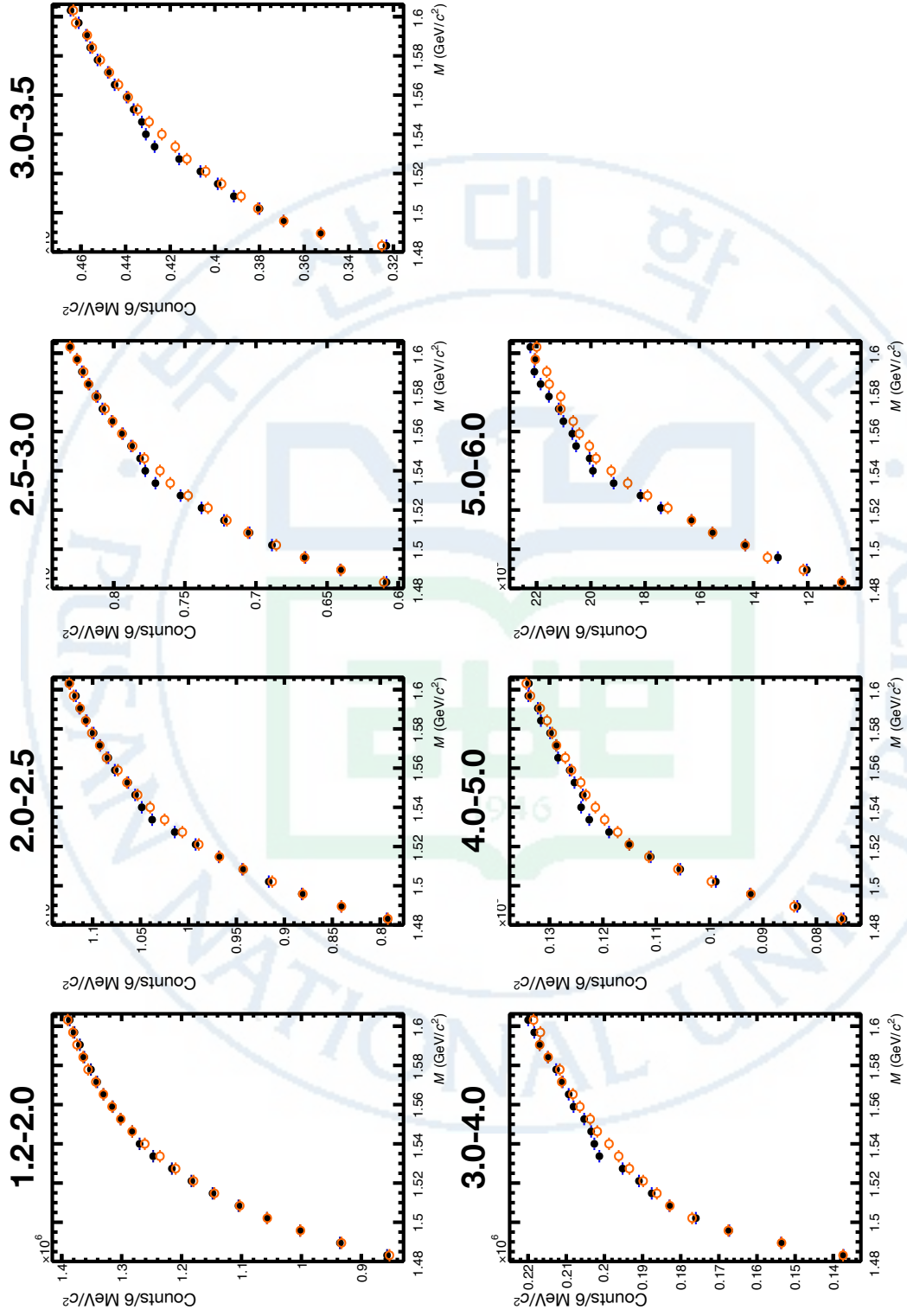


Figure 3.21:  $\Xi^\pm \pi^\pm$  invariant mass distributions (full circle) and the mixed-event background distributions (open circle) for 7  $p_T$  bins from semi-central events (10-40%). The values written above each figure indicate bin boundary of  $p_T$  bin.

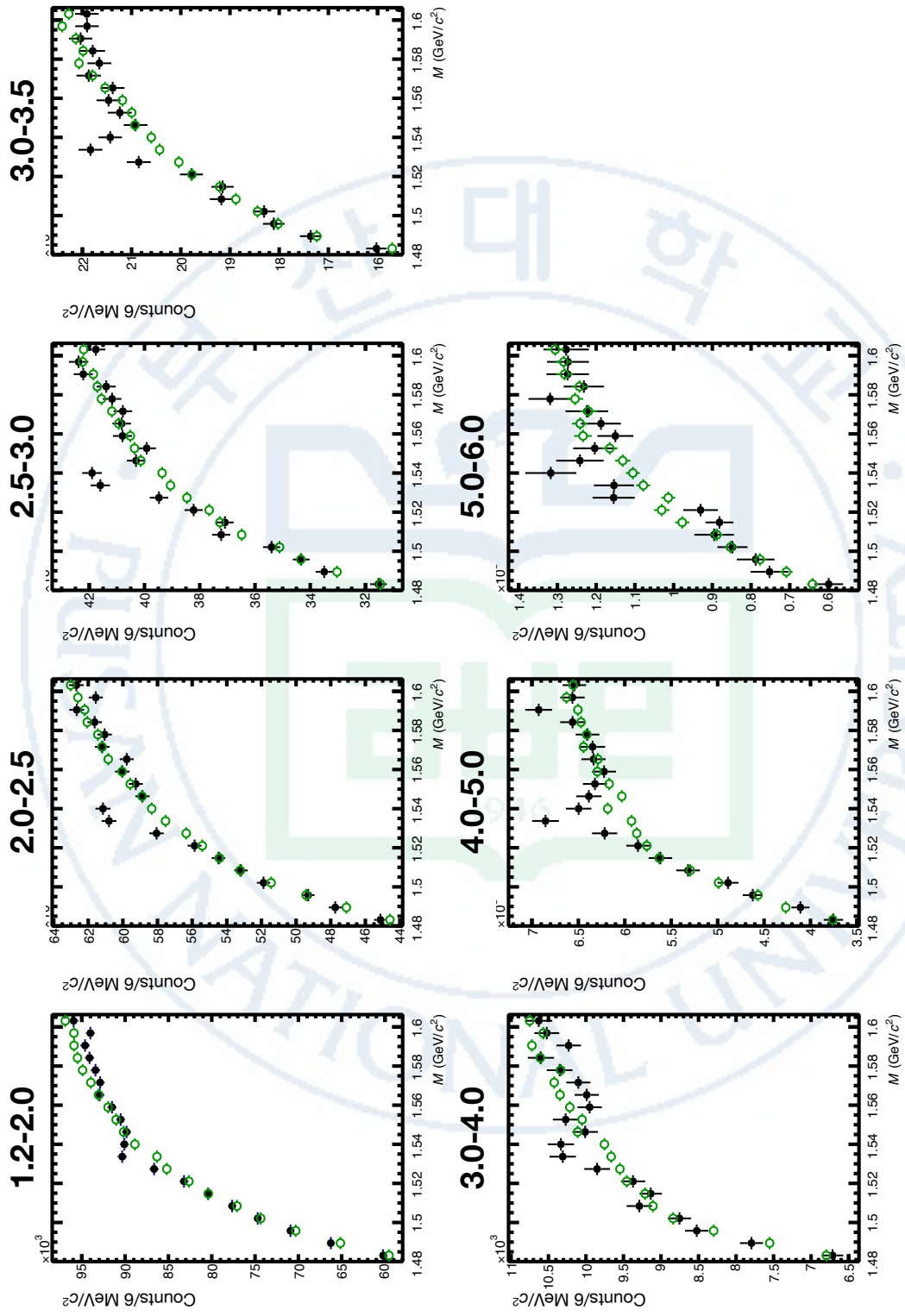


Figure 3.22:  $\Xi^\pm \pi^\pm$  invariant mass distributions (full circle) and the mixed-event background distributions (open circle) for 7  $p_T$  bins from peripheral events (40-80%) The values written above each figure indicate bin boundary of  $p_T$  bin.



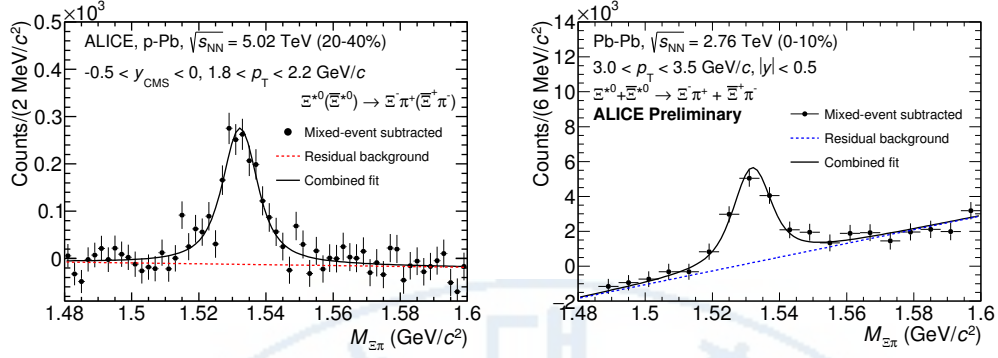


Figure 3.23: Invariant mass distribution after subtraction of the mixed-event background in p-Pb collisions (left) and in Pb-Pb collisions (right). The solid curve represents the combined fit, while the dashed line describes the residual background.

Figure 3.29 to 3.32 for Pb-Pb collisions.

In order to obtain raw yields, a combined fit of a first-order polynomial for the residual background and a Voigtian function for the signal were used. The Voigtian function is a convolution of a Breit-Wigner and a Gaussian function accounting for the detector resolution. The mathematical form of the fit function used in the analysis is:

$$f(M_{\Xi\pi}) = \frac{Y}{2\pi} \frac{\Gamma_0}{(M_{\Xi\pi} - M_0)^2 + \frac{\Gamma_0^2}{4}} \frac{e^{-(M_{\Xi\pi} - M_0)/2\sigma^2}}{\sigma\sqrt{2\pi}} + bg(M_{\Xi\pi}) \quad (3.2)$$

In fitting procedure, the mass parameter of the Voigtian fit ( $M_0$ ) is left free within the fit range (1.48 GeV/ $c^2$  and 1.59 GeV/ $c^2$ ). The width of the invariant mass distribution is governed by two parameters ( $\sigma$  and  $\Gamma_0$ ) when the Voigtian fit is applied. The  $\sigma$  describes broadening of the peak due to finite detector resolution while  $\Gamma_0$  comes from the intrinsic width of the resonance itself. The  $\Gamma_0$  is fixed to the PDG value of 9.1 MeV/ $c$  for the  $\Xi(1530)^0$ . The  $\sigma$  can be overestimated due to lack of statistics. Therefore the  $\sigma$  parameter is fixed to a value derived from  $\sigma$  in MB events which has the largest statistics. The  $\sigma$  as a function of  $p_T$  distribution for MB events is shown in Figure. 3.33 and we also report the mass of

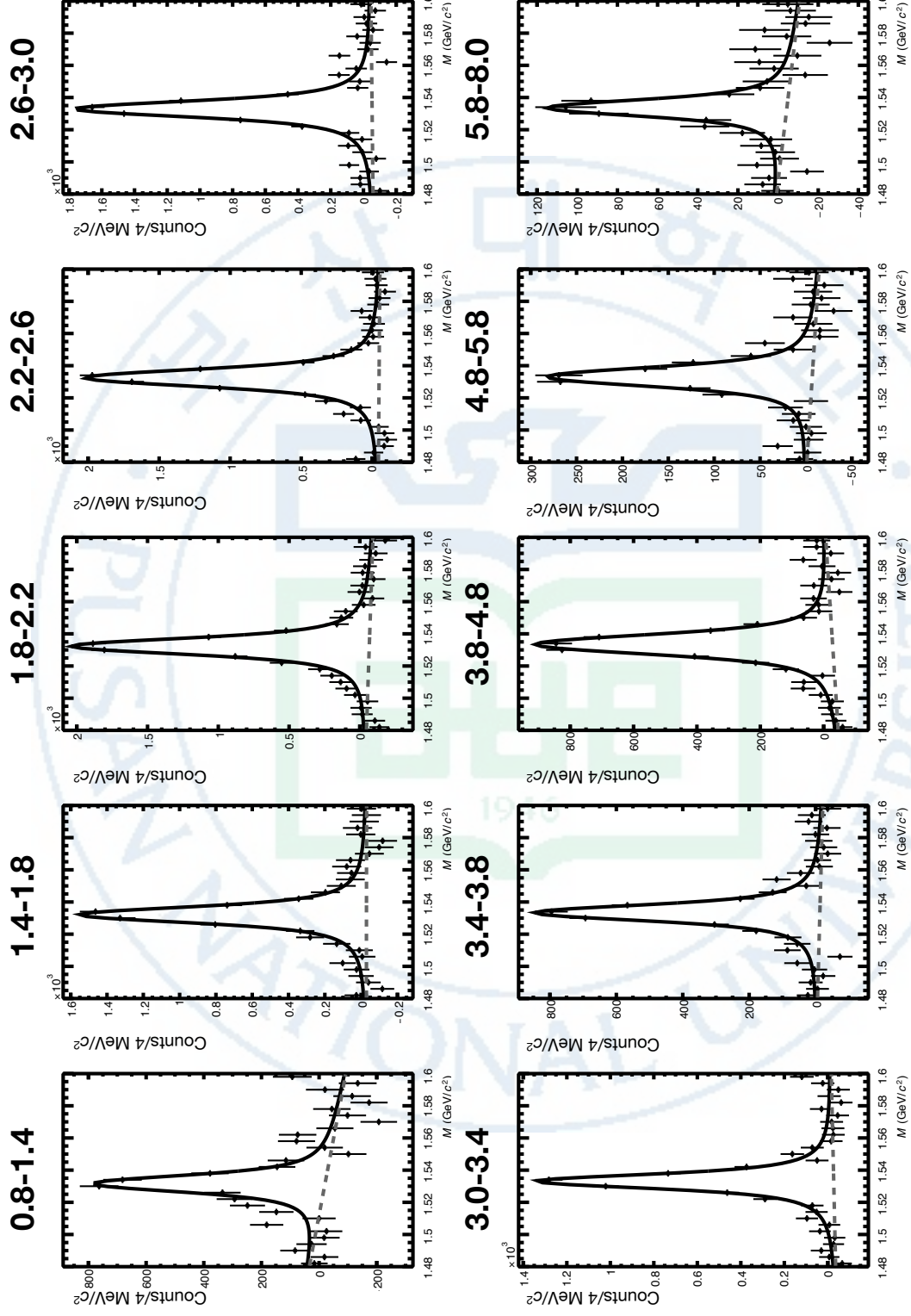


Figure 3.24: Invariant mass distributions after subtraction of the mixed-event background in minimum-bias event in p-Pb collisions. The solid curve represents the combined fit, while the dashed line describes the residual background.

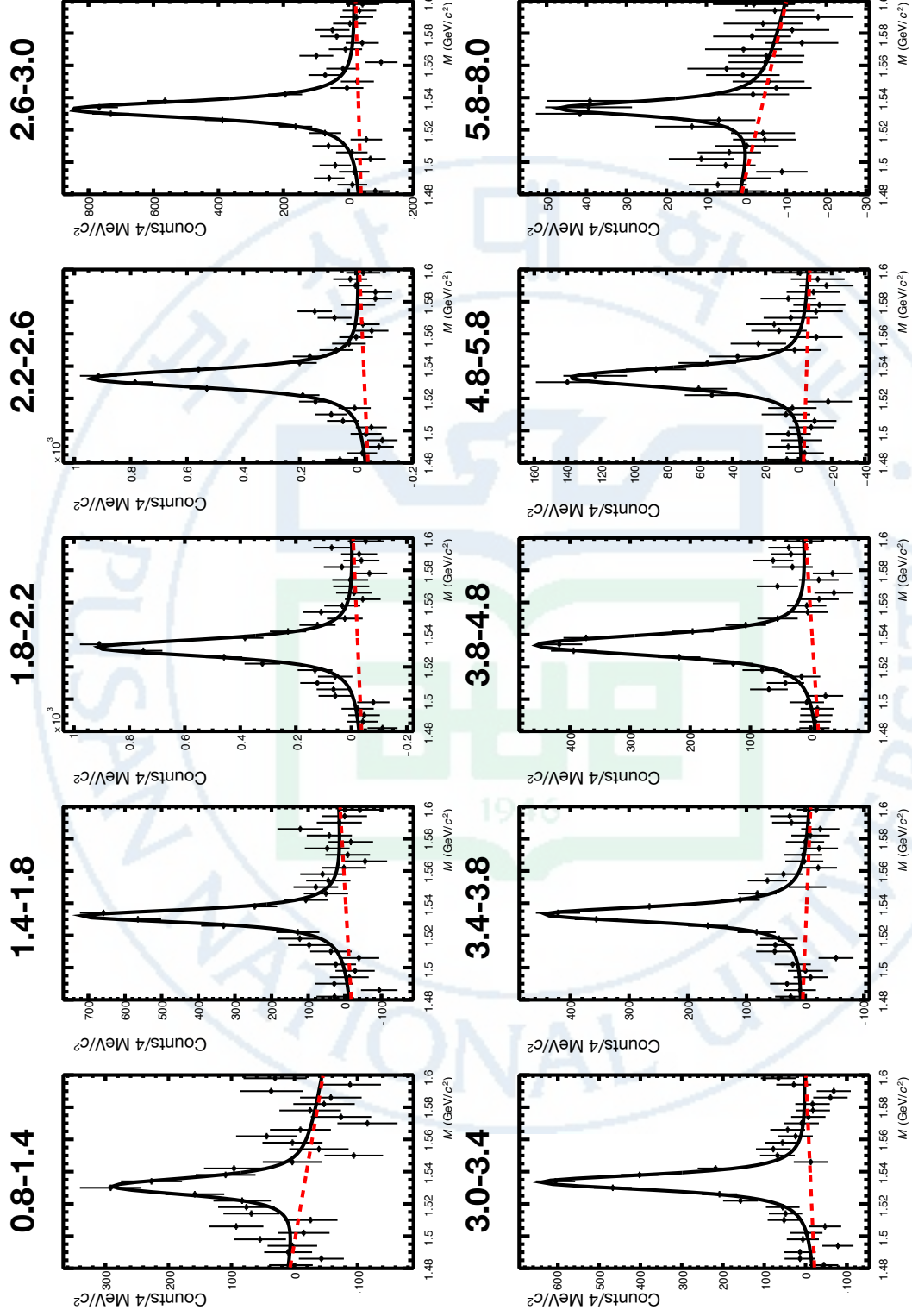


Figure 3.25: Invariant mass distributions after subtraction of the mixed-event background in central event (0-20%) in p-Pb collisions. The solid curve represents the combined fit, while the dashed line describes the residual background.

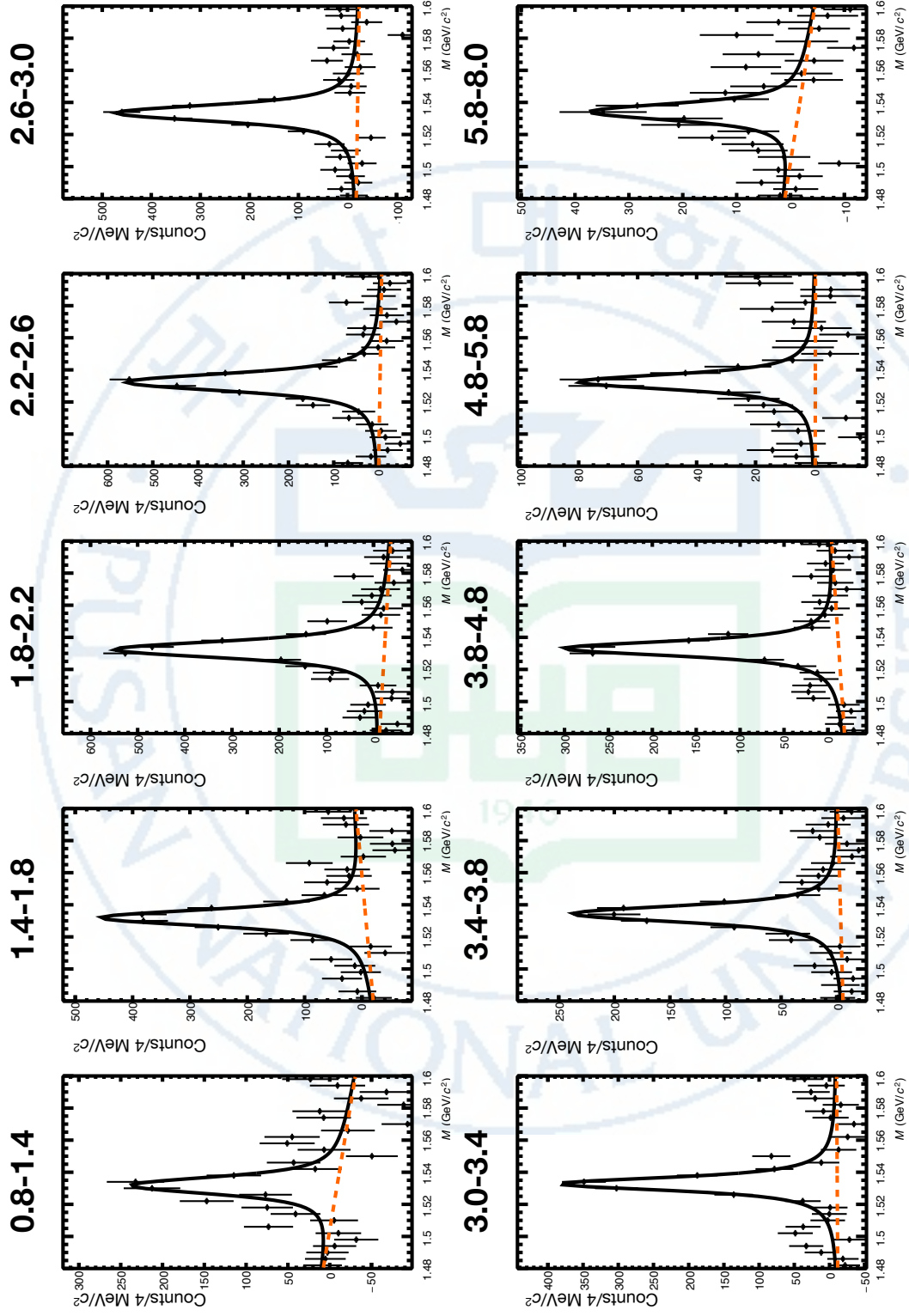


Figure 3.26: Invariant mass distributions after subtraction of the mixed-event background in 20-40% centrality interval in p-Pb collisions. The solid curve represents the combined fit, while the dashed line describes the residual background.



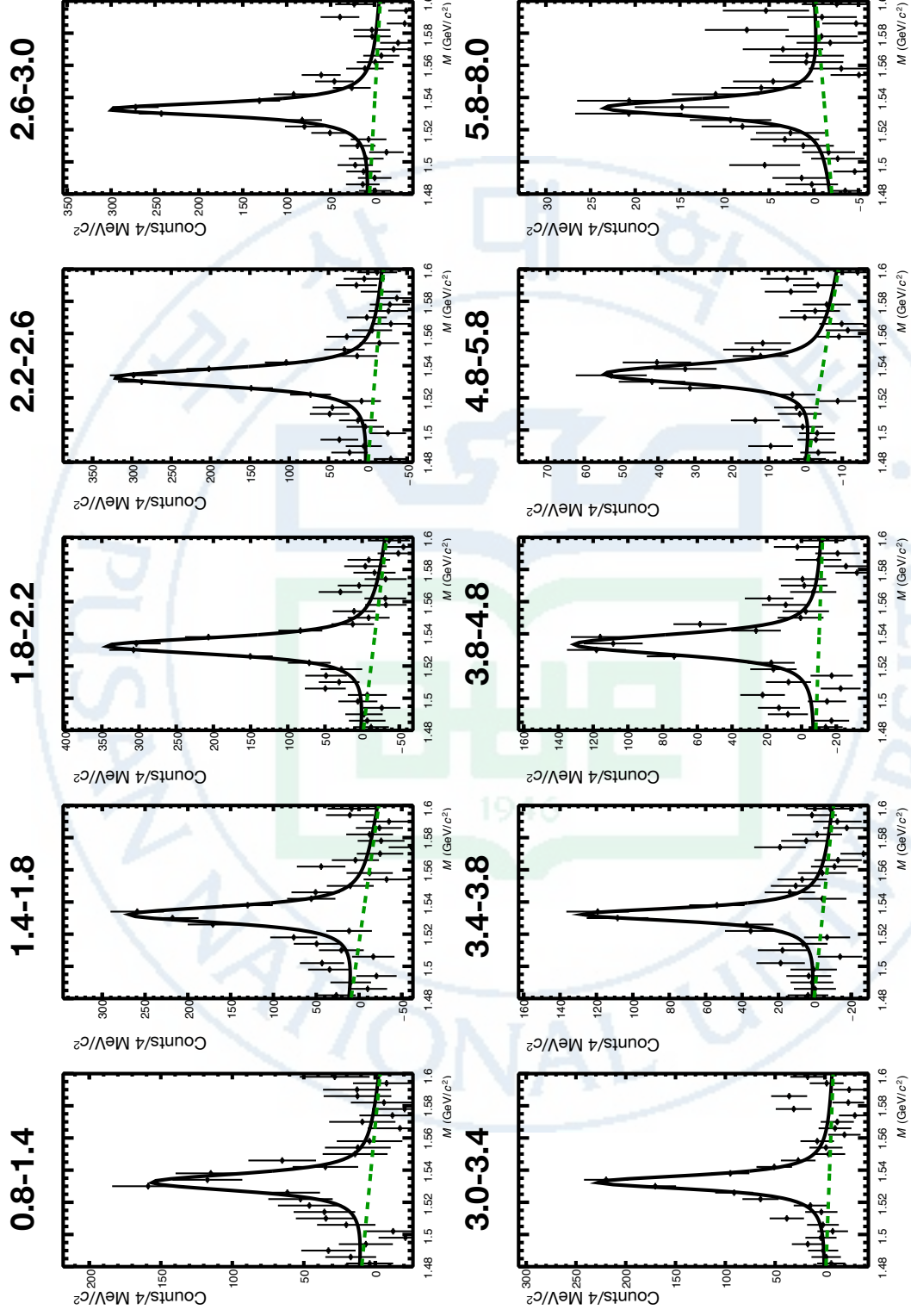


Figure 3.27: Invariant mass distributions after subtraction of the mixed-event background in 40-60% centrality interval in p-Pb collisions. The solid curve represents the combined fit, while the dashed line describes the residual background.

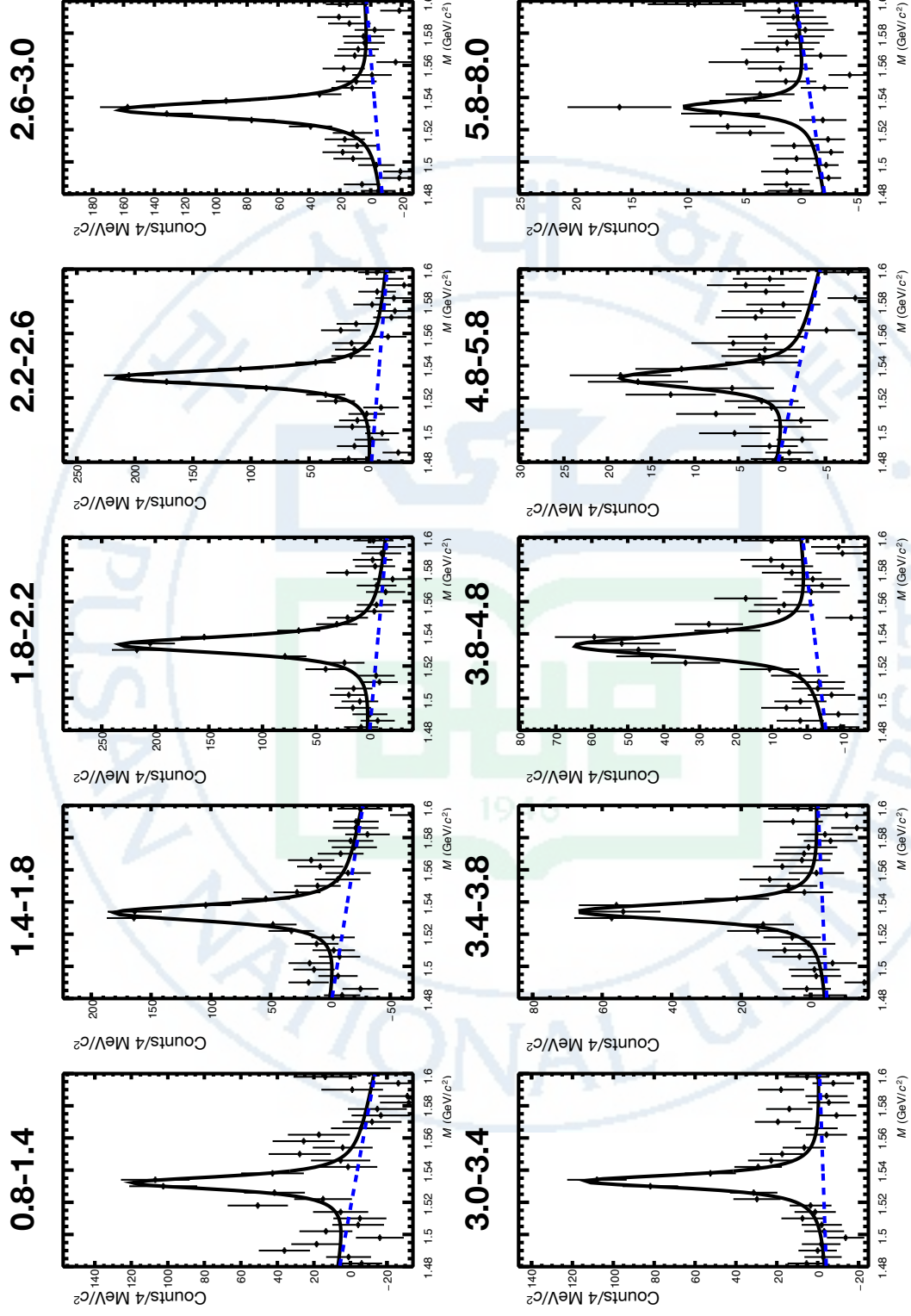


Figure 3.28: Invariant mass distributions after subtraction of the mixed-event background in peripheral event (60-100%) in p-Pb collisions. The solid curve represents the combined fit, while the dashed line describes the residual background.

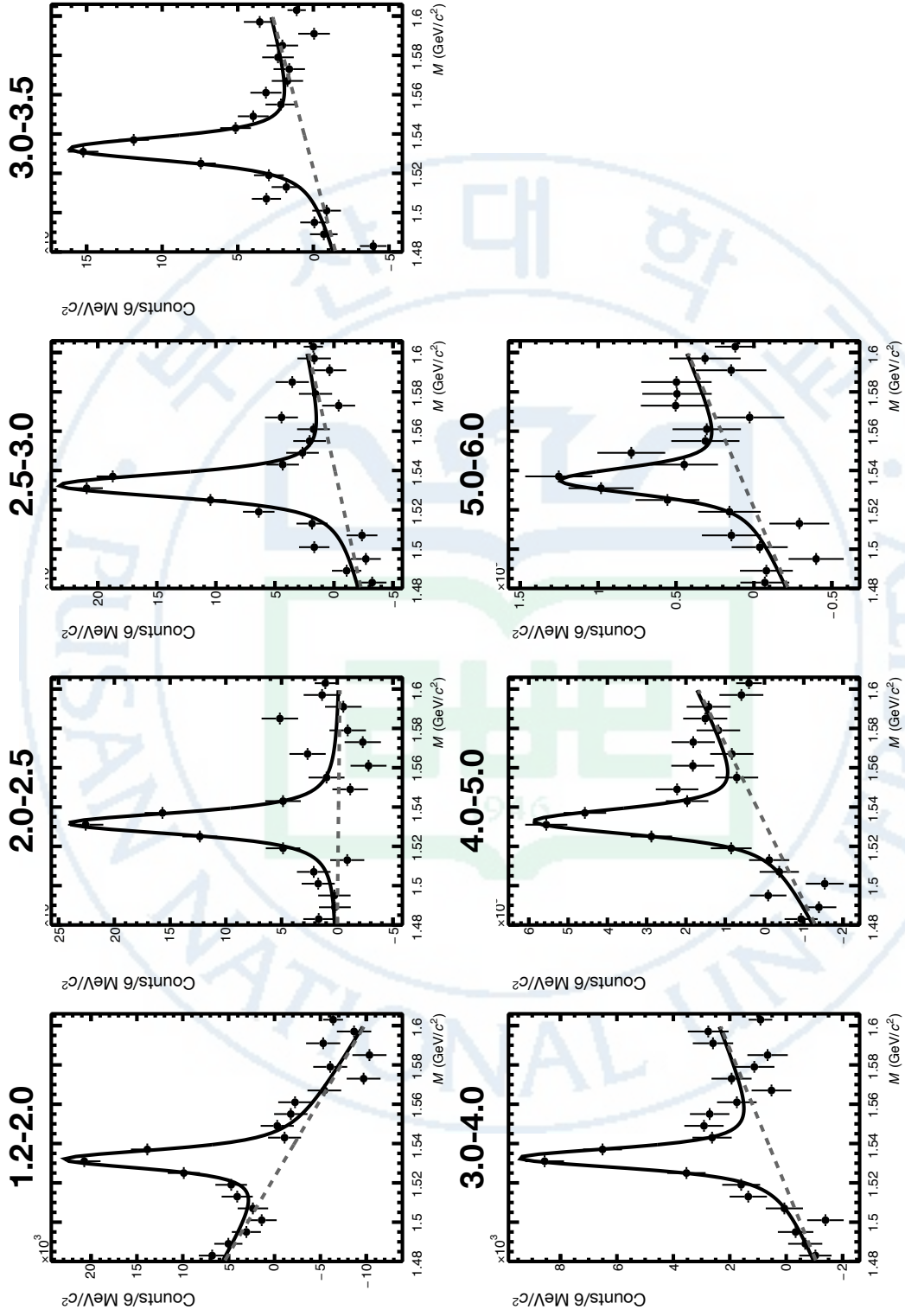


Figure 3.29: Invariant mass distributions after subtraction of the mixed-event background from minimum-bias events in Pb-Pb collisions. The solid curve represents the combined fit, while the dashed line describes the residual background.

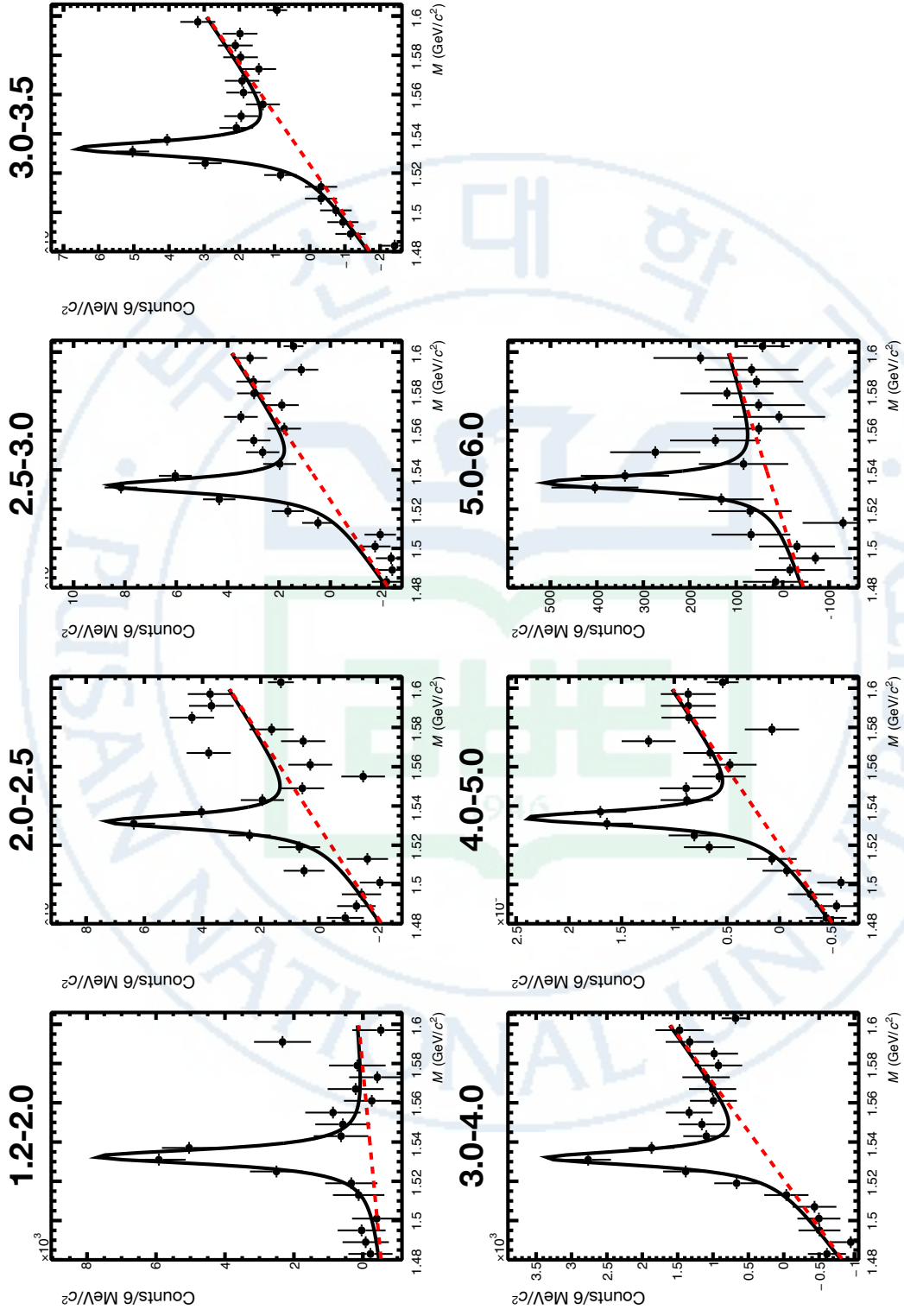


Figure 3.30: Invariant mass distributions after subtraction of the mixed-event background from central events (0-10%) in Pb-Pb collisions. The solid curve represents the combined fit, while the dashed line describes the residual background.

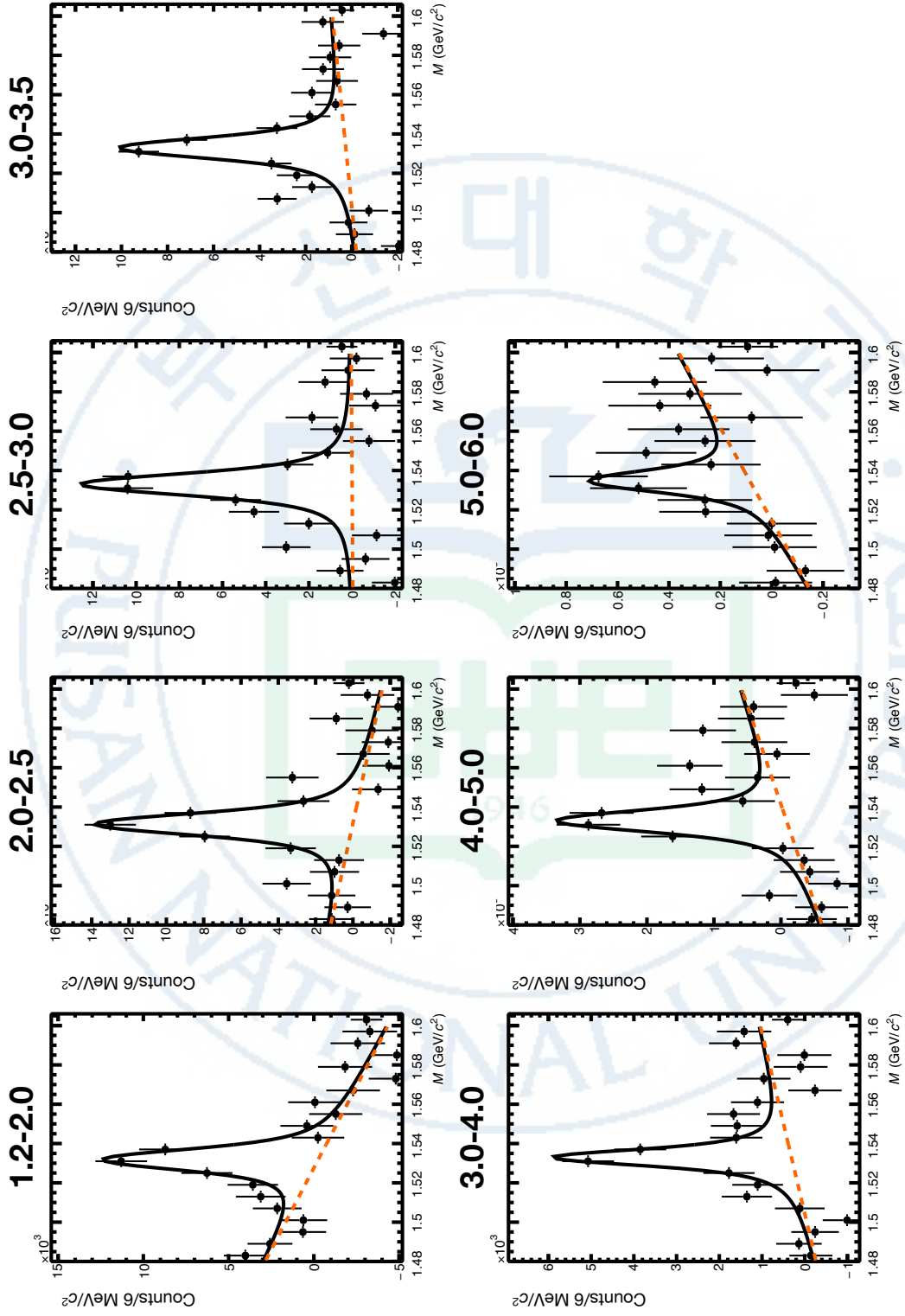


Figure 3.31: Invariant mass distributions after subtraction of the mixed-event background from semi-central event (10-40%) in Pb-Pb collisions. The solid curve represents the combined fit, while the dashed line describes the residual background.



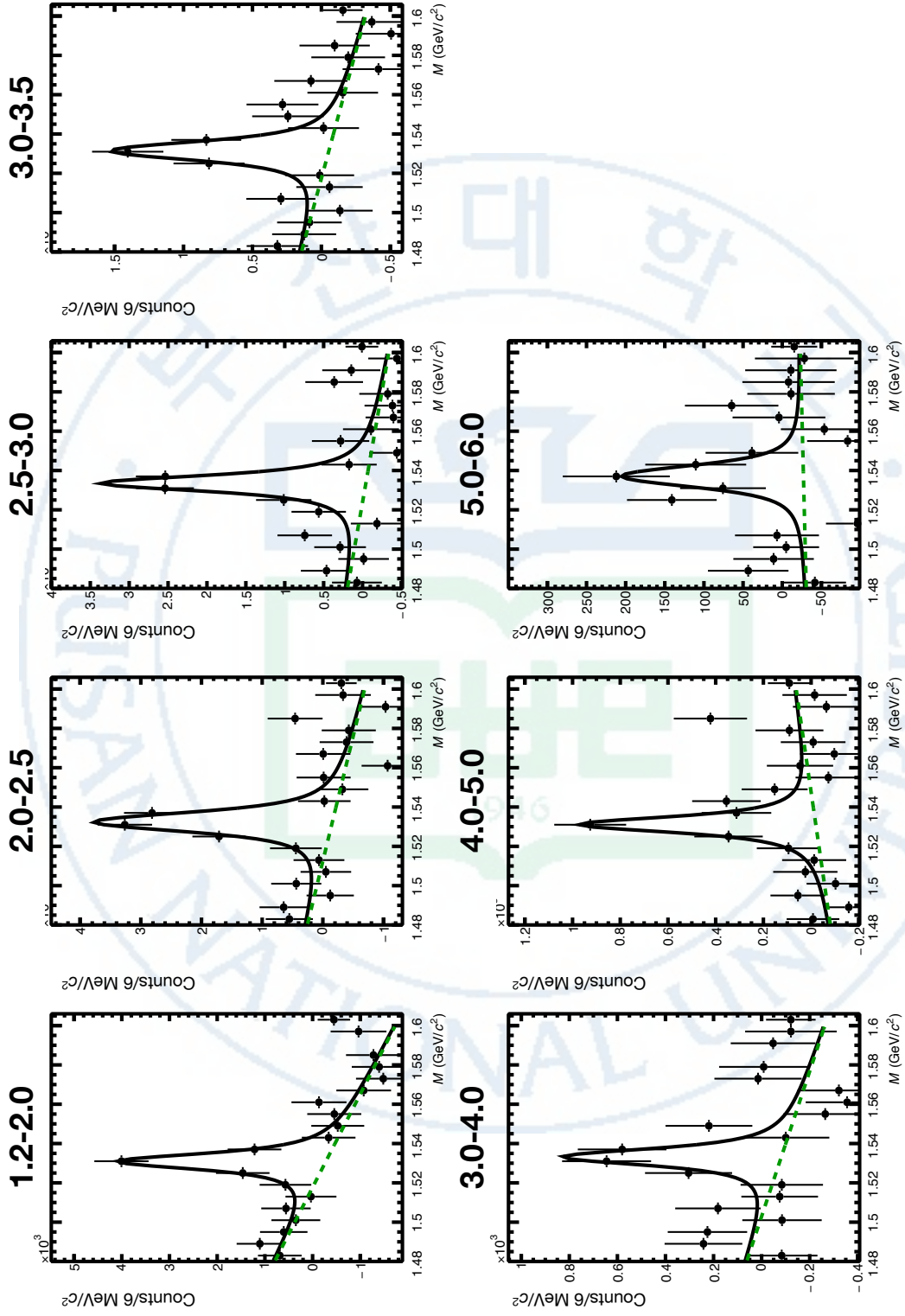


Figure 3.32: Invariant mass distributions after subtraction of the mixed-event background from peripheral event (40-80%) in Pb-Pb collisions. The solid curve represents the combined fit, while the dashed line describes the residual background.

$\Xi(1530)^0$  as a function of  $p_T$  in Figure. 3.34. The raw yields of  $\Xi(1530)^0$  have been extracted from the Voigtian fit for the four multiplicity bins (+ NSD events) in p-Pb and three centrality bins (+ MB events) in Pb-Pb collisions and the yields as a function of  $p_T$  are shown in Figure 3.35.

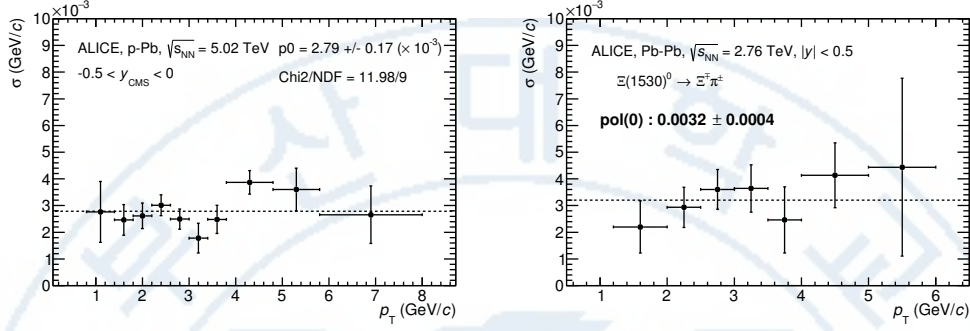


Figure 3.33:  $\sigma$  fit parameters as a function of  $p_T$  in MB in p-Pb collisions (left) and in Pb-Pb collisions (right).

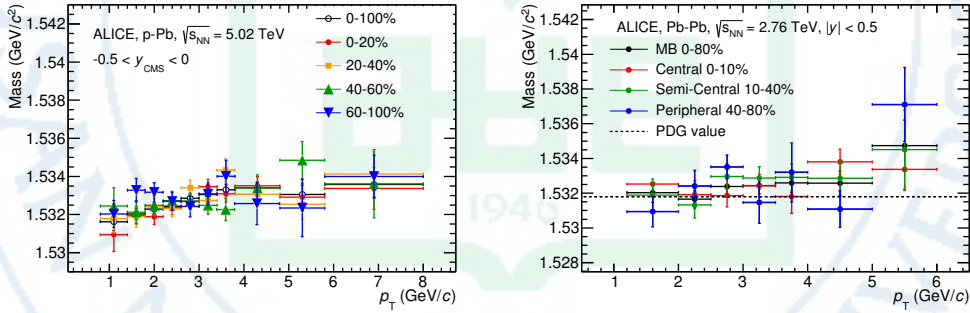


Figure 3.34:  $\Xi(1530)^0$  mass distribution as a function of  $p_T$  in each multiplicity classes in p-Pb collisions (left) and the different centrality classes in Pb-Pb (right). The mass values are obtained from fit of the Voigtian function.

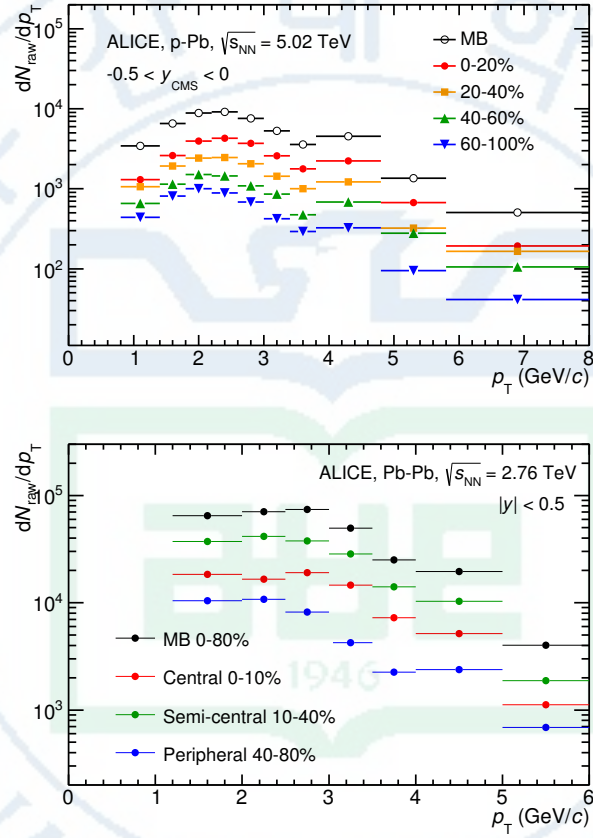


Figure 3.35: Raw spectra of  $\Xi(1530)^0$  obtained by integrating the Voigtian fit function for different multiplicities in p-Pb collisions (top) and different centrality classes in Pb-Pb collisions (bottom). Only the statistical errors are reported.

## 3.2 Efficiency correction

The raw yields were corrected for geometrical acceptance and reconstruction efficiency ( $A \times \epsilon$ ) of the detector (Figure 3.36). By using the DPMJET 3.05 event generator [36] and the GEANT 3.21 package [37], a sample of about 100 million p-Pb events was simulated to compute the corrections for the corresponding collisions. The  $A \times \epsilon$  is obtained from the ratio between the number of reconstructed  $\Xi(1530)^0$  and number of generated  $\Xi(1530)^0$  in the same  $p_T$  bin and rapidity interval. Since the correction factors for different multiplicity classes are in agreement with correction factor from MB events within statistical uncertainty, the latter was used for all multiplicity classes to avoid fluctuation on efficiency due to small statistics.

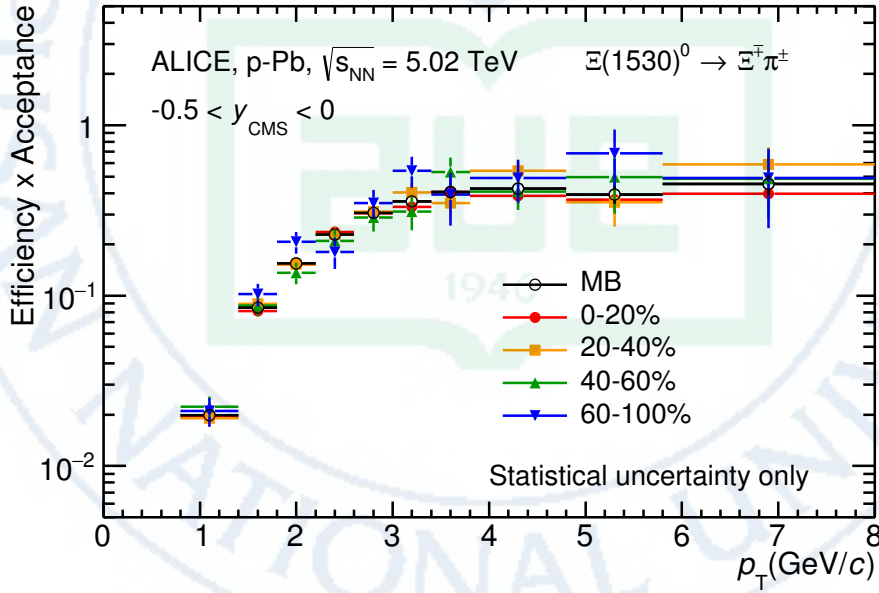


Figure 3.36: Geometrical acceptance and the reconstruction efficiency ( $A \times \epsilon$ ) for  $\Xi(1530)^0$  in  $-0.5 < y_{CMS} < 0$  in p-Pb collisions. Only statistical uncertainties are shown.

Because the generated  $\Xi(1530)^0$  spectra have different shapes than the measured  $\Xi(1530)^0$  spectra, it is necessary to weight the generated and reconstructed

$\Xi(1530)^0$  spectra in the simulation. Figure 3.37 shows the generated and reconstructed  $\Xi(1530)^0$  spectra plotted with the measured  $\Xi(1530)^0$  spectrum from MB events. As shown in Figure 3.37, the generated and measured  $\Xi(1530)^0$  spectra have a different shape, especially in the low  $p_T$  region. The generated  $\Xi(1530)^0$  spectrum decreases with increasing  $p_T$  about  $0.5 < p_T < 1$  GeV/c, while the fit of the measured  $\Xi(1530)^0$  spectrum reaches a local maximum at  $p_T \sim 1$  GeV/c. The correction  $\varepsilon$  is observed to change rapidly over this  $p_T$  range. Therefore, in order to make sure that generated and reconstructed spectrum have the shape of the measured  $\Xi(1530)^0$  spectrum, a weighting procedure on efficiency was applied. An iterative procedure is performed to determine the weighted efficiency as described below.

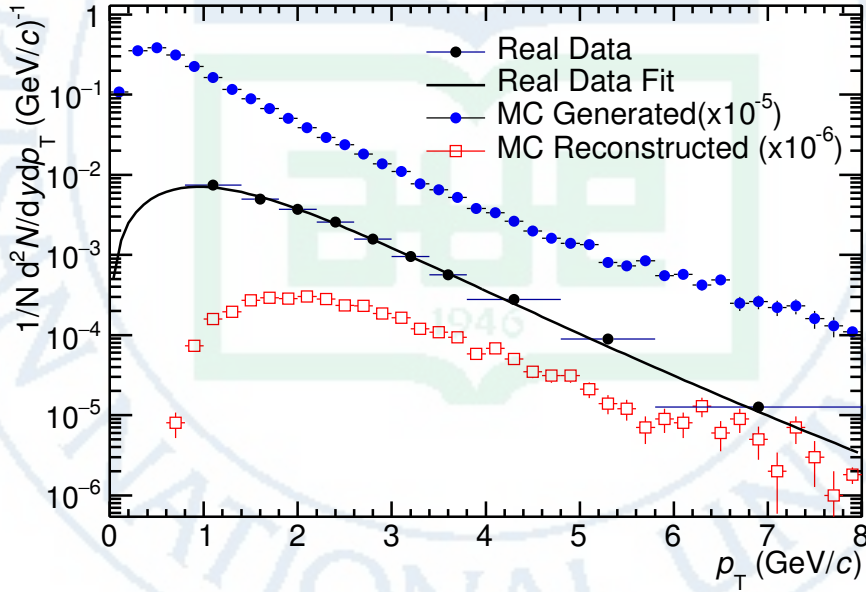


Figure 3.37: Real corrected  $\Xi(1530)^0$  spectrum is shown as black dots for the minimum-bias events with Lévy-Tsallis fit (black curve). The generated (un-weighted) spectrum are presented as blue dots and reconstructed (un-weighted) spectrum is shown as red squares.

1. The unweighted efficiency,  $\varepsilon$ , is calculated.
2. This  $\varepsilon$  is used to correct the measured  $\Xi(1530)^0$  spectrum.



3. The corrected  $\Xi(1530)^0$  spectrum is fitted.
4. This fit is used to weight the simulated  $\Xi(1530)^0$  spectrum. A  $p_T$ -dependent weighting is applied to the generated  $\Xi(1530)^0$  spectrum so that it follows the fit. The same weight is applied to the reconstructed  $\Xi(1530)^0$  spectrum.
5. The weighted  $\varepsilon$  is calculated.
6. Step 2-5 are repeated (with the weighted  $\varepsilon$  from step 5 used as the input for step 2) until the  $\varepsilon$  values are observed to change by  $< 0.1\%$  (relative) between iterations. It is observed that four iterations are sufficient for this procedure to converge.

Finally, the re-weighted efficiency is obtained, and the distribution as a function of  $p_T$  is shown in Figure 3.38.

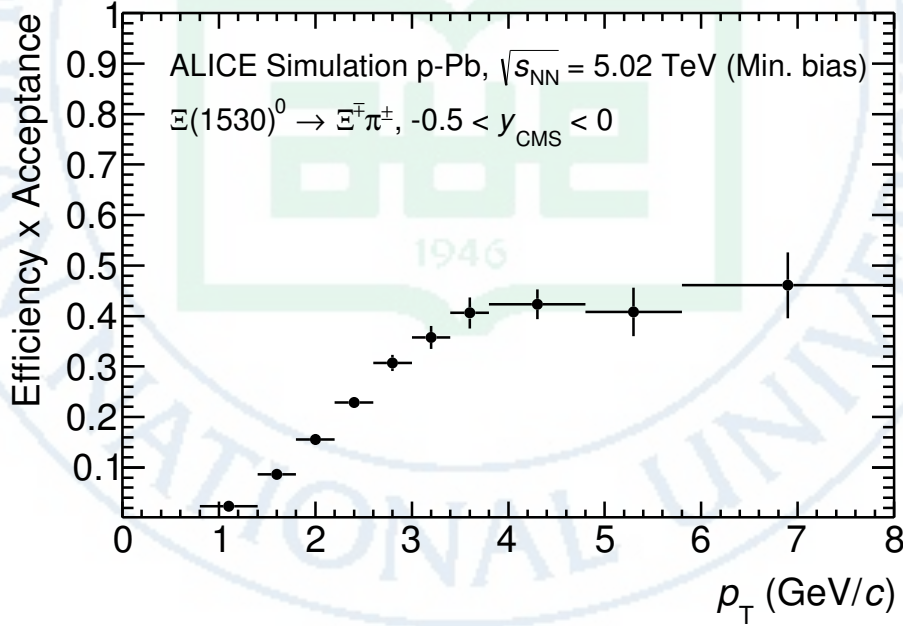


Figure 3.38: Efficiency as a function of  $p_T$  in minimum bias events in p-Pb collisions. Statistical uncertainties are presented as bar.

In order to obtain the efficiency correction for results in Pb-Pb collisions, MC events are generated using Heavy Ion Jet Interaction Generator (HIJING). The

generated events are passed through a GEANT3 model of the ALICE experiment with a realistic description of the detector response.

Because efficiency is observed to depend on centrality, centrality dependent efficiencies are applied to get corrected  $p_T$ -spectra. The weighing procedure which was adopted to correct the efficiency in p-Pb is also applied to the efficiency obtained in Pb-Pb. The  $A \times \epsilon$  multiplied by branching ratio of  $\Xi(1530)^0$  is shown in Figure 3.39.

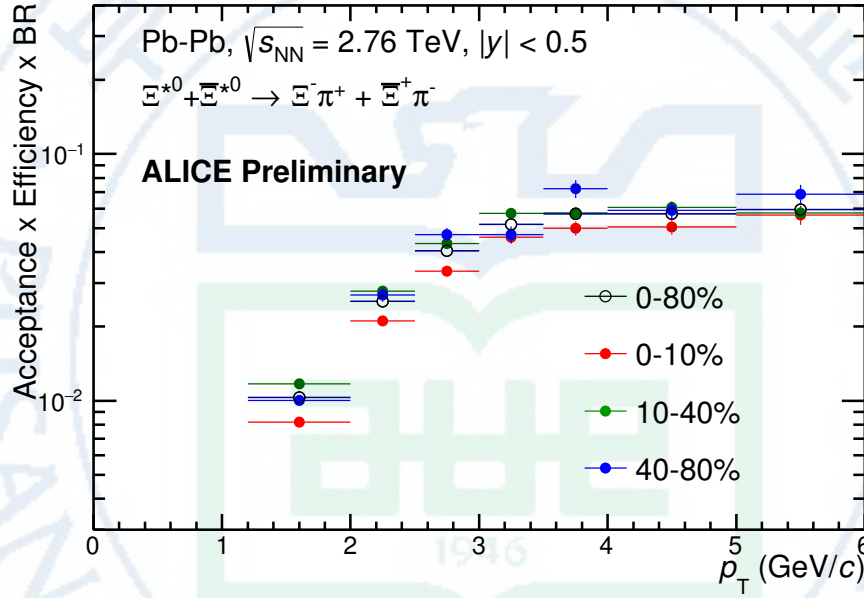


Figure 3.39: Efficiency as a function of  $p_T$  for different centrality classes in Pb-Pb collisions

### 3.3 Corrected $p_T$ -spectra

The  $p_T$  spectrum is the number of produced particles of a given type in the desired interval of phase-space divided by the number of inelastic collisions. Such distribution is calculated as:

$$\frac{1}{N} \times \frac{d^2 N}{dy dp_T} = \frac{1}{N_{E,PhysSel}} \times \frac{N_{raw}}{dp_T dy} \frac{1}{\epsilon} \frac{N_{total}^{MC}}{N_{PVcut}^{MC}}, \quad (3.3)$$

where  $N$  represents the number of events, the  $\frac{d^2 N}{dy dp_T}$  is the yield per range of rapidity  $y$ , per range in  $p_T$ . On the right side,  $N_{E,PhysSel}$  is the number of events triggered by the physics selection.  $N_{raw}$  is the raw yield extracted in  $p_T$  bins and rapidity bin of width  $\Delta y = 0.5$  in p-Pb and  $\Delta y = 1.0$  in Pb-Pb. The  $\epsilon$  is the reconstruction efficiency estimated from Monte Carlo simulations which was explained in Section 3.2. The  $\frac{N_{total}^{MC}}{N_{PVcut}^{MC}}$  is the ratio of the total number of particles from MC divided by the number of particles from MC after the Primary-Vertex cut is imposed. It takes into account the fraction of particle lost after imposing the PV cut. For MB result in p-Pb collisions, a normalization for the non-single diffractive cross section is applied, and it is 0.964 [23]. The obtained spectrum with NSD and the spectra from different multiplicity classes in p-Pb are shown in Figure 3.40, and the spectra from different centrality classes in Pb-Pb are shown in Figure 3.41.

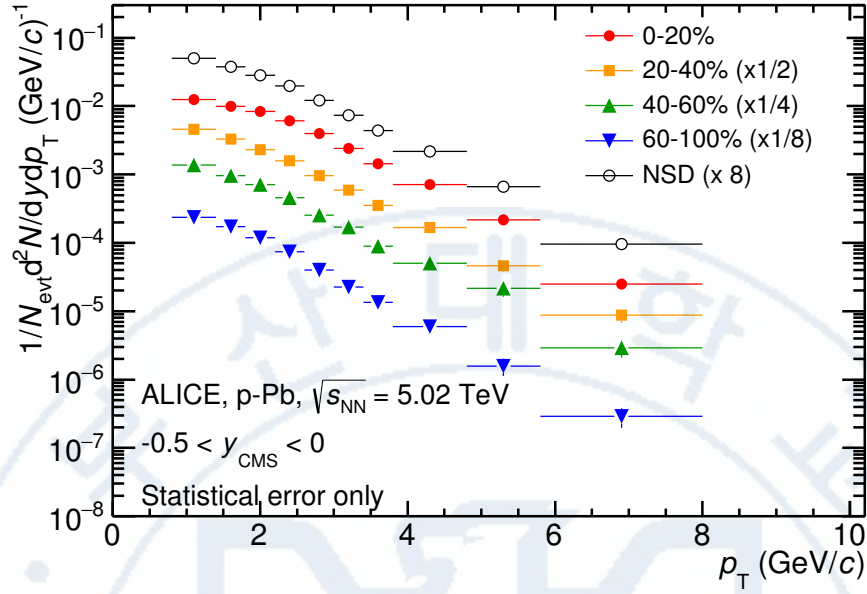


Figure 3.40: Corrected  $p_T$ -spectra of  $\Xi(1530)^0$  for NSD and different multiplicity classes in p-Pb collisions.

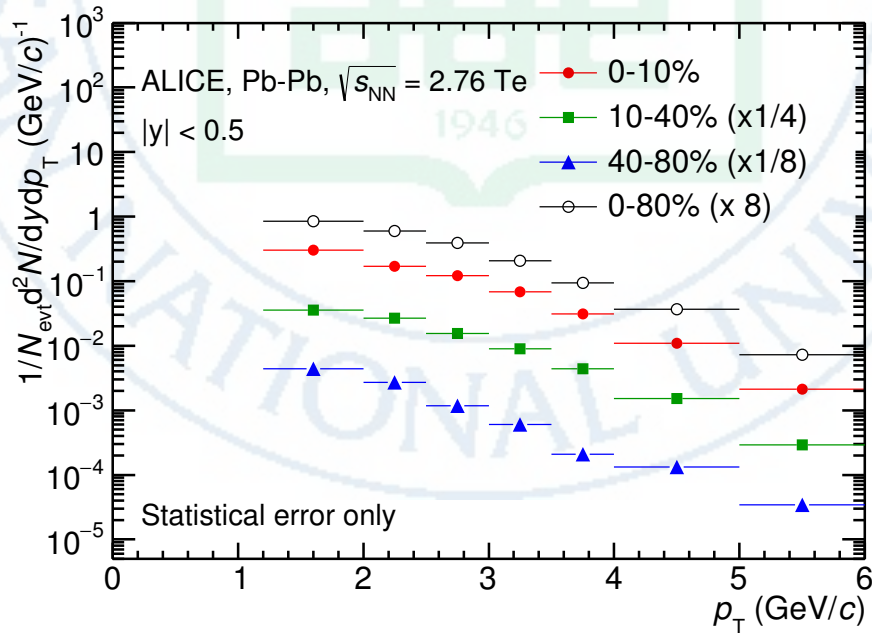


Figure 3.41: Corrected  $p_T$ -spectra of  $\Xi(1530)^0$  for different centrality classes in Pb-Pb collisions.

### 3.4 Systematic uncertainties

In order to obtain systematic uncertainties, same procedure which was done to get the result with default cut is performed many times by varying the possible permutation of analysis. (e.g., variation of topological cuts, different method for signal extraction). The general strategy for evaluating systematic uncertainties is described as following:

1. Choose one set of parameters for the analysis as default cut
2. Observe the deviation of yield when one parameter is changed
3. The systematic uncertainty is calculated for a given source as the RMS deviation of the available sources.
4. Barlow [38] check has been performed to verify whether it is likely due to a systematic effect instead of statistical fluctuation.
5. The total systematic uncertainty, taking into account all the different sources, is the sum in quadrature of each source.

Several groups which can contribute systematic uncertainty were studied. In particular, those that come from signal extraction, topological and kinematical selection cuts, track quality selection and  $n\sigma$  TPC PID variation were checked. The description of each source of systematic uncertainty is written below:

#### **Signal extraction**

Signal was extracted by varying the yield calculating method. Default method for signal extraction was integrating the Voigtian fit function and alternative one was bin counting method. The normalization range for mixed-event distribution was varied. Not only mixed-event background, the Like-Sign distribution and polynomial fit function were performed as different background estimators. These three sources were taken account into the systematic source of signal extraction.



The systematic uncertainty from signal extraction is computed as the sum in quadrature of three sources.

### **Topological selection**

To evaluate the stability of the chosen set of values for the topological cuts, the effects of loosening and tightening the cuts were investigated. The cuts are changed once at a time. Total systematic uncertainty from topological selection is calculated by summation in quadrature of nine sources.

### **TPC $N_{cluster}$ selection**

The TPC  $N_{cluster}$  is related to the quality of tracks, and the cut was applied for all daughter tracks. The nominal cut is that  $N_{cluster}$  is larger than 70 and value has been varied by 10%.

### **TPC $dE/dx$ selection**

In order to evaluate effect due to the TPC- $dE/dx$  selections, the  $\sigma_N$  selection was varied to  $N = 2.5$  and  $3.5$ .

### **$p_T$ shape correction**

As described in Section 3.2, due to the shape differences between the measured and generated and reconstructed  $\Xi(1530)^0$  spectra, we have applied reweighing procedure. This correction is considered as a contributor of systematic uncertainty as  $p_T$  shape correction.

### **Mass window range selection**

In order to select  $\Xi$  from  $\Lambda\pi$  invariant mass distribution, we gave the mass window of  $\pm 7 \text{ MeV}/c^2$  from PDG value of  $\Xi$  mass. Such range of window has been varied to  $\pm 6$  and  $\pm 8 \text{ MeV}/c^2$  in order to estimate the corresponding systematic uncertainty.

### Vertex range selection

The distribution of vertex-z is shown in Figure 3.1 with the indication of nominal cut of 10 cm. The cut on  $|V_z|$  was varied to  $\pm 9$  cm,  $\pm 11$  cm.

### Tracking efficiency

Systematic uncertainty on tracking efficiency from ITS + TPC combined track was assigned as 3% in p-Pb and 4% in Pb-Pb collision system.[39]

Finally, total systematic uncertainty is the sum in quadrature of sources listed above. Figure 3.42 and Figure 3.43 show the total systematic uncertainty in minimum bias events and different multiplicity classes in p-Pb collisions, respectively. Figures 3.44 and 3.45 present the total systematic uncertainty in minimum bias events and different centrality classes in Pb-Pb collisions.

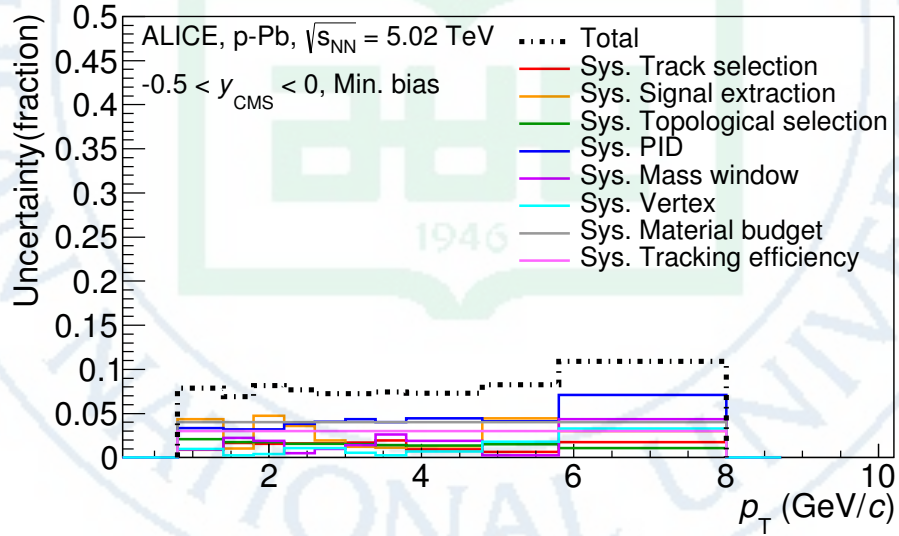


Figure 3.42: Summary of the contributions to the systematic uncertainty in minimum bias events in p-Pb collisions. The dashed black line is the sum in quadrature of all the contributions.

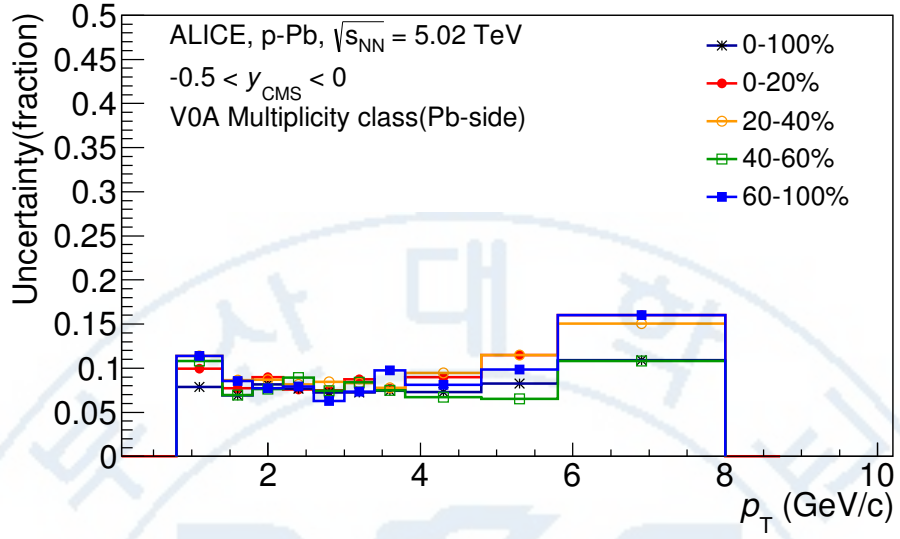


Figure 3.43: Systematic uncertainties for each multiplicity classes in p-Pb collisions.

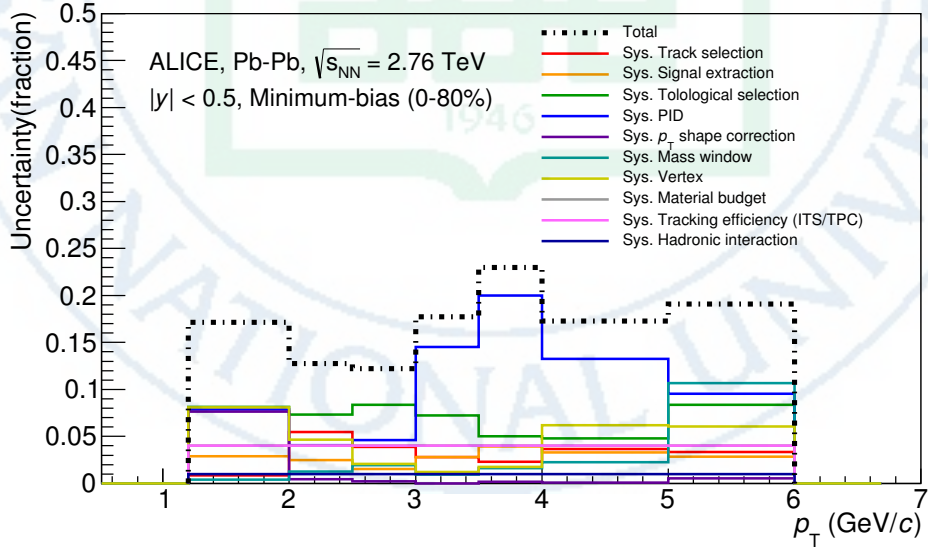


Figure 3.44: Summary of the contributions to the systematic uncertainty in minimum bias events in Pb-Pb collisions. The dashed black line is the sum in quadrature of all the contributions.

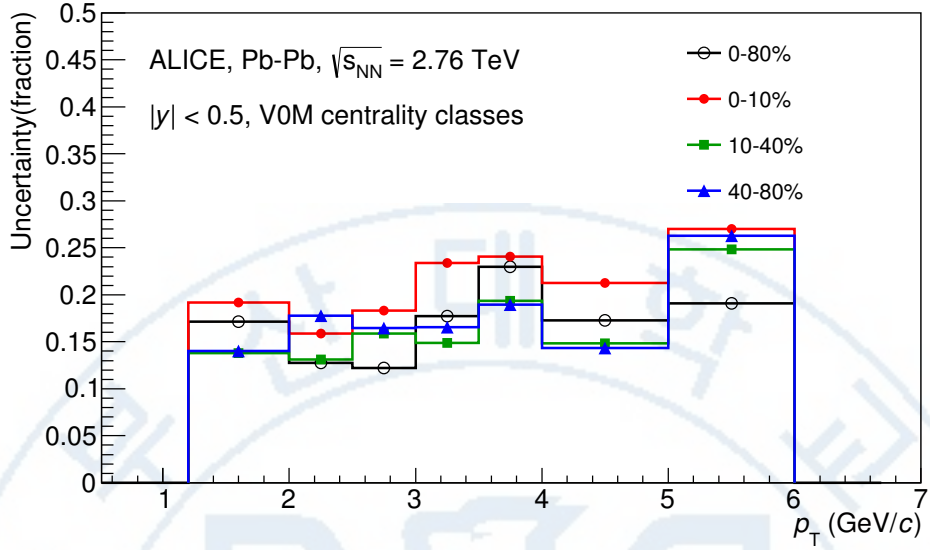


Figure 3.45: Systematic uncertainties for each multiplicity classes.

Source of uncertainty	p-Pb	Pb-Pb
<i>p<sub>T</sub></i> -dependent		
Tracking efficiency	3%	4%
Tracks selection	1-2%	1-5%
Topological selection	1-2%	5-8%
PID	3-7%	4-20%
Signal extraction	1-5%	1-4%
<i>p<sub>T</sub></i> shape correction	-	0-8%
Mass window ( $\Xi^\pm$ )	4%	0.5-11%
Vertex selection	3%	1-8%
<i>p<sub>T</sub></i> -independent		
Hadronic interaction	-	1%
Material budget	4%	4%
Branching ratio	0.3%	0.3%
Total	8-12%	9-28 %

Table 3.4: Summary of the systematic uncertainties in minimum-bias events. Minimum and maximum values from all *p<sub>T</sub>* intervals and multiplicity classes in p-Pb, centrality classes in Pb-Pb are shown for each source.

# Chapter 4

## Results and discussion

The transverse momentum distributions of the double-strange hyperon resonance,  $\Xi(1530)^0$ , produced in p-Pb collisions at  $\sqrt{s_{NN}} = 5.02$  TeV and Pb-Pb collisions at  $\sqrt{s_{NN}} = 2.76$  TeV were measured in the mid-rapidity range. From the measurement, integrated particle yield-ratios and  $\langle p_T \rangle$  with system size have been obtained. In the present Chapter, these results are compared with model predictions and discussed in connection with the following topics:

- Comparison of  $p_T$ -spectra
- Particle production mechanism in hadronic phase
- Strangeness enhancement in small system
- Mean transverse momentum

### 4.1 $\Xi(1530)^0$ transverse momentum spectra

The corrected  $p_T$ -spectra of  $(\Xi(1530)^0 + \overline{\Xi(1530)}^0)/2$  are shown in Figure 4.1 for p-Pb collisions and Pb-Pb collisions. The statistical and systematic uncertainties are reported respectively as the error bars and the boxes on the plot. The upper panel on Figure 4.1 shows the  $p_T$ -spectra in 0-20%, 20-40%, 40-60%, 60-100% multiplicity classes and spectrum from NSD events in p-Pb collisions at  $\sqrt{s_{NN}} = 5.02$  TeV in  $-0.5 < y_{CMS} < 0$  rapidity range. The bottom panel on Figure 4.1 presents the  $p_T$ -spectra in 0-10%, 10-40%, 40-80% and 0-80% centrality bins



in Pb–Pb collisions at  $\sqrt{s_{\text{NN}}} = 2.76$  TeV in  $|y| < 0.5$  rapidity range. Measured  $p_{\text{T}}$ -range of p–Pb collisions is  $0.8 < p_{\text{T}} < 8.0$  GeV/ $c$  whereas the spectra from Pb–Pb collisions are obtained with  $1.2 < p_{\text{T}} < 6.0$  GeV/ $c$  due to difficulty of signal extraction in low and high  $p_{\text{T}}$  region (see paragraph 3.1.4).

In order to estimate the  $p_{\text{T}}$ -spectra in low  $p_{\text{T}}$ -region where there are no experimental data points, a function that fits the spectra in the measured region is used. By using the fit function, integrated-yield of  $\Xi(1530)^0$  and  $\langle p_{\text{T}} \rangle$  can be obtained from  $p_{\text{T}}$  at 0 GeV/ $c$ . In case of the results in p–Pb collisions, the  $p_{\text{T}}$ -spectra are fitted by Lévy-Tsallis function while the  $p_{\text{T}}$ -spectra in Pb–Pb collisions are described with Boltzmann fit function.

The Lévy-Tsallis functional form describes the exponential shape of spectra at low  $p_{\text{T}}$  and the power-law shape at large  $p_{\text{T}}$  with an inverse slope parameter  $C$  and an exponent parameter  $n$ .

$$\frac{d^2N}{dydp_{\text{T}}} = p_{\text{T}} \frac{dN}{dy} \frac{(n-1)(n-2)}{nC[nC + m_0(n-2)]} \left[ 1 + \frac{\sqrt{p_{\text{T}}^2 + m_0^2} - m_0}{nC} \right]^{-n} \quad (4.1)$$

Free parameters are  $n$ ,  $C$ , and the integrated yield  $dN/dy$ . The  $m_0$  is fixed to the mass of the particle. The Boltzmann fit function is

$$\frac{d^2N}{dydp_{\text{T}}} = p_{\text{T}} \frac{dN}{dy} m_T e^{-\frac{m_T}{T}}, \quad (4.2)$$

where  $m_T = \sqrt{p_{\text{T}}^2 + m_0^2}$ ,

In addition, EPOS predictions [40, 41, 42, 43] is drawn as dashed lines for  $p_{\text{T}}$ -spectra in Pb–Pb collisions. It shows that the EPOS predictions reasonably well describe the  $p_{\text{T}}$ -spectra for peripheral events, 40-80%, while it does not match the  $p_{\text{T}}$ -spectra in central collisions, especially in the low  $p_{\text{T}}$  region.

The integrated yields of  $\Xi(1530)^0$  have been obtained in each multiplicity/centrality classes and are summarized in Table 4.1. Statistical and systematic uncertainties are quoted. The systematic errors include not only the error discussed in Section

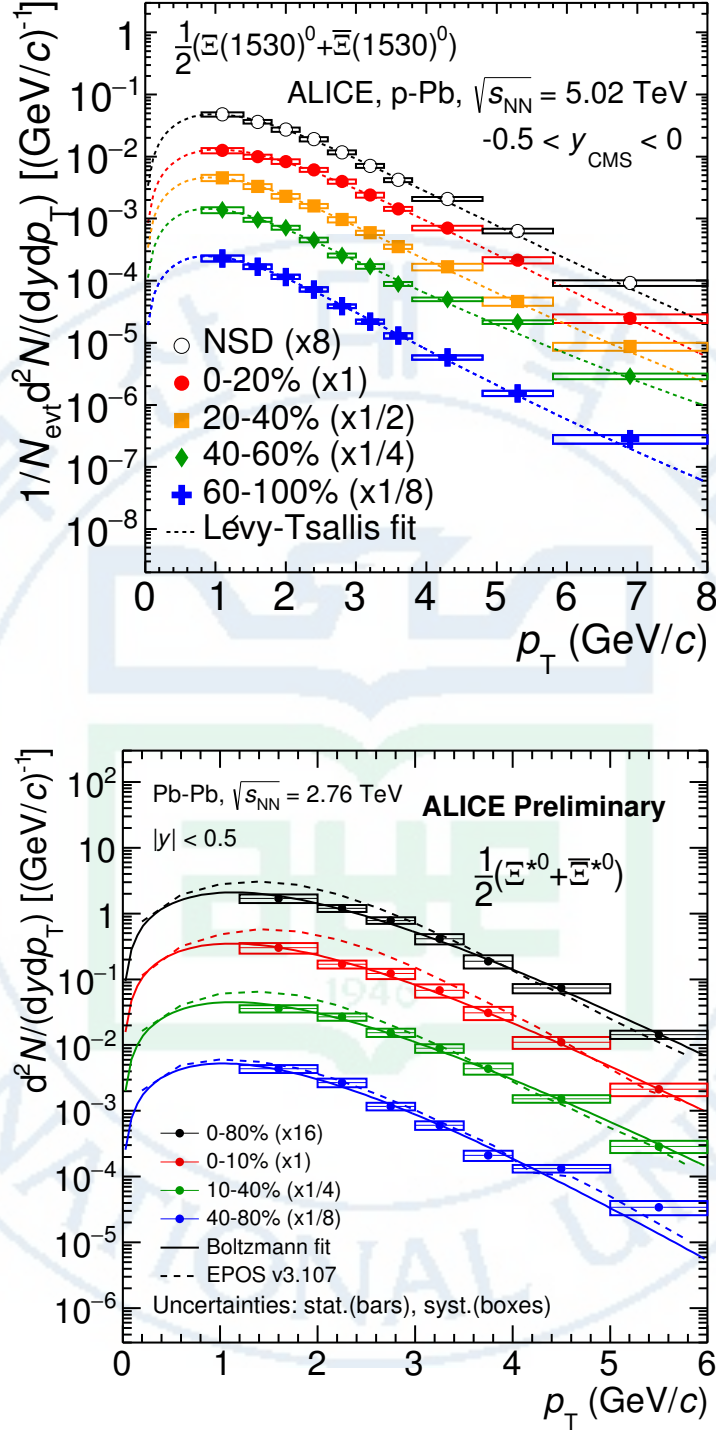


Figure 4.1: Corrected  $p_T$ -spectrum from NSD events and spectra from multiplicity dependent event classes in p-Pb collision system (top) and spectra in different centrality classes in Pb-Pb collision system (bottom). Statistical uncertainties are presented as bar and systematical uncertainties are plotted as boxes.

3.4 but also contribution due to the variation of fit function for  $p_T$ -spectra which is associated to the extrapolation to the un-measured region at low  $p_T$ .

Collision	Centrality	$dN/dy \times (10^{-3})$	$\langle p_T \rangle$ (GeV/c)
p-Pb	0-20%	$27.3 \pm 0.6 \pm 2.4 \pm 1.4$	$1.626 \pm 0.0016 \pm 0.033 \pm 0.059$
	20-40%	$17.7 \pm 0.5 \pm 1.8 \pm 1.6$	$1.482 \pm 0.0020 \pm 0.037 \pm 0.093$
	40-60%	$10.7 \pm 0.3 \pm 1.1 \pm 1.1$	$1.459 \pm 0.0025 \pm 0.045 \pm 0.105$
	60-100%	$3.6 \pm 0.1 \pm 0.4 \pm 0.3$	$1.377 \pm 0.0023 \pm 0.035 \pm 0.082$
	NSD%	$12.5 \pm 0.3 \pm 0.8 \pm 0.8$	$1.540 \pm 0.0016 \pm 0.023 \pm 0.067$
Pb-Pb	0-10%	$733.5 \pm 15.2 \pm 130.3 \pm 54.3$	$1.619 \pm 0.015 \pm 0.072 \pm 0.065$
	10-40%	$382.3 \pm 6.2 \pm 52.2 \pm 25.2$	$1.638 \pm 0.012 \pm 0.046 \pm 0.059$
	40-80%	$80.9 \pm 2.7 \pm 12.4 \pm 21.6$	$1.529 \pm 0.024 \pm 0.043 \pm 0.182$
	0-80%	$283.0 \pm 3.4 \pm 41.9 \pm 21.6$	$1.628 \pm 0.009 \pm 0.053 \pm 0.067$

Table 4.1: Integrated yield,  $dN/dy$ , and  $\langle p_T \rangle$  in each multiplicity/centrality interval. Statistical (first one), systematic uncertainties due to selection criteria (second one) and uncertainties due to extrapolation (third one) from the various fit functions are quoted.

## 4.2 Particle yield ratios

### 4.2.1 Integrated particle ratio to ground state particle

As discussed in Section 1.3.1, resonances can be used as tools to investigate hadronic phase. Because of its short lifetime which is comparable of the lifetime of the fireball, the resonance particle can be regenerated via pseudo-elastic scattering which leads to an increase of the yields. Vice versa, if re-scattering effect due to (pseudo-)elastic scattering in hadronic phase is dominant, the yield that we observe with detectors could decrease. Resonances which have shorter lifetime might be directly affected by hadronic phase because they already decay during that period, correspondingly the daughter particles have more probability to be scattered.

It has been observed that the yields of  $K^*(892)^0$  ( $c\tau \sim 4.2$  fm) resonance is lower than thermal model predictions [44] which could be due to the dominance of re-scattering in the hadronic phase. In contrast, the  $\phi$  meson ( $c\tau \sim 44$  fm) which have 10 times longer lifetime with respect to the lifetime of  $K^*(892)^0$  does not

show decreasing trend and consistent with thermal model expectations [44].

In order to clarify these effects, integrated yields of  $\Xi(1530)^0$  have been measured and compared to the yields of the  $\Xi$  which have the same strangeness content. The ratio of  $\Xi(1530)^0$  to  $\Xi$  as a function of mean charged particle multiplicity densities,  $\langle dN_{\text{ch}}/d\eta_{\text{lab}} \rangle$ , is shown in Figure 4.2. Note that numerator of the ratio is the sum of  $\Xi(1530)^0$  and its anti-particle and denominator is also the sum of  $\Xi^-$  and its anti-particle  $\Xi^+$ .

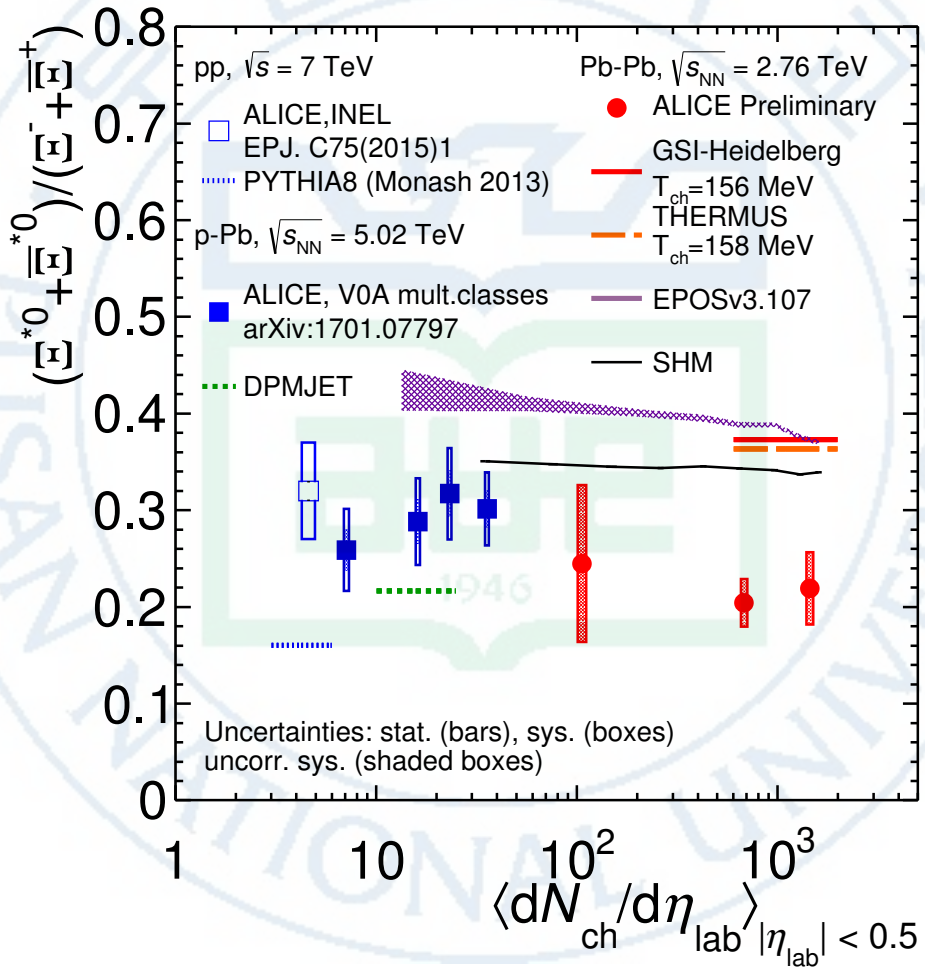


Figure 4.2: Ratio of  $\Xi(1530)^0$  to  $\Xi^-$  measured in pp [45], p-Pb [11, 19] and Pb-Pb collisions as a function of  $\langle dN_{\text{ch}}/d\eta_{\text{lab}} \rangle$  measured at midrapidity. Statistical uncertainties (bars) are shown as well as total systematic uncertainties (hollow boxes) and systematic uncertainties uncorrelated across multiplicity (shaded boxes). A few model predictions are also shown as lines at their appropriate abscissa.



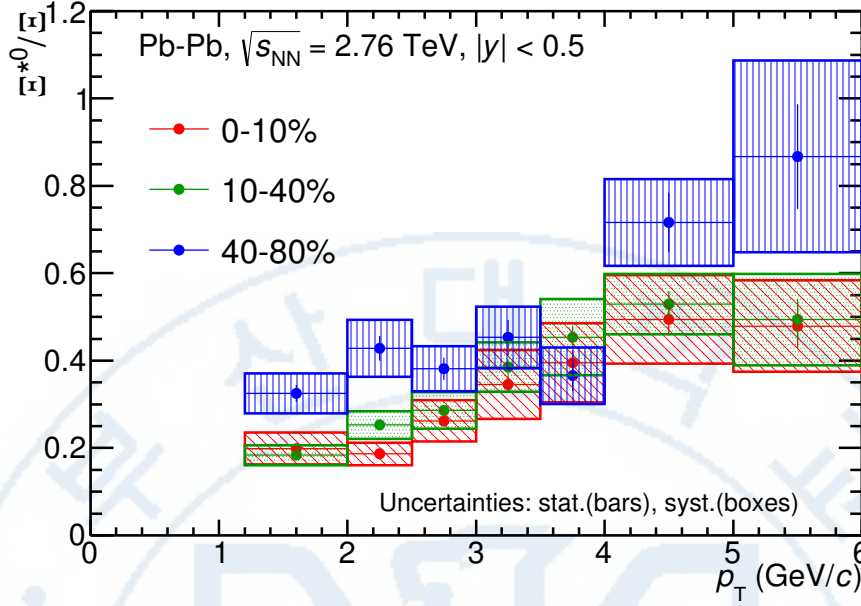


Figure 4.3: Ratio of  $\Xi(1530)^0$  to  $\Xi$  measured in Pb–Pb collisions as a function of  $p_T$  at mid-rapidity. Statistical uncertainties (bars) are shown and total systematic uncertainties (boxes).

As shown in Figure 4.2, the ratios of  $\Xi(1530)^0$  to  $\Xi$  measured in pp and p–Pb collisions are above model calculations from PYTHIA8 and DPMJET. For Pb–Pb collisions,  $\Xi(1530)^0/\Xi$  is lower than predicted by thermal models, despite a lifetime about five times longer with respect to  $K(892)^*0$ . In addition the results are also compared with EPOSv3 with UrQMD [25] and Statistical Hadronization Model (SHM), which describe a flat trend of  $\Xi(1530)^0/\Xi$  as a function of  $\langle dN_{ch}/d\eta_{lab} \rangle$  but overestimates the value of the ratio. Considering results from all collision systems, which cover the multiplicity range from 7.1 to 1448, the ratio is flat across system size. **The constant behavior of  $\Xi(1530)^0/\Xi$  indicates that neither regeneration nor re-scattering dominate, leading to little net change of the yield of resonances in the hadronic medium.**

Furthermore, the ratios of  $\Xi(1530)^0$  to  $\Xi$  in Pb–Pb collisions are studied as a function of  $p_T$  and the result is shown in Figure 4.3. The ratios in three different centrality intervals increase with  $p_T$  in measured  $p_T$  ranges. The ratio



from peripheral events is slightly larger than the ratio in semi-central and central events but within  $1\text{-}\sigma$  deviation.

The results of  $\Xi(1530)^0/\Xi$  can be compared to yield-ratio from the other resonances. Figure 4.4 shows ratio obtained from mesonic resonances,  $\rho/\pi$ , in pp and Pb–Pb collisions and the ratio is suppressed from small to large collision systems. Note that, the lifetime of  $\rho$  is about three times shorter than it of  $K(892)^*0$ . The measurement of  $\rho/\pi$  is compared with EPOSv3 with/without UrQMD. We have observed that the EPOSv3 prediction with UrQMD, which includes a modeling of re-scattering and regeneration in the hadronic phase, well describes the suppression trend from peripheral to central PbPb collisions, while the prediction without UrQMD does not reproduce the decreasing trend. This behavior is explained by the dominance of (pseudo-)elastic re-scattering of decay daughters over regeneration in the hadronic phase.

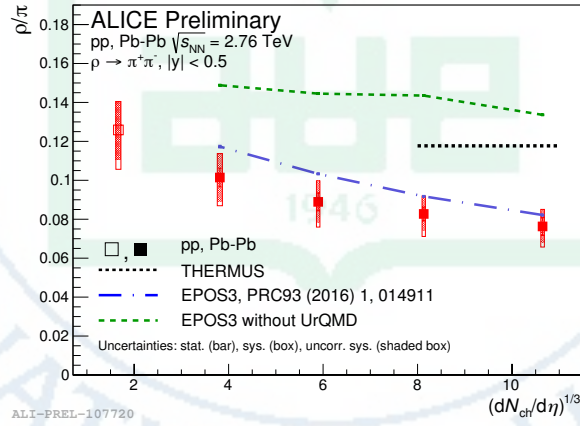


Figure 4.4: Ratio of  $\rho/\pi$  for different system sizes in pp and Pb–Pb collisions. Statistical uncertainties (bars) are shown as well as total systematic uncertainties (hollow boxes) and systematic uncertainties uncorrelated across multiplicity (shaded boxes).

The yield-ratios from baryonic resonances having different lifetimes are shown in Figure 4.5. The left panel on Figure 4.5 is ratio of  $\Sigma(1385)^\pm/\Lambda$  in pp and p–Pb collisions. The  $\Sigma(1385)^\pm/\Lambda$  ratios are consistent with the value predicted by

PYTHIA8 in pp, whereas the DPMJET prediction for p-Pb collisions underestimates the experimental data. In pp and p-Pb the ratios are higher than predicted by PYTHIA8 and DPMJET. The constant behavior of  $\Sigma(1385)^\pm$  in pp and p-Pb are comparable to the results obtained by the STAR collaboration at lower energies in pp and d-Au collisions. Because the lifetime of  $\Sigma(1385)^\pm$  ( $c\tau \sim 5.5$  fm) is comparable to the lifetime of  $K(892)^{*0}$ , one could expect that they show similar behavior. But, it is hard to conclude due to different cross section of decay particle of them. Thus, the results of  $\Sigma(1385)^\pm/\Lambda$  in Pb-Pb collisions is one of the key measurements to confirm that the particle having short lifetime can be affected by re-scattering effect rather than the regeneration.

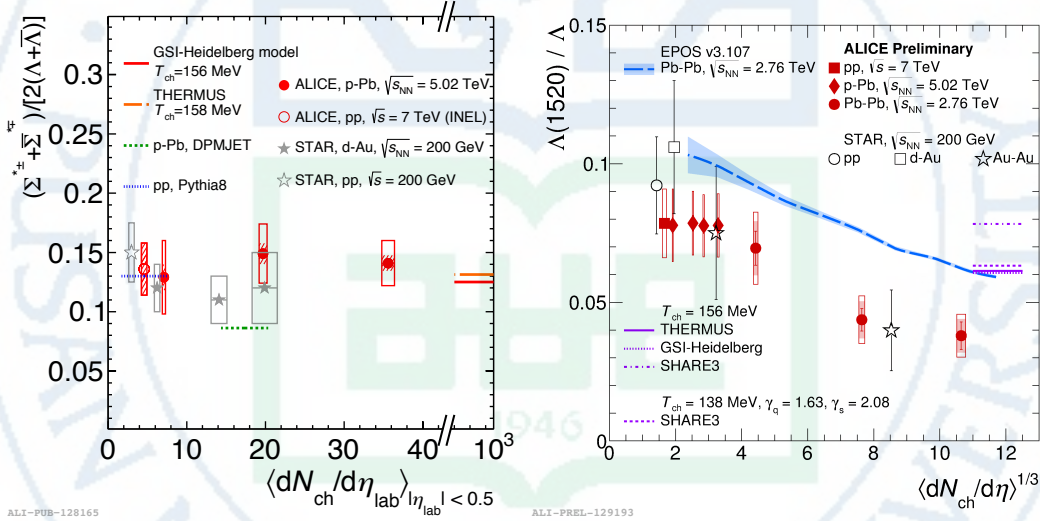


Figure 4.5: Ratio of  $\Sigma(1385)^\pm$  for different system sizes in pp and p-Pb collisions (left) and ratio of  $\Lambda(1520)/\Lambda$  in pp, p-Pb and Pb-Pb collisions (right). Statistical uncertainties (bars) are shown as well as total systematic uncertainties (hol-low boxes) and systematic uncertainties uncorrelated across multiplicity (shaded boxes).

The right panel of Figure 4.5 presents ratio of  $\Lambda(1520)/\Lambda$  in pp, p-Pb and Pb-Pb collisions. The  $\Lambda(1520)/\Lambda$  ratios in small system such as pp and p-Pb collisions show constant behavior which is similar trend with  $\Sigma(1385)^\pm/\Lambda$  in small system. Suppression of  $\Lambda(1520)/\Lambda$  is observed from pp, peripheral to central Pb-Pb collisions, which is similar to the behavior of  $\rho/\pi$  with system size. The suppression

of  $\Lambda(1520)$  ( $c\tau \sim 12.6$  fm) in central Pb–Pb collisions suggests the dominance of (pseudo)elastic re-scattering of decay daughter particles in the hadronic phase.

**These results support the existence of a hadronic phase lasting long enough to cause a significant reduction of the reconstructible yield of short-lived resonances.**

The integrated particle ratios to ground state particle in central Pb–Pb events with respect to peripheral events are measured as the double ratios. Figure 4.6 summarized the double ratio as a function of lifetime of each particle. As shown in the Figure 4.6, double ratio from resonances with lifetime shorter than  $\Xi(1530)^0$  is less than one. From the results, one might conclude that the lifetime of hadronic phase at LHC energies is less than the lifetime of  $\Xi(1530)^0$ .

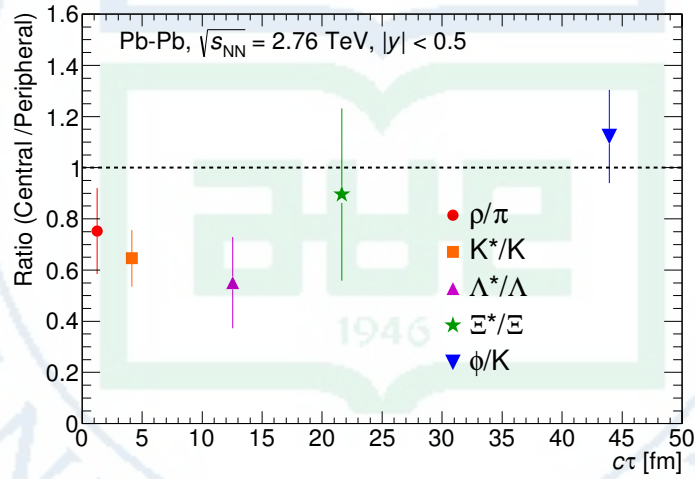


Figure 4.6: Double ratios of each resonances to ground-state hadrons obtained in central events divided by peripheral events in Pb–Pb collisions at  $\sqrt{s_{\text{NN}}} = 2.76$  TeV. Statistical uncertainties and systematic uncertainties are summed in quadrature.

### 4.2.2 Integrated particle ratio to $\pi$

In order to study evolution of relative strangeness production, the measured  $\Xi(1530)^0$  yields are compared with the yield of  $\pi$ . The integrated yield ratio of  $\Xi(1530)^0$  to  $\pi$  as a function of  $\langle dN_{\text{ch}}/d\eta_{\text{lab}} \rangle$  is shown in Figure 4.7. The ratio increase from pp to p-Pb collision systems as seen from multi-strange to pion ratio, see Figure 1.6. In Pb-Pb collisions, the ratio is constant and below the one extracted for the highest multiplicity class in p-Pb collisions.

The predictions from QCD-inspired models such as PYTHIA for pp [46] and DPMJET for p-Pb [36] clearly underestimate the observed yield ratios, whereas the statistical one seems to be comparable with results from high multiplicity in p-Pb. However the ratio in Pb-Pb is below the value of the thermal model. The SHM prediction with multiplicity shows an increasing trend from high multiplicity class in p-Pb collisions to the semi-central events in Pb-Pb collisions, then it decreases. The EPOS prediction is also shown as a function of  $\langle dN_{\text{ch}}/d\eta_{\text{lab}} \rangle$  [40, 41, 42, 43]. The prediction is flat with  $\langle dN_{\text{ch}}/d\eta_{\text{lab}} \rangle$  and matches the results in central p-Pb collisions, while it overestimates the results in Pb-Pb collisions. This discrepancy between model and experimental results is already seen in bottom panel in Figure 4.1. The EPOS overestimates the  $p_{\text{T}}$ -spectra, especially in the low  $p_{\text{T}}$  region where most of the particle yield are originated.

The results in small systems such as pp and p-Pb collisions are consistent with previous observation of ground-state particles to pion ratios. Figure 4.8 presents particle yield ratios to pions of strange and multi-strange hadrons normalized to the values measured in pp collisions. As shown in the Figure 4.8, the  $\Xi(1530)^0$  to pion ratios follow the trend of  $\Xi/\pi$  as function of  $\langle dN_{\text{ch}}/d\eta_{\text{lab}} \rangle$ . **These results indicate that the strangeness enhancement observed in p-Pb collisions depends predominantly on the strangeness content, rather than on the hadron mass.**

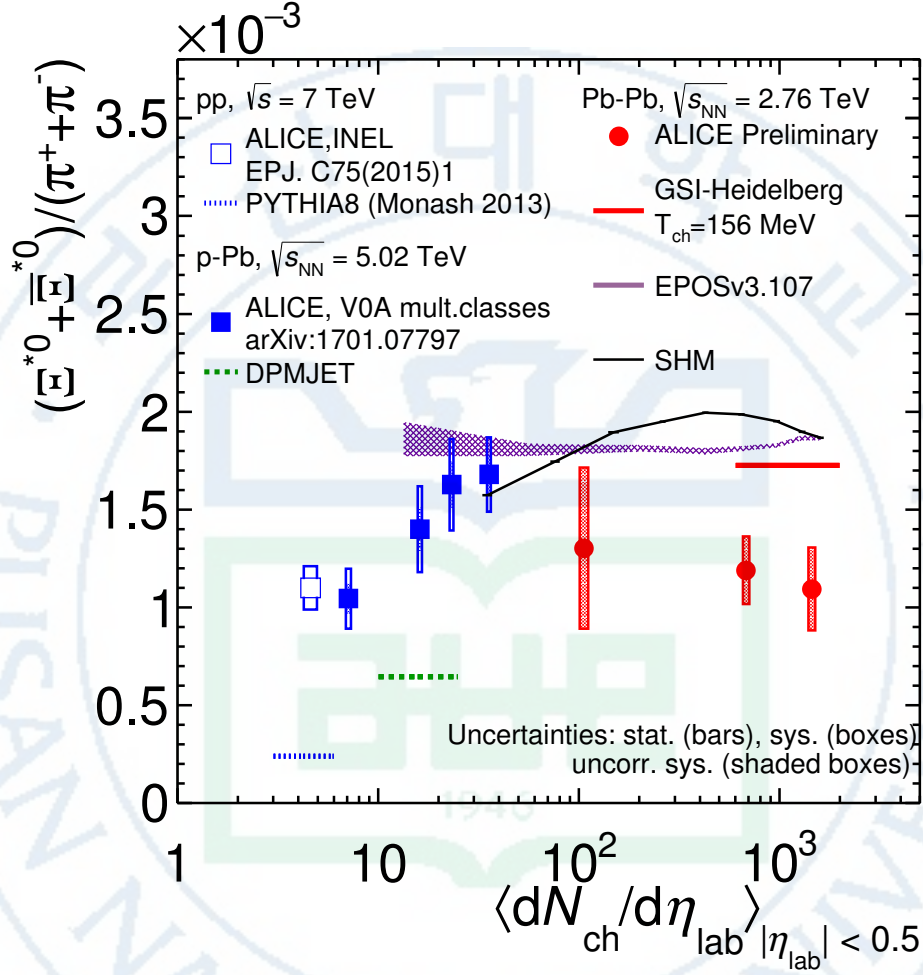


Figure 4.7: Ratio of  $\Xi(1530)^0$  to  $\pi^\pm$ , measured in pp [47] and p-Pb [45] collisions, as a function of the average charged particle density ( $\langle dN_{ch}/d\eta_{lab} \rangle$ ) measured at mid-rapidity. Statistical uncertainties (bars) are shown as well as total systematic uncertainties (hollow boxes) and systematic uncertainties uncorrelated across multiplicity (shaded boxes). A few model predictions are also shown as lines at their appropriate abscissa.



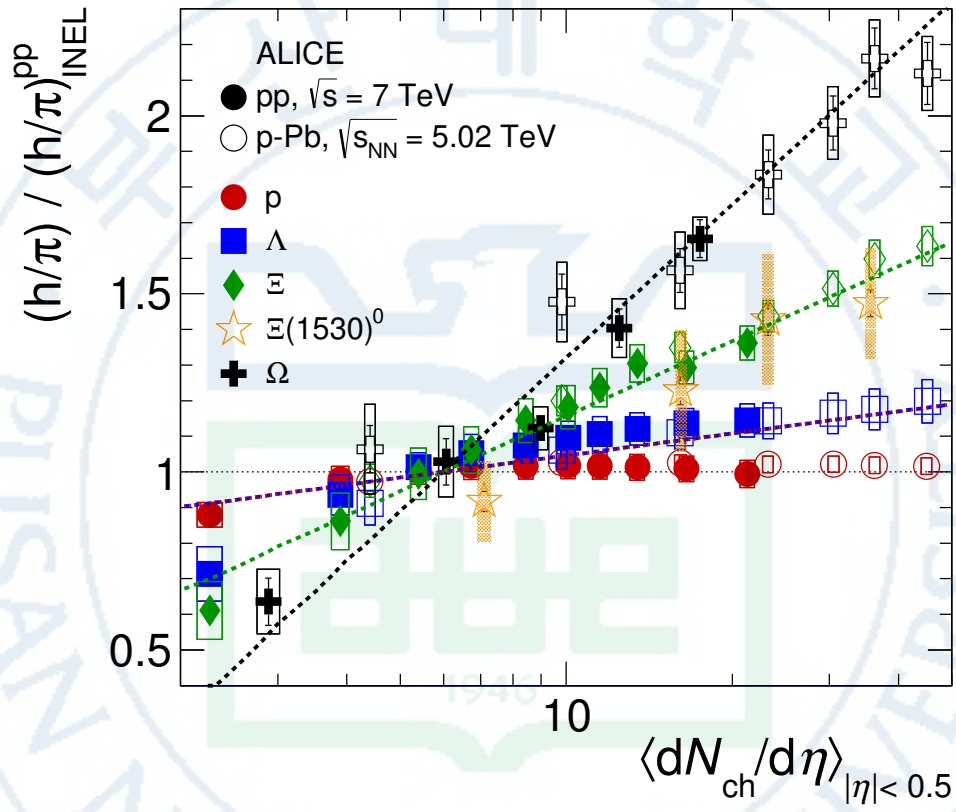


Figure 4.8: Particle yield ratios to pions of strange and multi-strange hadrons normalized to the values measured in pp collisions, both in pp and in p-Pb collisions. The common systematic uncertainties cancel in the double-ratio. The empty boxes represent the remaining uncorrelated uncertainties.

### 4.3 Multiplicity and mass dependence of $\langle p_T \rangle$

Figure 4.9 shows the mean transverse momentum,  $\langle p_T \rangle$ , as a function of mean charged-particle multiplicity density,  $\langle dN_{\text{ch}}/d\eta_{\text{lab}} \rangle$ , at midrapidity. The results of  $\Xi(1530)^0$  are compared with those for other hyperons observed in p-Pb collisions at  $\sqrt{s_{\text{NN}}} = 5.02$  TeV [11, 19].

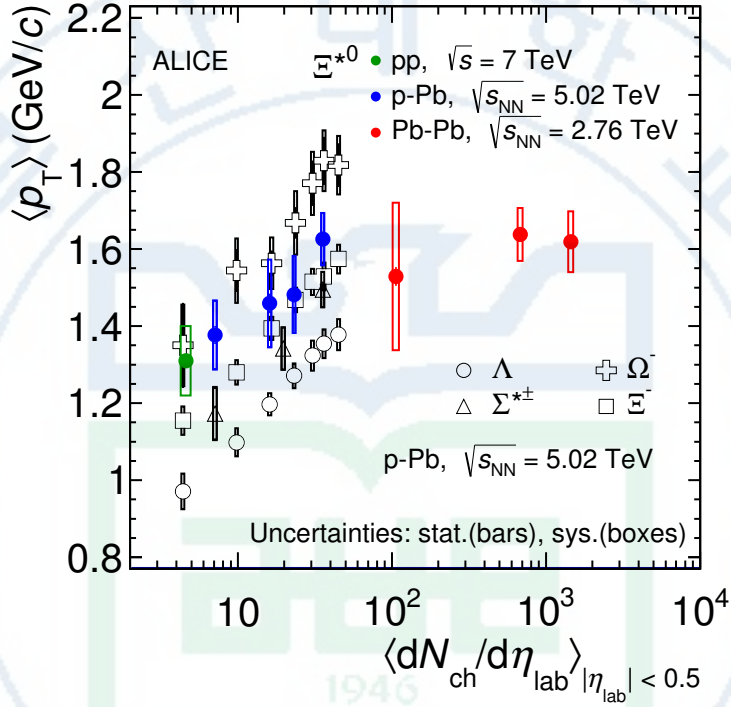


Figure 4.9: Mean transverse momenta  $\langle p_T \rangle$  of  $\Lambda$ ,  $\Xi^-$ ,  $\Sigma^{*\pm}$ ,  $\Xi^{*0}$  and  $\Omega^-$  in p-Pb collisions at  $\sqrt{s_{\text{NN}}} = 5.02$  TeV as a function of mean charged-particle multiplicity density  $\langle dN_{\text{ch}}/d\eta_{\text{lab}} \rangle$ , measured in the pseudorapidity range  $|\eta_{\text{lab}}| < 0.5$ . The results for  $\Lambda$ ,  $\Xi^-$  and  $\Omega^-$  are taken from [11, 19, 23]. Results for  $\Xi(1530)^0$ , the  $\langle p_T \rangle$  obtained in pp collisions at  $\sqrt{s} = 7$  TeV and Pb-Pb collisions at  $\sqrt{s_{\text{NN}}} = 2.76$  TeV are also presented. Statistical and systematic uncertainties are represented as bars and boxes, respectively.

Increasing trends of the  $\langle p_T \rangle$  from low to high multiplicities are observed for all hyperons in p-Pb collisions while the  $\langle p_T \rangle$  of  $\Xi(1530)^0$  is saturated in Pb-Pb collisions. The  $\langle p_T \rangle$  of  $\Xi(1530)^0$  is observed to have a 20% higher value at  $\langle dN_{\text{ch}}/d\eta_{\text{lab}} \rangle = 35.6$  than the results at  $\langle dN_{\text{ch}}/d\eta_{\text{lab}} \rangle = 7.1$ . Note that the value 35.6 corresponds with multiplicity for the 0-20% centrality classes

in p-Pb collisions and the value of 7.1 is the mean charged particle multiplicity density for minimum-bias events in pp collisions. This result is similar to the one obtained for the other hyperons.

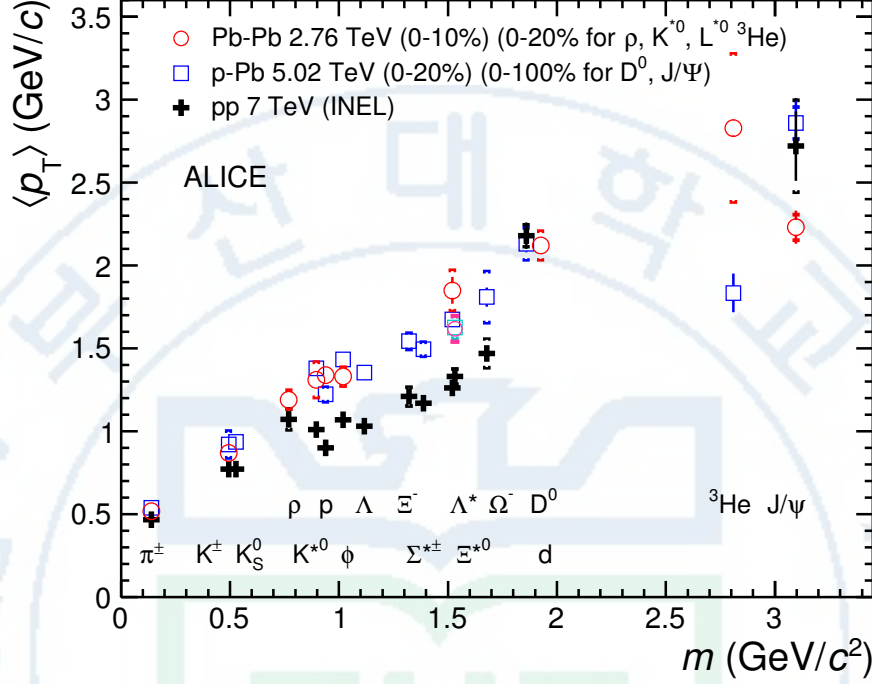


Figure 4.10: Mass dependence of the mean transverse momenta of identified particles for the 0-20% V0A multiplicity class and with  $-0.5 < y_{\text{CMS}} < 0$  in p-Pb collisions at  $\sqrt{s_{\text{NN}}} = 5.02$  TeV [11, 19], and in minimum-bias pp collisions at  $\sqrt{s} = 7$  TeV [45] with  $|y_{\text{CMS}}| < 0.5$ . Additionally,  $D^0$  and  $J/\psi$  results are plotted. The  $D^0$  and  $J/\psi$  were measured in different rapidity ranges:  $|y_{\text{CMS}}| < 0.5$  [48] ( $|y_{\text{CMS}}| < 0.9$  [49]) for  $D^0$  ( $J/\psi$ ) in pp and  $-0.96 < y_{\text{CMS}} < 0.04$  [48] ( $-1.37 < y_{\text{CMS}} < 0.43$  [50]) for  $D^0$  ( $J/\psi$ ) in p-Pb. Note also that the results for  $D^0$  and  $J/\psi$  in p-Pb collisions are for the 0-100% multiplicity class.

In small systems, **the  $\langle p_T \rangle$  follows an approximate mass ordering:**

- $\langle p_T \rangle_\Lambda < \langle p_T \rangle_{\Xi^-} \simeq \langle p_T \rangle_{\Sigma^{*\pm}} < \langle p_T \rangle_{\Xi^{*0}} < \langle p_T \rangle_{\Omega^-}$

Figure 4.10 shows a summary of the mass dependence of the  $\langle p_T \rangle$  of identified particles including not only light-flavor hadrons but also heavy-flavor hadrons. For the light-flavor hadrons, the mean transverse momenta in p-Pb collisions at  $\sqrt{s_{\text{NN}}} = 5.02$  TeV are observed to be consistently higher than those in minimum-bias events in pp collisions at  $\sqrt{s} = 7$  TeV. This difference could come from the

different selection of centrality classes. If we compare results from minimum-bias events in pp and p-Pb collisions, e.g.,  $D^0$  or  $J/\Psi$ , the results are then compatible. Similarly, the results from central p-Pb collisions and central Pb-Pb collisions look comparable, except for  $J/\Psi$ . The reason why the  $J/\Psi$  behaves differently could be due to different production mechanisms between heavy and light flavors. However, it is hard to conclude because of lack of results for charmed hadrons.

In order to have a better understanding on  $\langle p_T \rangle$  in different collision systems, comparison of the results from the same multiplicity could be helpful, since it can provides information from similar system size so that the difference is only from collision systems.

Because of small decrease of the  $\langle p_T \rangle$  for proton and  $\Lambda$  relative to those for  $K^{*0}$  and  $\phi$ , two different trends for mesons and baryons have been suggested [51]. However a different trend for mesons and baryons cannot be convincingly established. The more measurement of hadrons with different mass will help to investigate these aspects.

## 4.4 Conclusions and outlook

In this work, the  $\Xi(1530)^0$  have been measured from p-Pb and Pb-Pb collisions at mid-rapidity in ALICE at the center-of-mass energy  $\sqrt{s_{NN}} = 5.02$  TeV and  $\sqrt{s_{NN}} = 2.76$  TeV, respectively. The study of strange-resonance at mid-rapidity in heavy ion collisions is expected to carry the information on the QGP evolution. From the measurement of  $p_T$ -spectra of  $\Xi(1530)^0$ , the integrated yield and  $\langle p_T \rangle$  were obtained.

In order to study properties of hadronic phase, the yield ratio of  $\Xi(1530)^0$  to its ground state particle is extracted and compared to the yield ratios of other resonances with different lifetimes, such as  $\rho$ ,  $K^*(892)^0$ ,  $\Sigma(1385)^\pm$ ,  $\Lambda(1520)$  and  $\phi$ .

As a result, yield ratios extracted from short-lived resonances which have a lifetime shorter than the  $\Xi(1530)^0$  one, is suppressed from small to large collision

systems, whereas the yield ratios of the longer-lived particle,  $\Xi(1530)^0$  and  $\phi$ , to its ground state particle are constant across the system size. This behavior could be explained by the dominance of (pseudo-)elastic re-scattering of decay daughters of short-lived particles over regeneration in the hadronic phase.

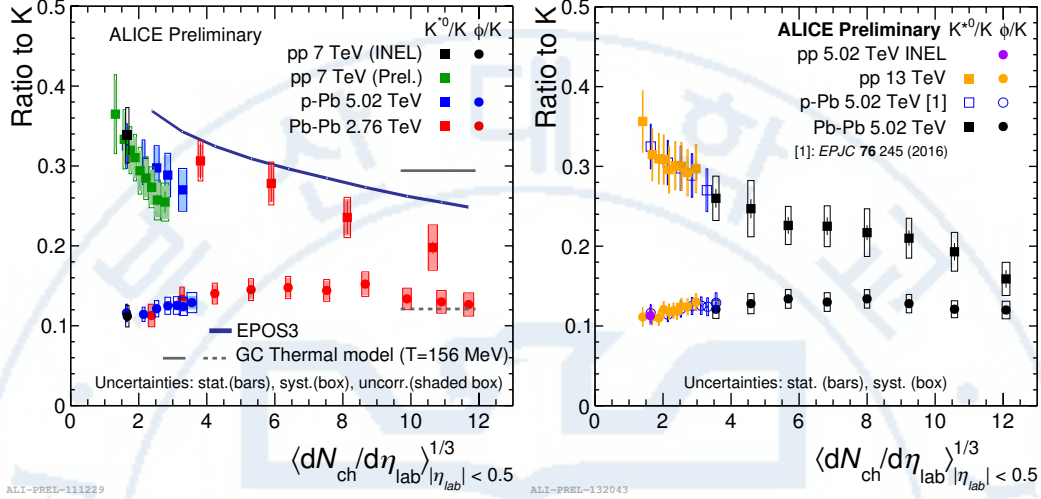


Figure 4.11:  $p_T$ -integrated  $K^*(892)^0/K$  and  $\phi/K$  ratios in different collision systems. The yield ratios obtained different multiplicity event in pp collisions at  $\sqrt{s}=7$  TeV, in p-Pb collisions at  $\sqrt{s_{NN}}=5.02$  TeV and in Pb-Pb collisions at  $\sqrt{s_{NN}}=2.76$  TeV are shown in left figure with the results obtained from inelastic event in pp collisions. The same yield ratios but with different energies (pp at  $\sqrt{s}=13$  TeV, Pb-Pb at  $\sqrt{s_{NN}}=5.02$  TeV) are shown on right figure.

Recently, multiplicity-dependent analysis has been performed, even, in pp collisions and it can help to understand the small system by comparing the results obtained from p-Pb collisions. Figure 4.11 shows yield ratios not only from different collision systems but also from multiplicity-dependent analysis with pp data sample. The left panel on Figure 4.11 presents the  $K^*(892)^0/K$  and  $\Phi/K$  ratio in pp at  $\sqrt{s}=7$  TeV, p-Pb at  $\sqrt{s_{NN}}=5.02$  TeV and Pb-Pb at  $\sqrt{s_{NN}}=2.76$  TeV. The right panel shows same particle ratios but with different energies from Run2 data samples. e.g., pp at  $\sqrt{s}=13$  TeV, Pb-Pb  $\sqrt{s_{NN}}=5.02$ .

Measurement of  $\Xi(1530)^0$  with multiplicity-dependent analysis with pp data sample also can be helpful to understand the re-scattering or regeneration effects



in the small system by comparing the previous results obtained in pp and p-Pb collisions. Therefore, it would be valuable to analyze  $\Xi(1530)^0$  in pp collisions as a next study.

In addition, the multiplicity-dependent analysis in pp collisions supports to the study of strangeness enhancement in the small system as shown in Figure 4.8. From the  $\Xi(1530)^0$  measurement described in this thesis, we have observed that the enhancement of strangeness in the small system depends on strangeness contents instead of the mass of hadrons. Study of  $\Xi(1530)^0$  in different multiplicity classes in pp collisions allows one to extend the results covering not only multiplicity ranges for p-Pb collisions but also more small system which is hard to be measured in p-Pb collisions.

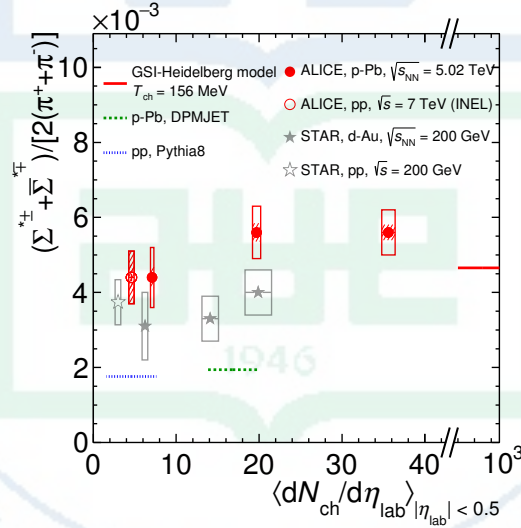


Figure 4.12: Ratio of  $\Sigma(1385)^\pm$  to  $\pi$  measured in pp [45, 47, 52, 53], dAu [52, 54] and pPb [11] collisions, as a function of the average charged particle density ( $\langle dN_{\text{ch}}/d\eta_{\text{lab}} \rangle$ ) measured at mid-rapidity. Statistical uncertainties (bars) are shown as well as total systematic uncertainties (hollow boxes) and systematic uncertainties uncorrelated across multiplicity (shaded boxes). A few model predictions are also shown as lines at their appropriate abscissa.

The comparison of not only doubled-strangeness particles,  $\Xi(1530)^0$  and  $\Xi$ , but also strangeness particles  $\Sigma(1385)^\pm$  and  $\Lambda$  are also very interesting in the context of small systems. Figure 4.12 shows the ratio of  $\Sigma(1385)^\pm$  to  $\pi$  as a function

of multiplicity. If the enhancement is related to the number of strangeness content, the ratio of  $\Sigma(1385)^\pm/\pi$  has a similar slope with  $\Lambda/\pi$ , since they have only one strange quark. We have observed that enhancement of  $\Sigma(1385)^\pm/\pi$  follows the one of  $\Lambda/\pi$  and such a result is consistent with the ones obtained for  $\Xi(1530)^0$ .

The comparison of  $\langle p_T \rangle$  of  $\Xi(1530)^0$  and other hyperons indicates that the  $\langle p_T \rangle$  of all hyperons including resonances increases with mean charged-particle multiplicity density in p-Pb collisions. The mass ordering of  $\langle p_T \rangle$  has been observed from identified particles including not only resonances but also ground state particles. As discussed in Section 4.3, comparison of  $\langle p_T \rangle$  from the same multiplicity could help to understand its evolution for different collision systems. Figure 4.13 presents system size dependence of the  $\langle p_T \rangle$  of  $K^*(892)^0$  and  $\Phi$  compared to that of the proton.

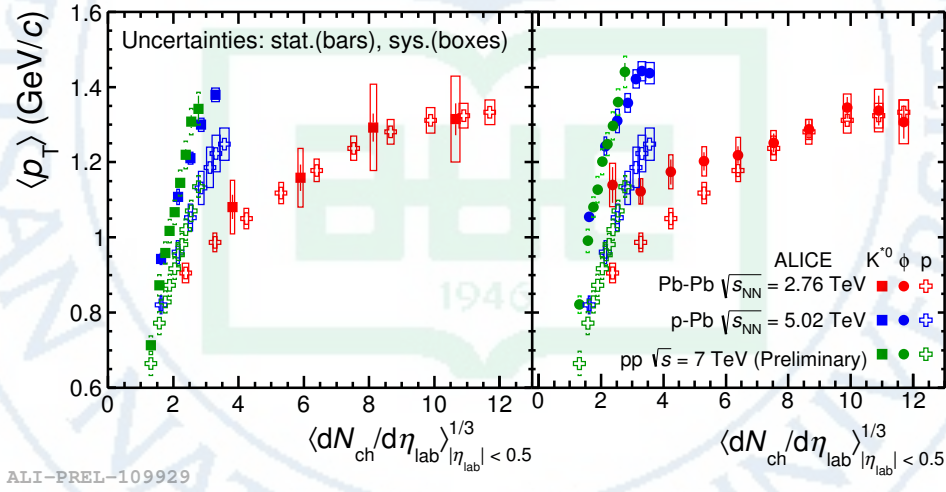


Figure 4.13: System size dependence of the mean transverse momentum of  $K^*(892)^0$  compared to that of the proton (left panel) and  $\langle p_T \rangle$  of  $\phi$  compared to that of the proton (right panel). The system size is defined as the cubic root of the average charged particle multiplicity density measured in the ALICE central barrel ( $|\eta| < 0.5$ ) in pp at  $\sqrt{s} = 7$  TeV (green), p-Pb at  $\sqrt{s_{NN}} = 5.02$  TeV (blue) and Pb-Pb at  $\sqrt{s_{NN}} = 2.76$  TeV (red). Statistical uncertainties are represented as bars, boxes indicate total systematic uncertainties.

As shown in Figure 4.13, at similar multiplicity, the  $\langle p_T \rangle$  is larger in pp and p-Pb than in Pb-Pb and the increase with multiplicity is steeper in small

systems. In order to have a better understanding on  $\langle p_T \rangle$  in different collision systems, comparison of the results which was shown in Figure 4.10 from the same multiplicity could be helpful, since it can provide information from similar system size so that the difference is only from different collision systems.

The  $\langle p_T \rangle$  also can be used for the study of hadronic phase because, if re-scattering or regeneration effect occurs, the shape of spectra could change. Consequently, the  $\langle p_T \rangle$  can change. Figure 4.14 shows the mass dependence of  $\langle p_T \rangle$  of resonances with EPOSv3 predictions of  $\langle p_T \rangle$ . The UrQMD takes account of re-scattering and regeneration effect in hadronic phase. The open diamond is the prediction of EPOSv3 with UrQMD OFF, and full diamond is prediction with UrQMD ON. As shown in Figure 4.14, the prediction of  $\langle p_T \rangle$  is larger when UrQMD ON for all particles. The deviation of  $\langle p_T \rangle$  from UrQMD ON and OFF is larger for short-lived resonance particles,  $\rho$ ,  $K^*(892)^0$ ,  $\Sigma(1385)^\pm$  and  $\Lambda(1520)$ . For the longer-lived resonances,  $\Xi(1530)^0$  and  $\Phi$ , the difference between UrQMD ON and OFF is small. From this comparison, one may conclude that the resonances with short lifetime could be affected re-scattering and regeneration effect in the hadronic phase.

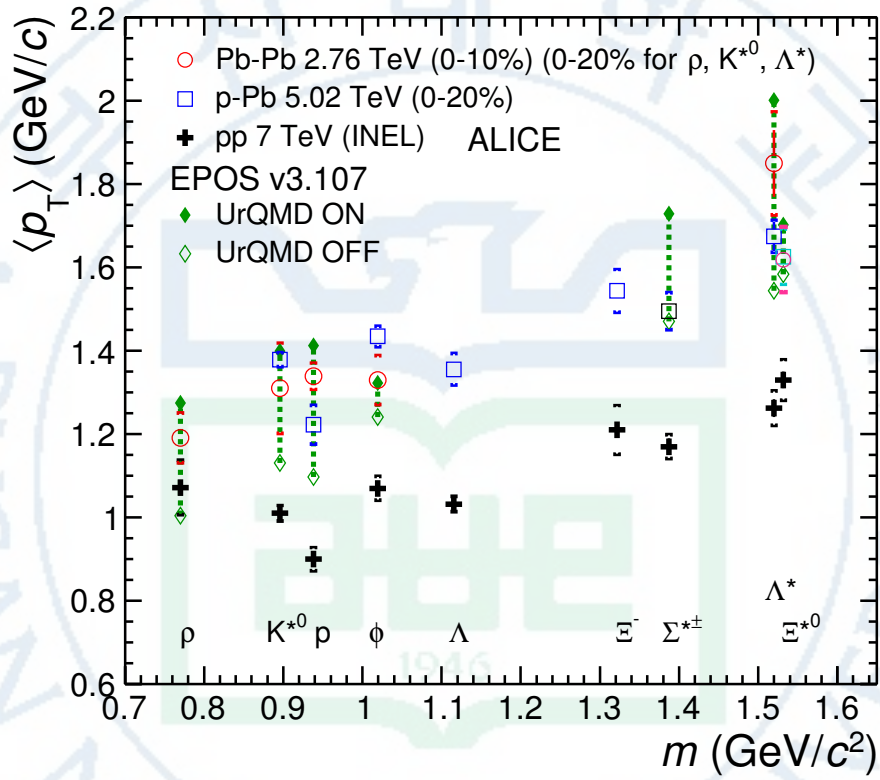


Figure 4.14: Mass dependence of the mean transverse momenta of identified particles and predictions from EPOS v3 with UrQMD OFF and ON for central (0-10%) Pb-Pb collisions at  $\sqrt{s_{NN}} = 2.76$  TeV.

- [1] C. B. L. Christof Gatttringer, “Quantum Chromodynamics on the Lattice: An Introductory Presentation,” *Lecture Note in Physics* **788**.
- [2] T. Bhattacharya, C. DeTar, H. T. Ding, S. Gottlieb, *et al.*, “The equation of state in (2+1)-flavor QCD,” *Phys. Rev.* **D90** (2014), [arXiv:1407.6387](#).
- [3] C. Alcock, “The Astrophysics and Cosmology of QuarkGluon Plasma,”.
- [4] F. Bellini, “Measurement of  $K(892)^0$  resonance production in Pb–Pb collisions with the ALICE experiment at the LHC,” *CERN-THESIS-2013-393* **D90** (2013) 145.
- [5] L. Evans and P. Bryant, “LHC Machine,” *JINST* **3** (2008) S08001.
- [6] J. D. Bjorken, “Highly relativistic nucleus-nucleus collisions: The central rapidity region,” *Phys. Review* **D27** (1983) 140–151.
- [7] F. Karsch, “Lattice QCD at high temperature and density,” *Lect. Notes Phys.* **583** (2002) 209–249, [arXiv:hep-lat/0106019](#).
- [8] Y. Aoki, G. Endrodi, Z. Fodor, S. Katz, and K. Szabo, “The order of the quantum chromodynamics transition predicted by the standard model of particle physics,” *Nature* **443** (2006) 675–678, [arXiv:hep-lat/0611014](#).
- [9] A. Andronic, P. Braun-Munzinger, K. Redlich, and J. Stachel, “Decoding the phase structure of QCD via particle production at high energy,” [arXiv:1710.09425](#).
- [10] U. W. Heinz, “Concepts of Heavy-Ion Physics,” [arXiv:hep-ph/0407360](#).
- [11] **ALICE** Collaboration, J. Adam *et al.*, “Multiplicity dependence of pion, kaon, proton and lambda production in p–Pb collisions at  $\sqrt{s_{NN}} = 5.02$  TeV,” *Phys. Lett.* **B728** (2014) 25–38, [arXiv:1307.6796 \[nucl-ex\]](#).
- [12] **ALICE** Collaboration, J. Adam *et al.*, “Centrality Dependence of the Charged-Particle Multiplicity Density at Midrapidity in Pb-Pb Collisions at  $\sqrt{s_{NN}} = 5.02$  TeV,” *Phys. Rev. Lett.* **116** (2016), [arXiv:1512.06104 \[nucl-ex\]](#).
- [13] C. Markert, “What do we learn from Resonance Production in Heavy Ion Collisions?,” *J. Phys. Nucl. Part. Physics* **31** (2005) S169–178.
- [14] G. Torrieri and J. Rafelski, “Strange hadron resonances as a signature of freeze-out dynamics,” *Phys. Lett* **B509** (2001) 239–245.
- [15] **ALICE** Collaboration, J. Adam *et al.*, “ $K^*(892)^0$  and  $\phi(1020)$  meson production at high transverse momentum in pp and Pb–Pb collisions at 2.76 TeV,” [arXiv:1702.00555](#).
- [16] **Particle Data Group** Collaboration, K. Olive *et al.*, “Review of Particle Physics,” *Chin. Phys.* **C38** (2014) 090001.



- [17] J. Rafelski and B. Muller, “Strangeness Production in the Quark-Gluon Plasma,” *Phys. Rev. Lett* **48** (1982) 1066–1069.
- [18] **ALICE** Collaboration, B. Abelev *et al.*, “Multi-strange baryon production at mid-rapidity in Pb–Pb collisions at  $\sqrt{s_{\text{NN}}}=2.76$  TeV,” *Phys. Lett.* **B728** (2014) 216–227, [arXiv:1307.5543 \[nucl-ex\]](#).
- [19] **ALICE** Collaboration, J. Adam *et al.*, “Multi-strange baryon production in p–Pb collisions at  $\sqrt{s_{\text{NN}}}=5.02$  TeV,” *Phys. Lett.* **B758** (2016) 389–401, [arXiv:1512.07227 \[nucl-ex\]](#).
- [20] C. Blume and C. Markert, “Strange hadron production in heavy ion collisions from SPS to RHIC,” *Progress in Particle and Nuclear Physics* **66** (2011) 834–879.
- [21] T. K. Nayak, “Heavy Ions: Results from the Large Hadron Collider,” *Pramana* **79** (2012) 719–735.
- [22] A. Collaboration, “Strangeness Enhancement and Canonical Suppression,” *Nature Physics* (2017) .
- [23] **ALICE** Collaboration, J. Adam *et al.*, “Production of  $K^*(892)^0$  and  $\phi(1020)$  in p–Pb collisions at  $\sqrt{s_{\text{NN}}}=5.02$  TeV,” *Eur. Phys. J.* **C76** (2016) 245, [arXiv:1601.7868 \[nucl-ex\]](#).
- [24] **ALICE** Collaboration, J. Adam *et al.*, “ $K^*(892)^0$  and  $\phi(1020)$  production in Pb–Pb collisions at  $\sqrt{s_{\text{NN}}}=2.76$  TeV,” *Phys. Rev.* **C91** (2015) 024609.
- [25] A. G. Knospe, C. Markert, K. Werner, J. Steinheimer, and M. Bleicher, “Hadronic resonance production and interaction in partonic and hadronic matter in EPOS3 with and without the hadronic afterburner UrQMD,” *Phys. Rev.* **C93** (2016) 014911.
- [26] **ALICE** Collaboration, B. Abelev *et al.*, “Performance of the ALICE Experiment at the CERN LHC,” *Int. J. Mod. Phys.* **A29** (2014) 1430044, [arXiv:1402.4476 \[nucl-ex\]](#).
- [27] “ALICE Technical Proposal,” *In CERN-LHCC-95-71* (1995) .
- [28] **ALICE** Collaboration, K. Aamodt *et al.*, “The ALICE experiment at the CERN LHC,” *JINST* **3** (2008) S08002.
- [29] C. Lippmann, “Performance of the ALICE Time Projection Chamber,” *Physics Procedia*. **37** (2012) 434–441.
- [30] **ALICE** Collaboration, B. A. et al., “ $K_s^0$  and  $\Lambda$  Production in Pb–Pb Collisions at  $\sqrt{s_{\text{NN}}}=2.76$  TeV,” *Phys. Rev. Lett.* **111** (2013) 222301, [arXiv:1307.5530 \[nucl-ex\]](#).
- [31] **ALICE** Collaboration, L. B. et al, “Definition of the ALICE coordinate system and basic rules for sub-detector components numbering,” *In Internal Note ALICE-INT-2003-038* (2003) .

- [32] A. Toia, “Participants and spectators at the heavy-ion fireball,” *CERN COIRIER* **April** (2013) .
- [33] **ALICE** Collaboration, J. Adam *et al.*, “Centrality dependence of particle production in p–Pb collisions at  $\sqrt{s_{\text{NN}}}= 5.02$  TeV,” *Phys. Rev.* **C91** (2015) 064905, [arXiv:1412.6828 \[nucl-ex\]](#).
- [34] **ALICE** Collaboration, B. Abelev *et al.*, “Centrality determination of Pb–Pb collisions at  $\sqrt{s_{\text{NN}}}= 2.76$  TeV with ALICE,” *Phys. Rev.* **C88** (2013) , [arXiv:1303.0737 \[nucl-ex\]](#).
- [35] **ALICE** Collaboration, B. Abelev *et al.*, “Pseudorapidity Density of Charged Particles in p–Pb Collisions at  $\sqrt{s_{\text{NN}}}= 5.02$  TeV,” *Phys. Rev. Lett.* **110** (2013) 032301, [arXiv:1210.3615 \[nucl-ex\]](#).
- [36] S. Roesler, R. Engel, , and J. Ranft, “The Monte Carlo Event Generator DPMJET-III, Advanced Monte Carlo for Radiation Physics, Particle Transport Simulation and Applications,” *Conference Proceedings, MC2000, Lisbon, Portugal, October 23-26* (2000) 1033–1038, [hep-ph/0012252](#).
- [37] R. Brun, F. Carminati, and S. Giani, “GEANT detector description and simulation tool,” *CERN-W5013* (1994) .
- [38] R. Barlow, “Systematic Errors: Facts and Fictions,” *Presented at Advanced Statistical Techniques in HEP, Durham, March 2002* (2002) 333p, [hep-ex/0207026v1](#).
- [39] **ALICE** Collaboration, B. Abelev *et al.*, “Centrality dependence of  $\pi$ ,  $K$  and  $p$  production in Pb–Pb collisions at  $\sqrt{s_{\text{NN}}}= 2.76$  TeV,” *Phys. Rev.* **C88** (2013) , [arXiv:1301.4361 \[nucl-ex\]](#).
- [40] H. Drescher, M. Hladik, S. Ostapchenko, T. Pierog, and K. Wener, “Parton-Based Gribov-Regge Theory,” *Phys. Rept.* **350** (2001) 93–289, [hep-ph/0007198](#).
- [41] K. Werner, I. Karpenko, T. Pierog, M. Bleicher, and K. Mikhailov., “Event-by-event simulation of the three-dimensional hydrodynamic evolution from flux tube initial conditions in ultrarelativistic heavy ion collisions,” *Phys. Rev.* **C82** (2010) 044904.
- [42] K. Werner, B. Guiot, I. Karpenko, and T. Pierog., “Analyzing radial flow features in p-Pb and p-p collisions at several TeV by studying identified-particle production with the event generator EPOS3,” *Phys. Rev.* **C89** (2014) 064903.
- [43] K. Werner., “Core-Corona Separation in Ultra-Relativistic Heavy Ion Collision,” *Phys. Rev. Lett.* **98** (2007) 152301.
- [44] A. Andronic, P. Braun-Munzinger, and J. Stachel, “Thermal hadron production in relativistic nuclear collisions: the hadron mass spectrum, the horn, and the QCD phase transition,” *Phys. Lett.* **B673** (2009) 142–145, [arXiv:0812.1186](#).

- [45] **ALICE** Collaboration, B. Abelev *et al.*, “Production of  $\Sigma(1385)^\pm$  and  $\Xi(1530)^0$  in proton-proton collisions at  $\sqrt{s}=7$  TeV,” *Eur. Phys. J. C* **75** (2015) 1, [arXiv:1406.3206 \[nucl-ex\]](#).
- [46] T. Sjöstrand, S. Mrenna, and P. Skands, “A brief introduction to PYTHIA 8.1,” *Comput. Phys. Comm.* **178** (2008) 852–867, [arXiv:0710.3820 \[hep-ph\]](#).
- [47] **ALICE** Collaboration, J. Adam *et al.*, “Measurement of pion, kaon and proton production in proton-proton collisions at  $\sqrt{s}=7$  TeV,” *Eur. Phys. J. C* **75** (2015) 226, [arXiv:1504.00024 \[nucl-ex\]](#).
- [48] **ALICE** Collaboration, J. Adam *et al.*, “ $D$ -meson production in p–Pb collisions at  $\sqrt{s_{NN}}=5.02$  TeV and in pp collisions at  $\sqrt{s}=7$  TeV,” *Phys. Rev. C* **94** (2016) 054908, [arXiv:1605.07569 \[nucl-ex\]](#).
- [49] **ALICE** Collaboration, B. Abelev *et al.*, “Inclusive  $J/\psi$  production in pp collisions at  $\sqrt{s}=2.76$  TeV,” *Phys. Lett. B* **718** (2012) 295–306, [arXiv:1203.3641 \[hep-ex\]](#).
- [50] **ALICE** Collaboration, J. Adam *et al.*, “Rapidity and transverse-momentum dependence of the inclusive  $J/\psi$  nuclear modification factor in p–Pb collisions at  $\sqrt{s_{NN}}=5.02$  TeV,” *JHEP* **06** (2015) 55, [arXiv:1503.07179 \[nucl-ex\]](#).
- [51] A. Velásquez, “Mean  $p_T$  scaling with  $m/n_q$  at the LHC: Absence of (hydro) flow in small systems?,” *Nucl. Phys. A* **943** (2015) 9–17, [arXiv:1506.00584 \[hep-ph\]](#).
- [52] **STAR** Collaboration, B. I. Abelev *et al.*, “Systematic measurements of identified particle spectra in pp, d–Au, and Au–Au collisions at the STAR detector,” *Phys. Rev. C* **79** (2009) 034909.
- [53] **STAR** Collaboration, B. I. Abelev *et al.*, “Strange Baryon Resonance Production in  $\sqrt{s_{NN}}=200$  GeV p+p and Au+Au Collisions,” *Phys. Rev. Lett.* **97** (2006) 132301, [nucl-ex/0604019v2](#).
- [54] **STAR** Collaboration, B. I. Abelev *et al.*, “Hadronic resonance production in d–Au collisions at  $\sqrt{s_{NN}}=200$  GeV measured at the BNL Relativistic Heavy-Ion Collider,” *Phys. Rev. C* **78** (2008) 044906, [arXiv:0801.0450 \[nucl-ex\]](#).

# 대형강입자충돌기 (LHC)의 대형이온충돌기 실험 (ALICE)에서 측정된 크시( $\Xi(1530)^0$ ) 공명입자 생성 연구

송 지 혜

부산대학교 대학원 물리학과

## 요약

대형강입자충돌기 (Large Hadron Collider: LHC)에서 진행되는 초상대론적 중이온충돌을 통해 초 고온, 고압 상태의 물질을 생성할 수 있다. 극한상태 물질의 특성을 연구하기 위해 다양한 수명을 갖는 강입자들을 재구성 한다. 이를 통해서 쿼크물질과 강입자들의 상호작용 – 재산란 및 재생성 – 을 유추해볼 수 있다.

본 논문에서는 강입자 분석에 사용된 대형이온충돌기 실험 (A Large Ion Collider Experiment: ALICE)에 대해 설명하고, ALICE를 통한 입자 확인 방법에 대해서 논의한다.

다양한 수명을 갖는 강입자 중 본 논문에서는 크시 입자를 분석 하였다. 크시입자의 가로운동량 분포를 측정하였고, 그 분포를 통해 크시입자의 생성량과 평균가로운동량을 충돌 시스템에 대해 분석하였다.

본 논문에서는 여러 충돌 시스템으로부터 생성된 크시 입자와 긴수명을 갖는 입자들의 상대적인 생성량 및 평균가로운동량에 대해 논의 할 것이다.